Multi-Scale Modeling of Heat Transfers in Liquid-Film Flows for Electric Motors Cooling

van Quan Hoang

THÈSE

Pour l'obtention du grade de

DOCTEUR DE L'ÉCOLE NATIONALE SUPÉRIEURE DE MÉCANIQUE ET D'AÉROTECHNIQUE

(Diplôme National – Arrêté du 25 mai 2016 modifié par l'arrêté du 26 Août 2022)

Ecole Doctorale :
MIMME Mathématiques, Informatique, Matériaux, Mécanique, Energétique
Secteur de Recherche : Énergétique, thermique et combustion

Présentée par :

HOANG Van Quan

****

Modélisation multi-échelle du refroidissement par film liquide dans les machines électriques

****

Directeur(s)de thèse : **Frédéric PLOURDE, Matthieu FÉNOT**
Co-encadrant : **Guillaume VINAY**

****

Soutenue le 6 mai 2024

devant la Commission d'Examen

****

JURY

Président :
***Dominique LEGENDRE**, professeur, IMFT*
Rapporteurs :
Sivaramakrishnan "Bala" BALACHANDAR, professeur, Université de Floride
Christian RUYER-QUIL, professeur, Université Savoie Mont-Blanc
Membres du jury :
Nadia CANET, directrice de recherche, CEA
Frédéric PLOURDE, directeur de recherche, ENSMA
Matthieu FENOT, professeur, ENSMA
Guillaume VINAY, ingénieur de recherche, IFPEN (R116)

Modélisation multi-échelle du refroidissement par film liquide dans les machines électriques

Résumé: Le défi de construire un solveur pour la simulation du refroidissement à l'huile dans les extrémités des bobinages des moteurs électriques est l'objet de cette étude. Le premier segment se concentre sur les phénomènes de transfert thermique du flux de film liquide sur une surface complexe pré-mouillée. L'objectif est de comprendre les mécanismes d'interaction entre le liquide et la surface complexe. Une analyse détaillée des résultats de la simulation est réalisée, en tenant compte des effets de paramètres variables tels que le nombre de Reynolds et le nombre de Prandtl.
Suite à cela, un solveur précis VOF à deux phases couplé avec un modèle d'angle de contact dynamique est mis en oeuvre pour tenir compte de ce type de géométrie des bobinages où le film liquide s'écoule par-dessus. Tout d'abord, l'algorithme PISO équilibré est développé, améliorant le calcul des gradients dans l'équation de la quantité de mouvement, et modifiant l'algorithme de Rhie et Chow. Cette méthode révisée assure que la force de tension superficielle et les gradients de pression sont discrétisés de manière identique au même emplacement. De plus, l'algorithme de Rhie et Chow est modifié en intégrant la force de tension superficielle, pour équilibrer les forces de pression. La méthode de la fonction de hauteur est intégrée au code CONVERGE CFD, remplaçant la fraction de vide lisse (SVF) pour une estimation de la courbure. Par la suite, l'angle dérivé du modèle d'angle de contact dynamique est utilisé pour modifier la courbure des cellules d'interface murale. Une explication approfondie de l'algorithme est fournie, ainsi que les cas de test de simulation et leur corrélation avec les données expérimentales.
S'appuyant sur les travaux précédents, un ensemble de simulations est mené pour étudier les phénomènes de mouillage de l'écoulement liquide sur une surface complexe plate. En cette occasion, la surface est sèche, et le phénomène de mouillage est étudié. Cette partie présente la méthodologie de simulation numérique utilisée pour modéliser ces phénomènes, en plus des résultats de la simulation. Une analyse détaillée de ces résultats est présentée, notamment les effets de la méthode de calcul de la courbure, la variation de l'angle de contact d'équilibre et du nombre de Reynolds

Mots clés : Modélisation CFD, Moteurs électriques—Refroidissement, Transfert de chaleurs, Algorithme PISO équilibré, Fonction de hauteur, Angle de contact dynamique, Écoulement de film liquide sur une surface complexe

Well-balanced PISO algorithm, Height Function, Dynamic contact angle, Liquid film flow over complex surface

Abstract: The challenge of constructing a solver for the simulation of oil cooling in electric motor end-windings is the focus of this study. The initial segment concentrates on heat transfer phenomena of liquid film flow over a pre-wetted, complex surface. The goal is to understand the interaction mechanisms between the liquid and the intricate surface. A detailed analysis of the simulation results, taking into account the effects of varying parameters like Reynold number and Prandtl number. Following this, an accurate VOF two-phase flow solver coupling with a dynamic contact angle model is implemented to take into account this kind of geometry of windings where the liquid film flows over. Firstly, the Well-balanced PISO algorithm is developed, improving the calculation of gradients in the momentum equation, and modifying the Rhie and Chow algorithm. This revised method ensures that the surface tension force and pressure gradients are discretized identically at the same location. Additionally, the Rhie and Chow algorithm is modified by incorporating the surface tension force, to equilibrate the pressure forces. The Height Function method is integrated into the CONVERGE CFD code, replacing Smooth Void Fraction (SVF) for a curvature estimate. Subsequently, the angle derived from the dynamic contact angle model is utilized to modify the curvature of the interface wall cells. A thorough explanation of the algorithm is provided, along with the simulation test cases and their correlation with experimental data. Building upon previous work, a set of simulations are conducted to study the wetting phenomena of liquid flow over a flat complex surface. On this occasion, the surface is dry, and the wetting phenomena is studied. This part introduces the numerical simulation methodology used to model these phenomena, in addition to the simulation results. Detailed analysis of these results is presented, including the effects of curvature calculation method, varying the equilibrium contact angle and Reynolds number.

Keywords: Computational fluid dynamics, Electric motors—Cooling, Heat—Transmission, Well-balanced PISO algorithm, Height Function, Dynamic contact angle, Liquid film flow over complex surface

ACKNOWLEDGMENTS

As I conclude this chapter of my academic journey, I am filled with profound gratitude for the numerous individuals who have contributed to the successful completion of my PhD thesis.

First and foremost, I want to thank my parents, uncles, and all my family members. Your unwavering support, love, and encouragement have been the foundation of my success. You have stood by me through every challenge and celebrated every milestone. I am deeply grateful for your sacrifices and the strength you've given me throughout this journey.

I extend my deepest appreciation to my thesis director, Mr. Frédéric Plourde, who granted me the opportunity to pursue my thesis, changing my life in unforgettable ways. His guidance and encouragement have been instrumental, and I am profoundly grateful to him.

I also wish to express my thanks to Mr. Matthieu Fénot for his consistent guidance and support throughout this journey. My sincere gratitude goes to Mr. Guillaume Vinay, who has meticulously followed and supported me for three years, providing sage advice, trust, and valuable recommendations, especially in discussions of scientific issues. It was a privilege to know him and to have conducted my thesis under his supervision.

I would also like to thank Mr. Olivier Laget and Ms. Adèle Poubeau for their assistance, guidance, and valuable advice, as well as for providing solutions to scientific challenges.

Special thanks to Mr. Balachandar and Mr. Ruyer-Quil for your thorough review and insightful comments on my thesis as reviewers. Your detailed critiques have not only enhanced my work but also prepared me for its defense.

To the esteemed jury members—Mr. Balachandar, Mr. Ruyer-Quil, Mr. Dominique Legendre, Ms. Nadia Caney, and again, Mr. Guillaume, Mr. Plourde and Mr. Matthieu—thank you for your time, rigorous evaluation, and the constructive discussions during my defense. Your engagement and thoughtful remarks have been greatly appreciated and have enriched my understanding of my research area.

This achievement would not have been possible without the collective support of my family and academic mentors. I am truly fortunate to have had such a strong network of support, both personal and professional, throughout this challenging but rewarding journey

Contents

Table of figures

Table of tables

Chapter 1

Cooling Techniques for Electric Motors

An overview of the electric motor and its associated thermal challenges is provided. This also highlights the current cooling techniques for electric motors and outlines the objectives of this thesis.

1.1 Introduction

In the last few years, electric motors have attracted the attention of the automotive industries, and researchers all over the world due to the benefit of environmental impact. The trend to design a more compact high-power electric motor is associated with new thermal management challenges. The heat generated inside an electric motor comes from many factors such as magnetic losses, Joule losses, and mechanical losses. Therefore, several parts in the engine will have to work in a stricter mode. In particular, the current capacity in the conductor will increase in some cases, causing the heat loss caused by the Joule effect to dramatically increase (the temperature of the coil rises rapidly because the heat produced is proportional to the square of the current). In addition, the compact design of the engine will reduce the space required for cooling. For this reason, a reasonably high effective cooling method needs to be developed to help the engine operate stably and safely.

In our project, the active convection cooling strategy is studied, where the heat from the end-windings of the electric motor will be directly absorbed by the oil and transferred to the surroundings.

1.2 Electric motor structure

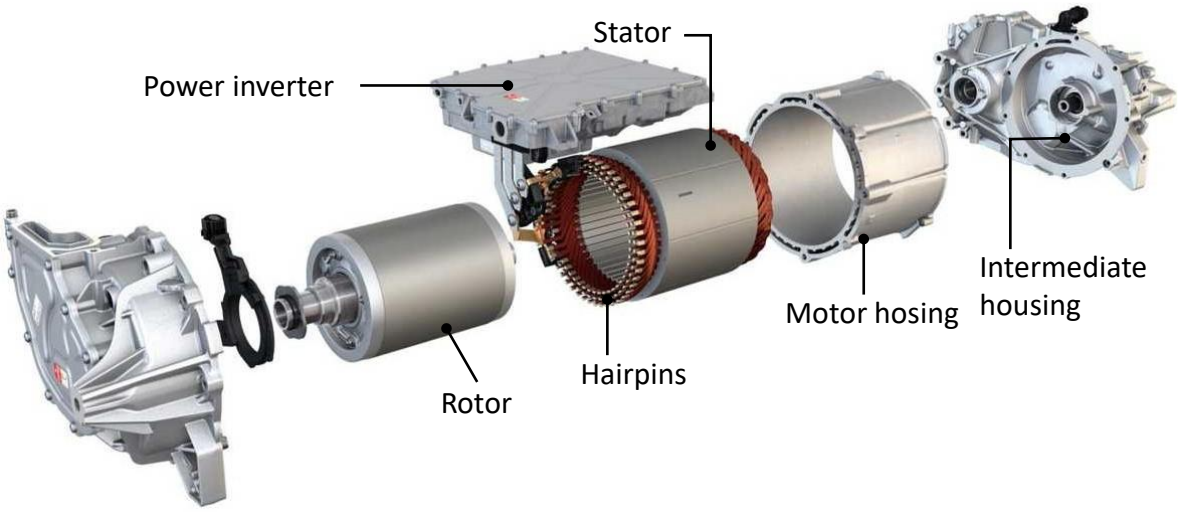

Figure 1: Main components of an electric motor [1]

The structure of an electrical machine consists of different parts, as presented in Figure 1. In this configuration, the main machine components are the following: windings (made of coils), stator

laminations, rotor laminations, motor housing (or frame), and eventually the magnets (in electrical machines with permanent magnets).

1.3 Thermal Issues

The heat generated inside an electric motor comes from several factors such as magnetic losses, Joule losses, and mechanical losses [2,3]. The heat source of Joule losses comes from the conversion of electric energy to thermal energy when the current flows through the conducting material such as copper winding in the stator part. The magnitude of the heat energy follows the Joule–Lenz law: I^2R where I is the electric current and R is the electric resistance of the conductor.

The magnetic losses or iron losses come from 2 main aspects: hysteresis loss and eddy current loss. Hysteresis loss is caused by molecular friction in a ferromagnetic material under an alternating magnetic field, and eddy current loss is caused by the induction of eddy current in the core and conductors held in a magnetic field. Also, in an electric motor, the heat generated by the mechanical energy is mainly due to mechanical friction and viscous friction.

As stated above, the heat sources of electric motors come from a few different parts making their thermal management a complex challenge. It can be summarized as follows [4]: "Heat transfer is as important as electromagnetic and mechanical design. The analysis of heat transfer and fluid flow in motors is actually more complex, more nonlinear, and more difficult than the electromagnetic behavior". Due to the complexity of motor components and heat sources, the heat generated is distributed unevenly inside the electric motor and depends on the motor type and operating conditions.

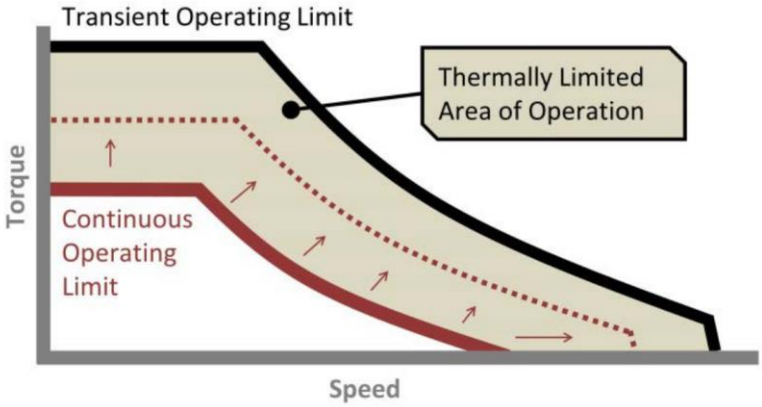

Figure 2: Thermal management impact on motor performance to support increased power [5]

The proper thermal management of the electric motor not only increases reliability but also minimizes the effect of changes in material properties, which are directly related to the torque envelope and efficiency, as shown in Figure 2. As a consequence, many researchers and organizations are developing effective cooling techniques to overcome the thermal problem.

The main type of heat transfer inside an electric motor can be specified as below:

Conduction heat transfer in the motor components

Convection phenomenon specifically in airgap and end-windings

1.4 Cooling method for electric motor

The cooling study of an electric machine designed to achieve promising electrical objectives has a critical influence on its performance. Bertin [6] has studied the main possibilities and issues of heat removal in electric machines.

Nowadays, the importance of finding modern cooling solutions to keep temperatures in the machine at acceptable value is rising. In reality, these machines are required to provide high-efficiency and huge power values, specifically when applied for propulsion in the acceleration phase of the car, compared to what was designed in the previous decades. Many institutions and researchers have tested, explained, and evaluated different cooling methods for automotive traction engines [5,7,8].

Two possible strategies can be adopted to solve the thermal problems encountered. The first strategy consists of finding critical physical parameters that influence the heat transfer (for instance, it could be the structure materials used in motor construction, geometrical factors, or properties of cooling fluids, etc.), and working on optimizing them to fit with the adequate machine thermal design (passive cooling). The other strategy is to focus on developing cooling techniques allowing the highest heat dissipation (active cooling). A review of the literature shows that authors have mainly worked on one of the two strategies for improving heat extraction methods, and few have studied both [4]. Some parts of the machine that are classically cooled must be accurately studied under different electrical and environmental conditions, so that their cooling is adapted to the electrical performance of the machine and improves its overall efficiency. Those parts are mainly the stator, the frame, and the rotor. This study focuses only on the closed-loop active cooling method using Automatic Transmission Fluid (ATF).

As a common aspect, the liquid cooling method offers higher performance in terms of cooling capacity mainly due to the higher specific heat capacity and better convective coefficient of liquids with respect to gaseous coolants. The closed-loop configuration ensures the absence of any foreign particles, but proper sealing must be adopted to avoid any coolant leakage.

1.4.1 Oil injection

As illustrated in Figure 3 , numerical and experimental research studies [9,10] have been carried out on oil injection technology to gain further insight into the configuration, arrangement, and cooling behavior to achieve maximum efficiency. Swales et al. [11] operate a closed-loop oil cooling system for hybrid electric vehicles powertrain motors (Figure 4). From a thermodynamic and physical point of view, oils and, more specifically, Automatic transmission fluids present many advantages: their thermal conductance is similar to water, they also work as good electrical insulators with a low dielectric constant, high dielectric strength, and electric resistivity. Moreover, chemical stability,

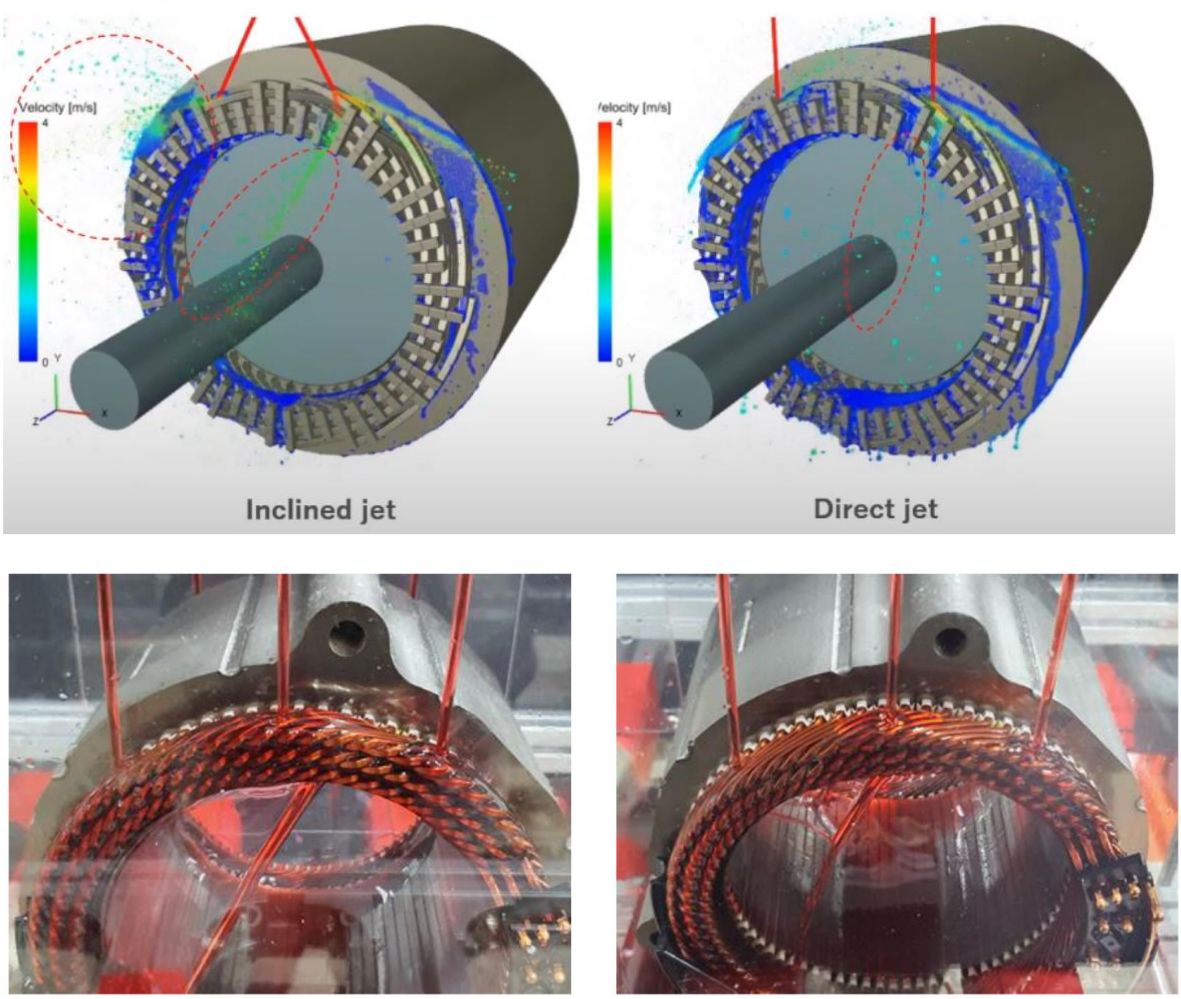

Figure 3: Oil injection on end wingding of the electric motor, numerical and experimental [9,10]

non-flammability are all aspects that make oils a valid alternative to standard fluids. In fact, the motor can be flooded without considering electric or magnetic effects since the ATF is a diamagnetic fluid.

In the considered patent [11], the motor can be in a cooling circuit with the transmission, such as the cooling oil is provided from the transmission itself. Alternatively, this cooling oil can be provided from a separate cooling system. In this embodiment, only a single oil feed is provided from the transmission to the motor: a top port delivers cooling oil for the stator, rotor, and bearings. Figure 4 shows a flow control element which is configured to distribute the oil at desired flow rates to the stator and rotor; it can be a partial or complete ring. A dam member is connected or integrally formed with a rotor end ring to distribute the cooling oil circumferentially to the stator when the cooling oil is thrown outward towards the stator by centrifugal force. Moreover, a structure on the bearing retainer allows the oil to flow from the flow control element to the bearing. In conclusion, this patent describes an efficient cooling loop. In fact, by choosing proper oil, the cooling performances of the system can be high since the thermal oil properties are better than air, as mentioned above. On the other hand, the viscosity of the oil itself must be taken into account. Higher hydraulic losses have to be prevented: a specific pumping system is needed as well as an additional heat exchanger for oil cooling.

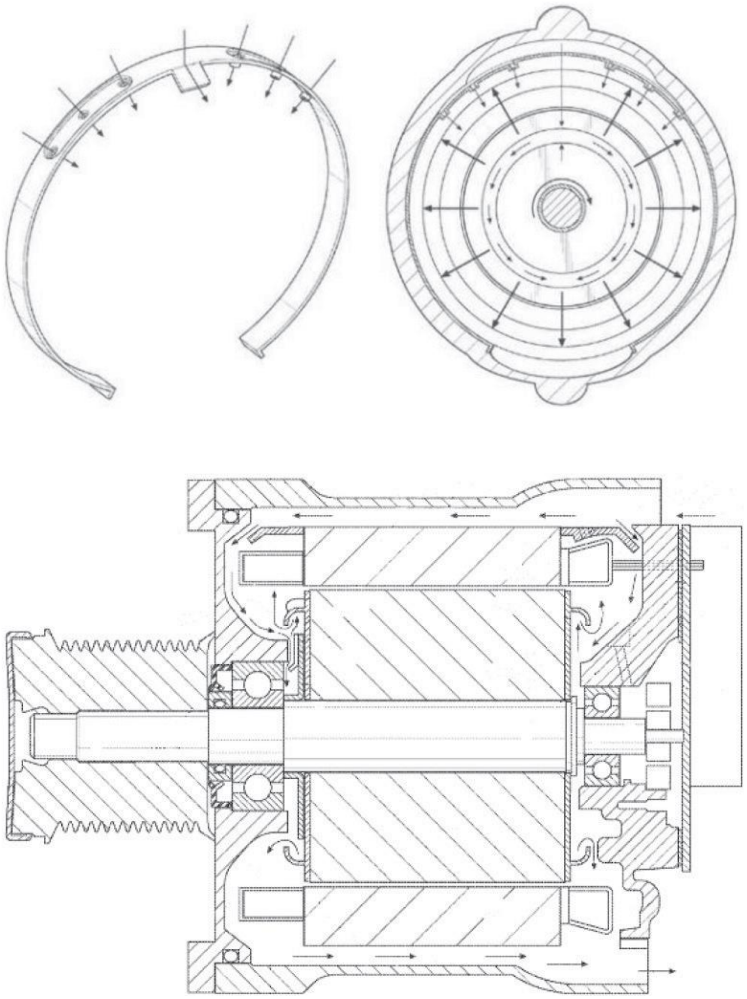

Figure 4: (a) Oil distribution parts (b) Oil cooling system. The coolant flow path is the black arrows [11]

1.4.2 Oil spraying

Oil spraying for cooling electric motors is also investigated by researchers [12–15]. Davin et al. [8] detailed the validation of the oil spray cooling, and the results have been compared against a reference motor with air cooling. Lubricating oil is injected as a coolant on both sides of the machine to cool the stator coil end-windings directly. Figure 5 reports the test motor layout. As it can be observed, the oil is injected through proper nozzles located near the flanges. The coolant is collected at the bottom by gravity and is then recirculated. Different types of nozzles have been analyzed with various oil spray patterns and distributions inside the motor. Figure 6 provides a useful sketch for flow visualization. As the oil film may not be equally distributed along with the stator coils, the cooling of the motor may not be uniform as well.

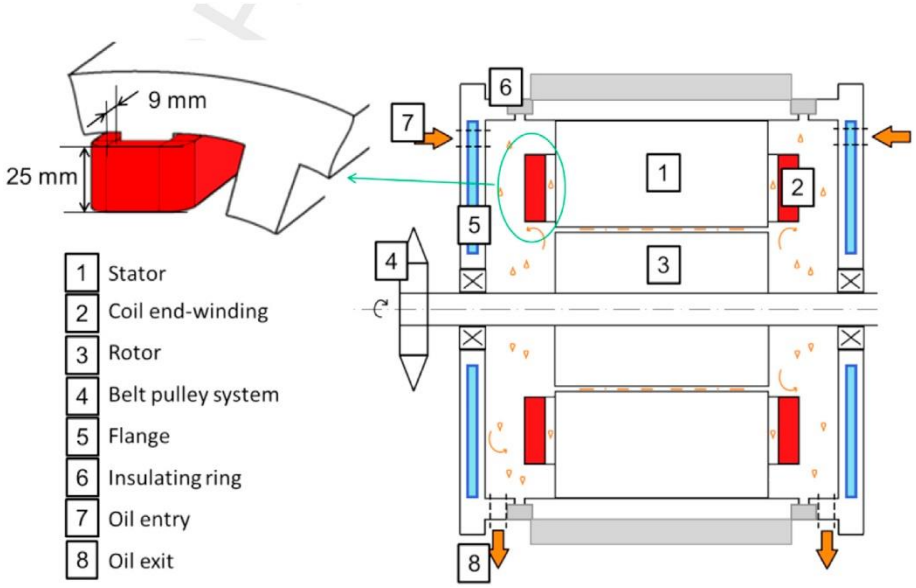

Figure 5: Experiment setup for end-winding cooling [8]

1.5 Objectives of the doctorate

The direct impingement of a jet into an electric stator chamber presents a myriad of multiphysics challenges. These complexities arise from conditions within the end-winding stator chamber, such as strong airflow caused by rotor rotation and the intricate surface geometry of the end windings (Figure 7). Accurate simulation and evaluation of heat transfer performance in this flow environment are particularly challenging, especially for Computational Fluid Dynamics CFD.

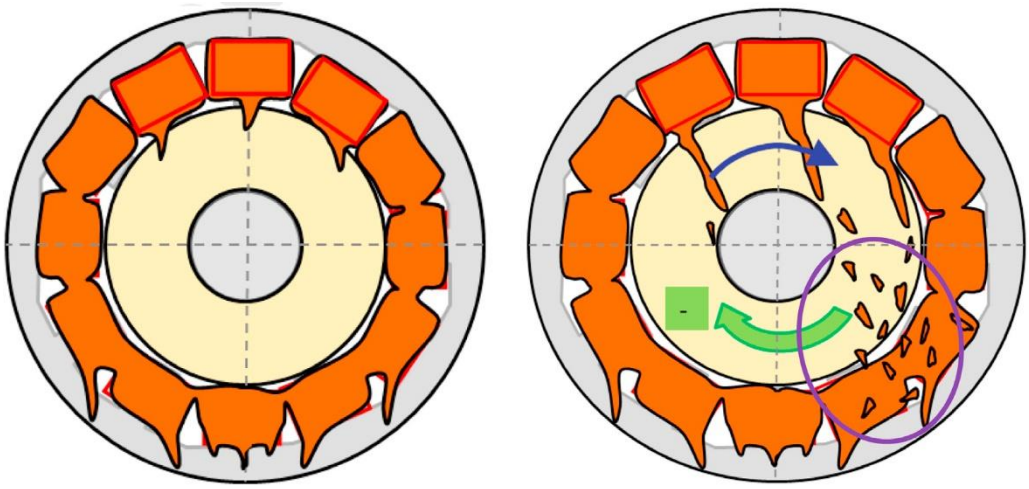

Figure 6: Sketch of oil distribution observed at null and low rotation speed [8]

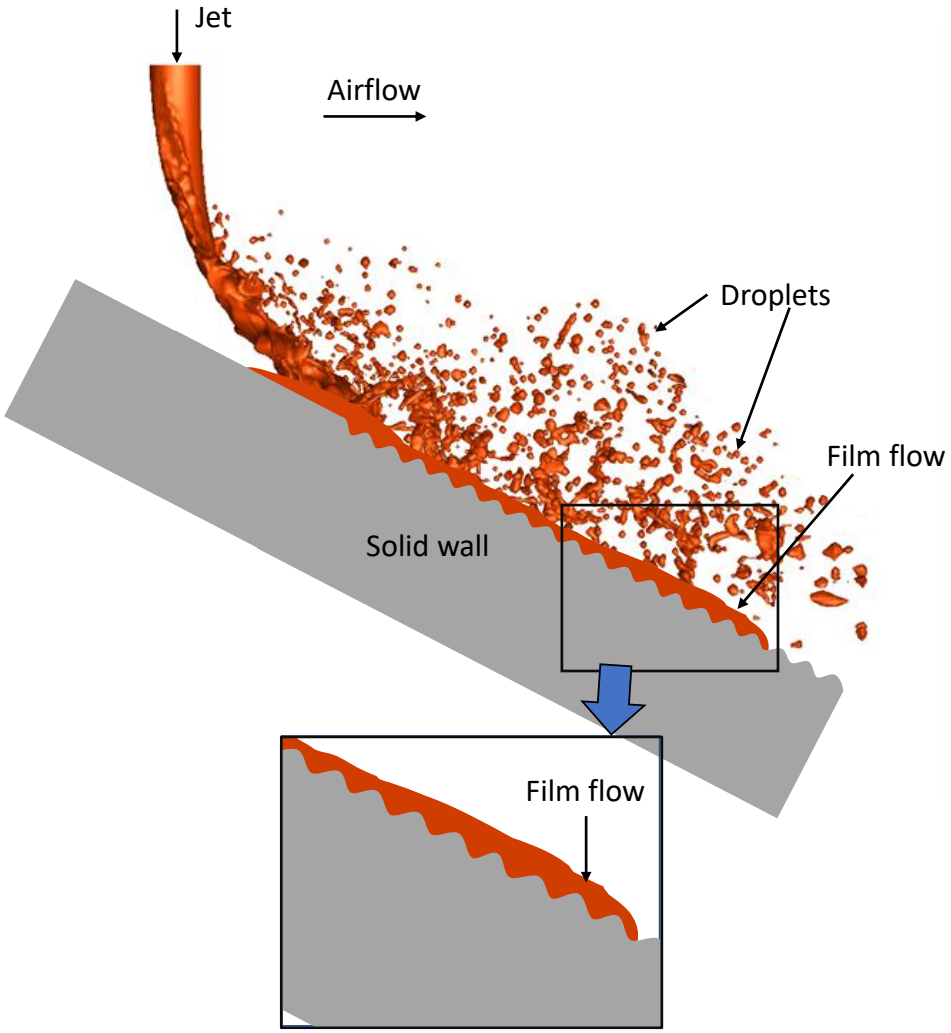

Figure 7. Schematic representation of multiphysics challenges in jet impingement on complex solid surfaces

To address these multifaceted issues, our department is breaking down the larger problem into smaller, more manageable tasks that can be solved sequentially before being integrated. Each segment is assigned to different team members for specialized focus.

In the context of my doctoral project, the objective is to develop a numerical methodology that can effectively simulate a liquid film flow generated by a jet impinging upon the end-windings of an electric motor (Figure 7). Given the naturally complex geometry of the end-windings and the critical role of liquid topology in heat transfer, a sophisticated two-phase flow solver is essential. This solver must be coupled with a dynamic contact angle model to accurately account for the complexities involved in the winding geometry where the liquid film flows.

The organization of the dissertation is as follows:

Chapter 1: Provides an overview of electric motors and their cooling methods.

Chapter 2: Discusses the physical phenomena related to liquid film flow and wetting.

Chapter 3: Introduces the numerical methods employed for simulating two-phase flows.

Chapter 4: Focuses on presenting the results of heat transfer interactions between the liquid and various solid surfaces within the context of film flow. It should be noted, however, that the current Converge CFD code is insufficient for capturing the complexities of film flow over intricate surfaces.

Chapter 5 outlines new developments aimed at enhancing the original two-phase flow algorithms within the commercial CFD code, Converge (https://convergecfd.com). These enhancements are specifically designed to better adapt to the unique challenges posed by two-phase flows in end-winding cooling. They include:

- Well-balanced methods
- Height functions method
- Dynamic contact angle model

Chapter 6: Is devoted to validating these new methods, confirming their effectiveness and accuracy.

Chapter 7: Showcases the application of these newly developed methods on complex surfaces, offering a detailed analysis of the results.

Chapter 2

Physical phenomena involved in liquid cooling

Understanding the physical phenomena involved in liquid film flow is crucial. What is surface tension? Why is it important to the film flow and the physical phenomena of a liquid's wettability when it wets a dry surface? Since wetting behavior is rate-dependent, a mathematical contact angle model, which varies based on the liquid's speed, is needed to represent wettability accurately.

2.1 Surface tension

The liquid is one of the four primary states of matter (the others being solid, gas and plasma), where the molecules attract each other and create an incompressible and constant volume state. When the attraction force is greater than the thermal agitation, the molecules come together to change from a gas phase to a liquid phase, but unlike solids, they are still disordered. At the atomic scale, there are two types of molecules, those in the bulk liquid are attracted to other molecules by cohesive forces in all directions and are in a free and "happy" state [16], whereas the molecules outside the liquid only meet the surface and subsurface molecules, resulting in a net inward cohesive force (Figure 8).

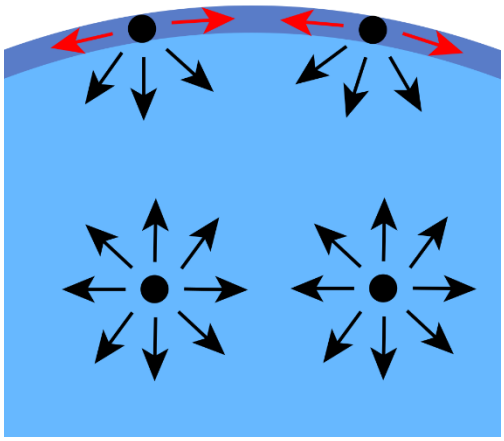

Figure 8: Diagram of the cohesive forces on molecules of a liquid

When a molecule is on a surface, it is in an unfavorable energy state because it loses half of its cohesive interactions. If *F* is the cohesive force of a molecule within the bulk region, then a molecule located at the surface is roughly $F/2$. As the surface tension represents the energy per unit surface area, if a is the molecule size and a^2 the exposed area, then the surface tension is defined as $\sigma \cong F/(2a^2)$. In a sample of oil, the interaction is the van der Waals force, $F \cong kT$, which is thermal energy. Hence for example at 25°C, $kT \approx \frac{1}{40} eV$ which gives $\sigma \approx 20\, mN/m$. Likewise, the surface tension between common oils and air are given in Table 1:

Table 1: Surface tension of common fluids [17]

Name	Surface tension at 20 °C in mN/m
Benzene	28.9
Ethanol	22.1
Propanol	23.7
Water(WA)	72.8
Tetrahydrofuran(THF)	26.4
Methanol	22.7
Mercury	425.4
Isopropanol	23.0
n-Octane(OCT)	21.6
n-Hexane(HEX)	18.4
Glycerol(GLY)	64.0
Carbon Disulfide	32.3

Mercury exhibits the strongest cohesive force at room temperature up to 425 mN/m; water also has a relatively high surface tension up to 72 mN/m, thanks to hydrogen bonds.

Although the origin of the surface tension can be explained at the molecular scale, σ is the macroscopic parameter and is used as explained below.

2.1.1 In terms of energy

As explained by De Gennes [16], surface tension is the energy that must be supplied to increase the surface area by a unit. Suppose someone wants to move the molecules to increase the surface area by an amount of dS, then the work, δW, required to do this can be defined as below:

$$\delta W = \sigma dS \quad (1)$$

2.1.2 In terms of force

In terms of force, the surface tension of the liquids is the force per unit length. As illustrated in Figure 9, a rod bent into three sides to form a rectangle, another rod can roll freely and perpendicularly on two sides of the rectangle. When this system is immersed into bubble soap, for example, as soon as the apparatus is removed from the liquid, the mobile rod immediately moves in the direction of the arrow, meaning that the liquid film exerted a force on the movable rod in order to reduce its surface area. The magnitude of this force, called capillary force, depends on the surface tension of the liquid, and the work needed to move the rod by a distance dx is:

$$\delta W = Fdx = 2\sigma l dx \tag{2}$$

Where l is the circumference of the rod in contact with the liquid.

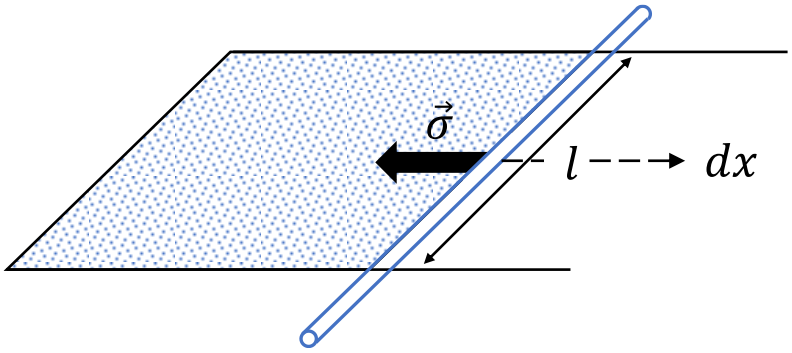

Figure 9: An example to illustrate the capillary force

The four pictures in Figure 10 illustrate the beautiful effect of surface tension in nature.

2.1.3 Laplace pressure

Laplace published in 1805 that the pressure difference between the inside and outside of the droplet is caused by the surface tension. For instance, a droplet tends to have a spherical shape because it has the lowest surface tension energy. For a spherical droplet of radius R, the work done by the surface tension force and pressure to displace the interface by an amount dR is (Figure 11):

$$\delta W = -p_w dV_w - p_0 dV_0 + \sigma dS \tag{3}$$

Where $dV_w = -dV_0 = 4\pi R^2 dR$ is the volume of the droplet, $dS = 8\pi R dR$ its surface area, p_w and p_0 are the pressure inside and outside of the droplet, and σ is the surface tension.

At the equilibrium state, $\delta W = 0$ then Equation (3) becomes:

$$\Delta p = p_w - p_0 = 2\frac{\sigma}{R} \tag{4}$$

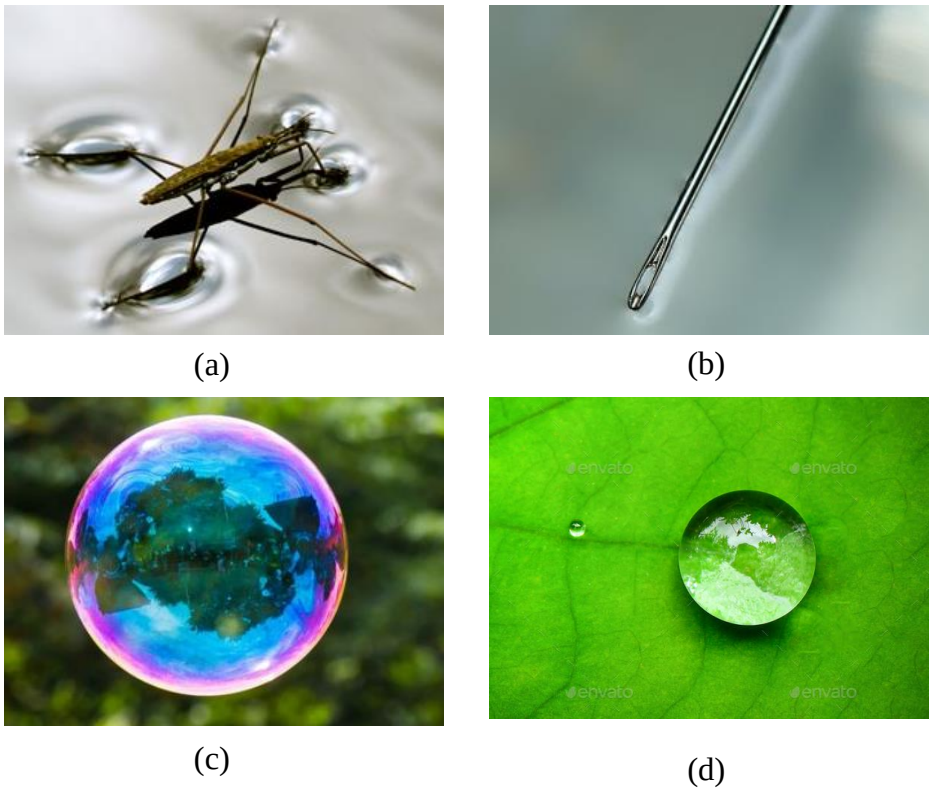

(a) (b)

(c) (d)

Figure 10: Pictures illustrating different phenomena based on interfacial tension (a) a gerris walking on water (b) a needle floating on the water surface (c) a soap bubble floating in the air (d) a water drop on a lotus leaf

Thus, when crossing a curved interface, a pressure jump occurs by an amount Δp. According to (4) the smaller the droplet, the greater the inner pressure.

In most configurations, the curvature is not constant. An example of interface element whose main radius of curvature in the two orthogonal planes are R_1 and R_2 (Figure 12).

The mechanical equilibrium of the interface implies that the resultant of surface tension and pressure forces are zero. The mechanical balance at the interface according to the normal gives:

$$\vec{F}_{tension} + \vec{F}_{pressure} = 0 \tag{5}$$

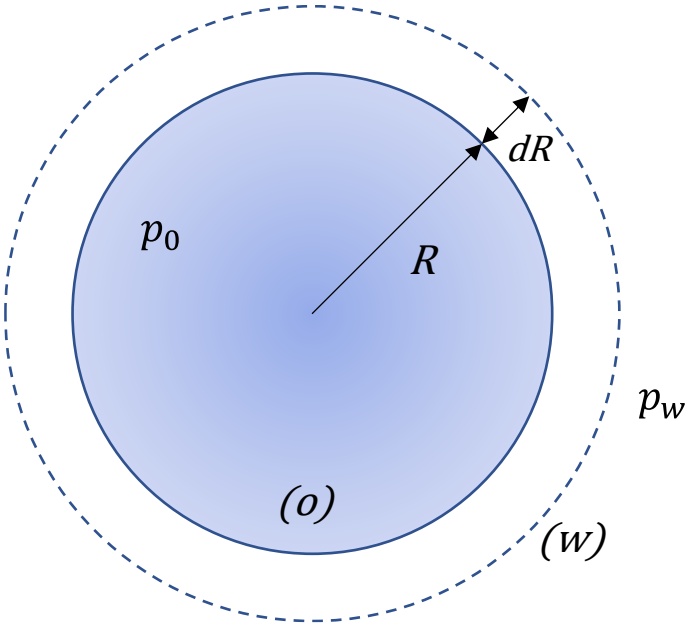

Figure 11: Overpressure inside a drop *(o)* and outside *(w)*

where

$$\vec{F}_{tension} = [-2\sigma R_1 d\theta_1 \sin\left(\frac{d\theta_2}{2}\right) - 2\sigma R_2 d\theta_2 \sin\left(\frac{d\theta_1}{2}\right)]\,\vec{n} \tag{6}$$

Because $\frac{d\theta_2}{2}$ and $\frac{d\theta_1}{2}$ are really small compared to 1, Equation (6) can write as:

$$\vec{F}_{tension} = -\sigma d\theta_1 d\theta_1 (R_1 + R_2)\,\vec{n} \tag{7}$$

$\vec{F}_{pressure}$ can be written as:

$$\vec{F}_{pressure} = ((p1 - p2)(\,R_1 \sin(d\theta_1)\;\; R_2 \sin(d\theta_2)))\,\vec{n} \tag{8}$$

At first-order, the pressure force is reduced to:

$$\vec{F}_{pressure} = ((p1 - p2)(\,R_1 d\theta_1\; R_2 d\theta_2)\vec{n}$$

Finally, the total force balance is written:

$$p1 - p2 = \sigma \frac{R_1 + R_2}{R_1 R_2} \tag{9}$$

Or

$$p1 - p2 = \sigma(\frac{1}{R_1} + \frac{1}{R_2}) \tag{10}$$

Where $\frac{1}{R_1} + \frac{1}{R_2} = \kappa$ is the curvature of the interface.

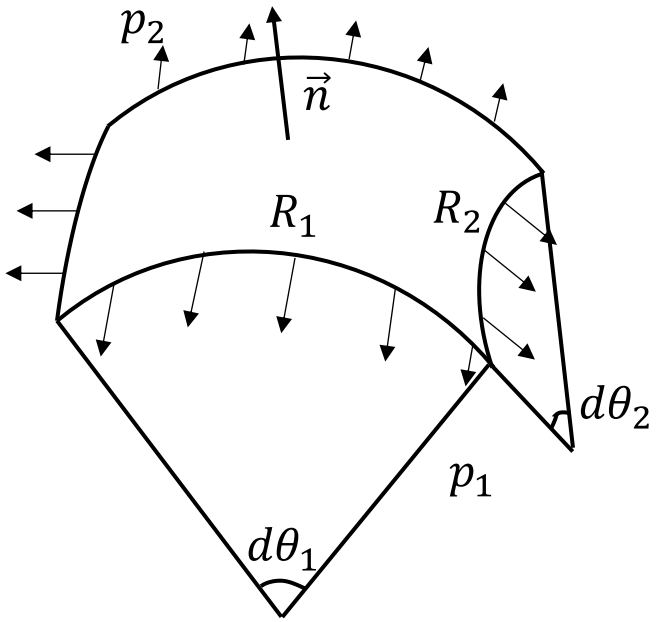

Figure 12: Mechanical equilibrium of a curved interface

2.2 Wettability

2.2.1 Thermodynamics

Consider the static droplet placed on the solid surface. If its volume is assumed to be tiny, then it takes the shape of a spherical cap in order to minimize its energy, and gravity becomes negligible compared to the other forces. The contact angle is the angle measured in the liquid at the liquid-gas interface with the solid surface, as illustrated in Figure 13. It determines the wettability characteristics of the solid surface, and it can also reflect the relative strength of molecular interaction between liquid, solid, and gas. For a given gas/liquid system placed on a perfectly flat solid surface at given pressure and temperature, there is a unique equilibrium contact angle.

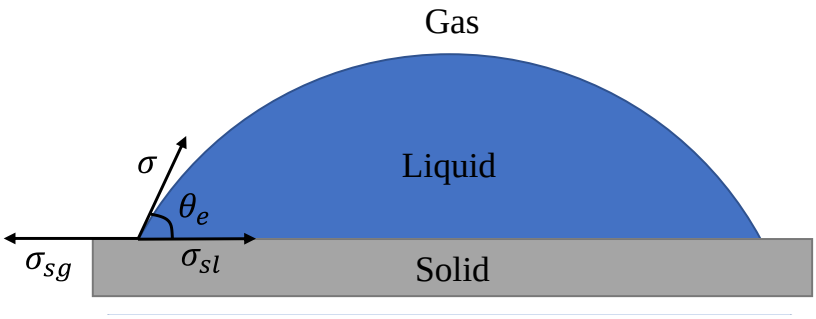

Figure 13: Balance of the forces that act on the triple contact line

The contact angle at equilibrium is determined by Young's Equation. Since the force at the triple contact line is at equilibrium, the equation relating the contact angle and the surface tensions is:

$$\sigma_{sg} - \sigma_{sl} - \sigma_{lg} cos\theta_e = 0 \tag{11}$$

Where σ_{gl}, σ_{sl} and σ_{sg} are the surface tensions for gas-liquid, liquid-solid, and gas-solid interfaces, respectively and θ_e is equilibrium contact angle.

However, this simple Equation (11) doesn't include the energy at the contact line. Pethica [18] modified the Young Equation by defining a line tension for a liquid droplet on an ideal solid surface. This led to the modified Young's Equation

$$cos\theta_e = \frac{\sigma_{sg} - \sigma_{sl}}{\sigma_{lg}} + \frac{\varsigma}{\sigma_{lg}} \frac{1}{a} \tag{12}$$

Where ς is the line tension, and a is the radius of the spherical cap.

2.2.2 Advancing and receding angle

As described in the thermodynamic section, when a droplet is placed on a clean, perfect, and flat solid surface, the contact line will form an equilibrium θ_e contact angle with the wall, defined by Young's Equation.

On the surface that is not perfectly flat, the static contact angle is not unique. For example, if a drop on a solid surface (Figure 14(a)) is deflated, the contact angle θ can reduce down to a limiting value θ_r, at which angle the contact line suddenly moves. This specific value is called receding contact angle.

Likewise, as the drop is inflated (Figure 14(b)), the contact angle increases and exceeds the equilibrium contact angle, but without contact line moving. The contact angle still increases until it reaches a threshold value θ_a , called the advancing contact angle, where the contact line finally starts to move.

This phenomenon can also be observed by inclining the solid surface where the larger contact angle at the front is the advancing contact angle, and the smaller contact angle at the rear of the droplet is the receding contact angle (Figure 14(d)).

Finally, to summarize, the advancing contact angle is the maximum contact angle just before the contact line moves. The receding contact angle is the minimum contact angle just before the contact line moves.

The hysteresis phenomenon is defined as the difference between the two limiting contact angles: the advancing and receding angle.

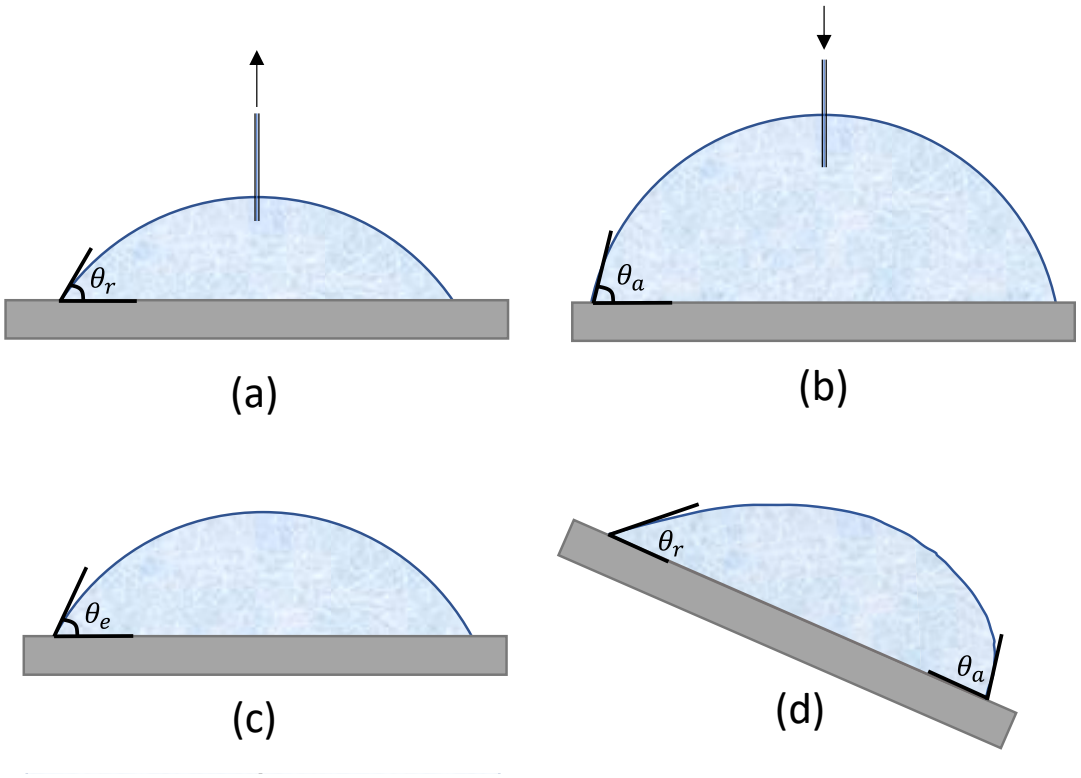

Figure 14: Contact angle hysteresis: (a) receding contact angle, (b) advancing contact angle, c) static contact angle (d) contact angles of the droplet on the inclined surface

The equilibrium contact angle can be calculated from the advancing and receding contact angle using the theoretical equation by Tadmor and confirmed by experiment [19]:

$$\theta_e = \arccos\left(\frac{r_a cos\theta_a + r_r cos\theta_r}{r_a + r_r}\right) \quad (13)$$

Where r_a and r_r are the reference parameters:

$$r_a = \left(\frac{sin^3\theta_a}{2-3cos\theta_a+cos^3\theta_a}\right) \text{ and } r_r = \left(\frac{sin^3\theta_r}{2-3cos\theta_r+cos^3\theta_r}\right). \quad (14)$$

2.2.3 Adhesion energy

As depicted in Figure 14 (d), when inclining the solid surface, the gravity force makes the droplet move down. But the droplet remains at rest on the surface until the θ_a threshold angle is reached. The force that holds the droplet at rest is due to the adhesion force against gravity. To characterize this effect for a droplet on a solid surface, Young-Dupre [20] defined a so-call solid-liquid adhesion energy W_{sl}:

$$W_{sl} = \sigma_{sg} + \sigma_{lg} - \sigma_{sl} \quad (15)$$

By combining Equation (11) and Equation (15), the Young-Dupré Equation can be derived as:

$$W_{sl} = \sigma_{lg}(1 + cos\theta_e) \quad (16)$$

2.2.4 Effect of roughness on wetting

The wetting of a liquid on a solid surface is impacted not only by the surface chemistry but also by the surface topography. Two distinct models, developed independently by Wenzel [19] and Cassie [21,22] are commonly used to explain the effect of surface roughness on the apparent contact angle of liquid drops.

Wenzel model

$$cos\theta = r_r cos\theta_{smooth} \quad (17)$$

where θ_{smooth} is the contact angle measured on a smooth surface of the same material, given by Young's Equation and r_r is the ratio of the actual area of the rough surface to the projected area.

Cassie model

The Cassie model postulates that the hydrophobic nature of a rough surface is caused by microscopic pockets of air remaining trapped below the liquid droplet, leading to a composite interface. Φ is the solid area fraction of the projected wet area, r_f is the roughness of the solid−liquid interface. Cassie equation yields [23]:

$$cos\theta = -1 + \Phi\ (1 + r_f cos\theta_{smooth}) \tag{18}$$

The two models consider different behaviors of a liquid droplet on a surface. The Wenzel model considers a liquid droplet that seeps in between the irregularities of a rough surface. The Cassie model considers a liquid droplet that sits on top of the irregularities, with a layer of air trapped between the irregularities beneath it (Figure 15).

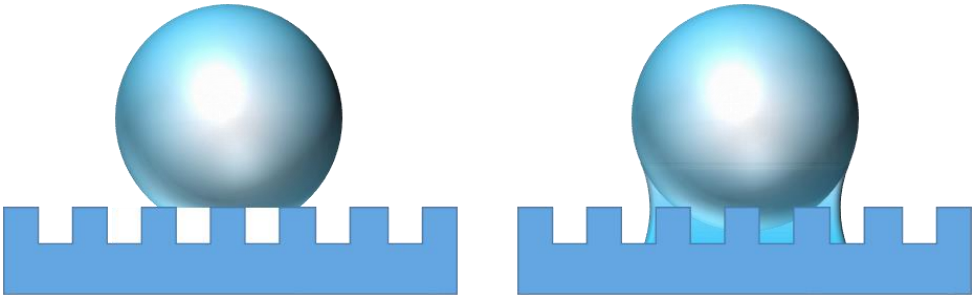

Figure 15: Schematic of Cassie state and Wenzel state [24]

2.3 Dynamic contact angle models

In this section, the origin of the contact angle phenomena as well as the dynamic contact angle model are presented in detail;

As mentioned in Section 2.2, the contact angle is formed by the adhesion force between liquid, gas, and solid phase. For liquid moving quickly over a surface, the contact angle can be altered from its value at rest. The advancing contact angle will increase with speed and the receding contact angle will decrease. The discrepancies between static and dynamic contact angles are closely proportional to the capillary number. Many researchers have carried out experiments from the macro to the atomic scale to better understand the origin of dynamic contact angle [27]. Extrand [25,26] conducted experiments on a flat surface with a heterogeneous island as shown in Figure 16. The solid part in Figure 16 (a) was made of a silicon wafer with native oxide layer, while the solid part (Figure 16 (b), (c)) has an additional heterogeneous island obtained by depositing a drop of polystyrene (PS). First, the drop of water was deposited on the clean silica surface. The drop spreads on this solid surface

until it reaches the equilibrium contact angle $7 \pm 3°$. The next test is illustatred in Figure 16 (b) where the drop of water is deposited such that the contact line of the water droplet is on the periphery of the heterogeneous island; the contact angle equal $95 \pm 2°$. In the third test illustrated in Figure 16 (c), Extrand initially did the same test as second experiment, but then he gradually adding more water to the droplet, hence the contact line is expanded. Right after contact line touch silica surface, the contact angle changes abruptly from $95 \pm 2°$ to $7 \pm 3°$. Hence, the contact angle is not affected by the material under the drop, but rather by the material near the contact line.

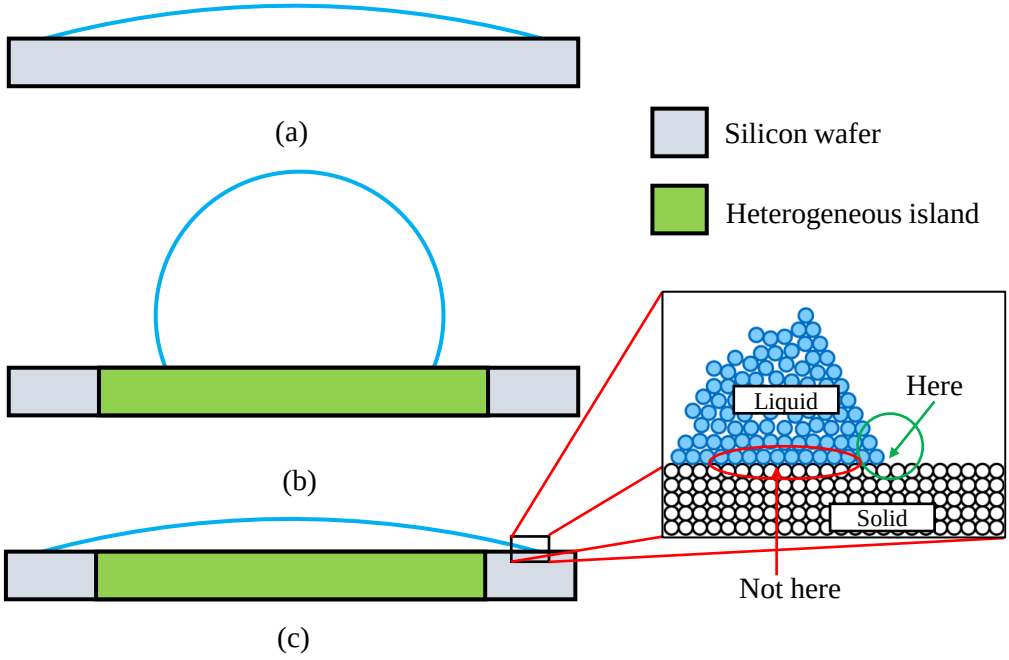

Figure 16: Wetting experiments [25,26]

To better understand hysteresis phenomena, for the first time Liu et al. [27] use helium ion microscopy to observe the ubiquitous 3D nanoscopic distortion along the contact line at the atomic scale (Figure 17).

The base material was mica, Silicon wafer and Copper plate with a Root Mean Square (RMS) roughness of 0.12 nm, 0.42 nm and 10.32 nm respectively. Though at the micro scale (100 μm) the contact line seems smooth, numerous nano distortions and wrinkles appear at the nano scale (500 nm). As shown by the experiment, if the material is absolutely smooth, all hysteresis phenomena and thus the dynamic contact angle will disappear. However, the atomic roughness can trigger these phenomena.

In their conclusions, Liu et al. [27] explain that the hysteresis phenomena, coming from the difference between advancing and receding contact angle is due to the static and dynamic friction of the contact line with the solid surface; increasing roughness leads to increasing hysteresis angle.

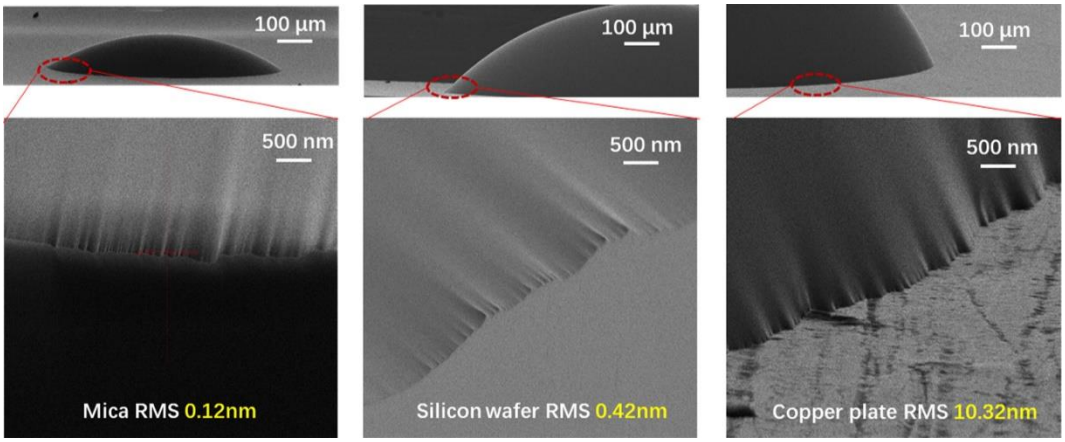

Figure 17: 3D nanoscopic morphology of the close contact line region using helium ion microscopy [27]

Thought it is possible to simulate the motion of the contact line at the molecular scale [28], this approach is not considered in our study.

At the macro scale, a conflict emerges between the classical condition of adherence of fluid to the wall and the tangential motion of the contact line at velocity V_{cl}. Reconciling the two leads to a singularity in the expression of viscous stresses τ_{xy}.

$$\tau_{xy} \approx \mu \frac{V_{cl}}{\Delta} \tag{19}$$

τ_{xy} is the stress generated by a contact line. Δ is the mesh size.

Indeed, the viscous stresses τ_{xy} tend towards infinity when the mesh size tends towards 0. Many researchers developed models of dynamic contact angle to overcome this singularity such as Quasi-dynamic, Kistler's dynamic [29], Shikhmurzaev [30], Cox's model [31,32].

Following Sikalo et al. [33], the dynamic contact angle depends on many parameters such as:

$$\theta_d = f(\theta_e, Ca, We, \mu_l, \dots) \tag{20}$$

θ_e is the static or equilibrium contact angle, Ca is the Capillary number, We is the Weber number and μ_l is the dynamic viscosity of the liquid.

The Capillary number is a dimensionless number representing the ratio of viscous forces to surface tension forces acting across an interface between two liquids and is defined as:

$$Ca = \frac{Viscous\ force}{Surface\ tension} = \frac{V_{cl}.\mu_l}{\sigma_{lg}} \tag{21}$$

V_{cl} is the contact line velocity, μ_l the viscosity of the liquid and σ_{lg} the surface tension coefficient.

The Weber number is a dimensionless number that compares the inertia force to the surface tension force:

$$We = \frac{Liquid's\ inertia}{Surface\ tention} = \frac{u^2\rho_l D}{\sigma_{lg}} \tag{22}$$

Where u is the velocity of the droplet just before impacting the wall, ρ_l is the liquid density, and D is the diameter of the droplet.

2.3.1 Quasi-dynamic contact angle model

The quasi-dynamic model is the simplest dynamic contact angle model. Fixed advancing or receding contact angle is imposed as a boundary condition. Though it is the most basic dynamic contact angle model, it is widely used in the literature (Olsson [34,35]). This model can be represented by two equations as:

$$\theta_d = \theta_a \quad if \quad V_{cl} \geq 0 \tag{23}$$

$$\theta_d = \theta_r \quad if \quad V_{cl} < 0 \tag{24}$$

2.3.2 Kistler's dynamic contact angle model

The empirical dynamic contact angle model developed by Kistler (1993) is based on Hoffman's empirical function (Hoffman, 1975). In this correlation, the dynamic contact angle depends on the static contact angle and the contact line velocity through Ca number. The model is valid for advancing contact lines only.

$$\theta_d = f_H(Ca + f_H^{-1}(\theta_e)) \tag{25}$$

Where f_H is the Hoffman's function (f_H^{-1} is its inverse) and defined as:

$$f_H(\theta_e) = cos^{-1}(1 - 2\tanh\,(5.16((\frac{\theta_e}{1 + 1.31{\theta_e}^{0.99}})^{0.706})) \quad (26)$$

If the advancing contact angles are available, θ_e in Equation (25) and Equation (26) can be replaced by them depending on the velocity direction.

2.3.3 Shikhmurzaev's model

The second empirical model is Shikhmurzaev's model [36]. This model is also dependent on the contact line velocity, through Ca number and the equilibrium contact angle. But it is also dependent on three phenomenological constants fitted to experiments (a_1, a_2, a_3). The model is based on the theory that the solid-liquid and the liquid-gas interfaces have specific thermodynamic properties, which means that they behave like real phases, and that the contact line motion is a result of mass exchange between these two phases.

Shikhmurzaev's model is based on the relationship between several parameters as described below:

$$\cos(\theta_d) = \cos(\theta_a) - \frac{2u_d(a_1 + a_2u_r)}{(1 - a_2)(a_1 + u_d^2)^{0.5} + u_d} \quad (27)$$

For the advancing phase, Equation (27) can be written as:

$$\theta_d = cos^{-1}\left(\cos(\theta_a) - \frac{2u_d(a_1 + a_2u_r)}{(1 - a_2)(a_1 + u_d^2)^{0.5} + u_d}\right) \quad (28)$$

Where a_1 is a constrain for the equilibrium state, which is defined as:

$$a_1 = 1 + (1 - a_2)(cos(\theta_a) - a_4 \quad (29)$$

while a_2 is the dimensionless surface density, u_r is the radial velocity at the interface contact with the solid part.

$$u_r = \frac{\sin(\theta_d) - \theta_d\cos\,(\theta_d)}{\sin(\theta_d)\cos(\theta_d) - \theta_d} \quad (30)$$

And u_d is the dimensionless contact line velocity defined as:

$$u_d = a_3 \frac{V_{cl}\mu_l}{\sigma_{l-g}} \tag{31}$$

For glycerol, the experiments conducted by Blake and Shikhmurzaev [30] determined the constant phenomenological parameters:

$$a_2 = 0.63, a_3 = 4.3, a_4 = -0.08 \tag{32}$$

2.3.4 Cox's model

This dynamic contact angle model is based on the asymptotic theory developed by Cox (1986), Hocking and Rivers (1982), Ngan and Dussan V. (1982) and Dussan et al. (1991), and is valid for both advancing and receding contact lines. It can be written as:

$$\theta_d = g^{-1}\left(g(\theta_{app}) + Ca\ log\left(\frac{L}{\lambda}\right)\right) \tag{33}$$

θ_{app} is the apparent contact angle in the macroscopic region which can be calculated from Ca and θ_e such as used in Afkhami [37], Sui and Spelt [38] or imposed to θ_d and θ_r as in Legrendre and Maglio [39]. L is the length scale and λ is the physical slip length. The g function can be depicted as:

$$g(\theta) = \int_0^{\theta} \frac{x - \sin(x)\cos(x)}{2\sin(x)} dx \tag{34}$$

To compare these four different dynamic contact angle models, the study of Gohl et al. [40] are introduced, where they studied these four different types of dynamic contact angle models to test the difference. The dynamic contact angle has been implemented by modifying the curvature at the near-wall interface. For validation, the authors used glycerol droplets impacting a solid surface with a small impact velocity (low Weber number). The results in Figure 18 show the importance of the dynamic contact angle model on two-phase flow simulation.

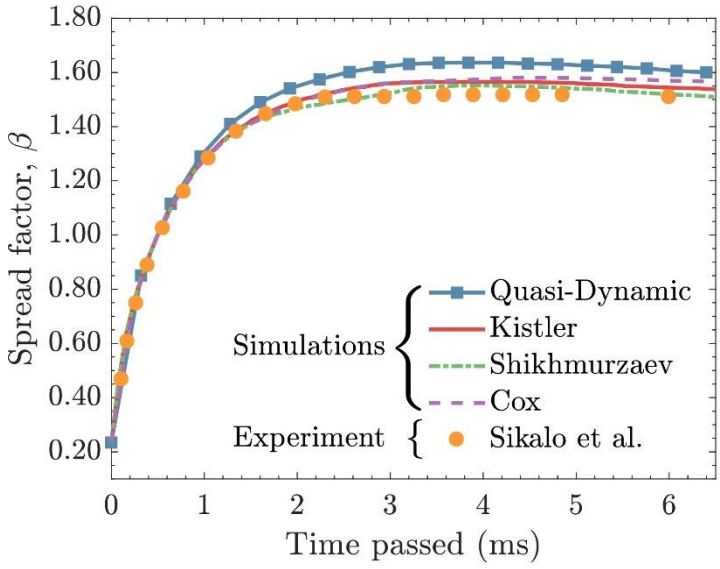

Figure 18: Evolution of spreading factor [40]

2.4 Conclusion

Details of the physical phenomena involved in two-phase flow are elaborated upon in this chapter. Firstly, the root of surface tension is explored, which arises from the interactions between the atomic forces of a liquid. Its appearance in two-phase flow and the mechanics behind it are explained, allowing for the calculation of surface tension forces. Subsequently, wettability is discussed, defined as the force that arises between atoms of a solid surface, liquid, and gas. Since wetting behavior is rate-dependent, a mathematical dynamic contact angle, which varies based on the liquid's speed, is needed to represent wettability accurately. The dynamic contact angle are presented, with an outline of models attempting to calculate the actual contact angles of a liquid in various states (equilibrium, advancing, and receding).

Such understanding is crucial for the development of models that accurately capture surface tension and wettability during the numerical development phase.

Chapter 3

Numerical Methods for Two-phase Flow

The actual method of solving two-phase flow numerically is detailed, along with the mathematical principles behind the scenes. The general equations governing two-phase flows and the numerical methods employed to solve them are discussed.

3.1 Governing equations for incompressible two-phase flows

In this study, a one-fluid set of Navier-Stokes equations for incompressible two-phase flow is used. The continuum conservation equation is:

$$\nabla u = 0 \tag{35}$$

The momentum conservation equations can be written as:

$$\rho\left[\frac{\partial u}{\partial t} + \nabla.(uu)\right] = -\nabla p + \nabla[\mu\nabla u + \mu(\nabla u)^T] + F + \rho g \tag{36}$$

where u is the velocity, p is the pressure, g is the gravity and $F = \sigma\kappa\delta_s\mathbf{n}$ is the surface tension force; σ is the surface tension coefficient, κ and $\mathbf{n}$ the surface curvature and the normal to the interface, respectively; δ_s is the Dirac function expressing the fact that the surface tension term is only concentrated at the interface. To solve Equation (36), it is necessary to know the viscosity μ, density ρ and surface tension force of the liquids. Hence, an equation that can track the position of the interface over time is required. In this present study, the VOF-PLIC (VOF Piecewise-Linear Interface Calculation) method [41–44] is used to describe the interface between the two fluids.

3.2 Finite Volume Method

In this study, the finite volume method is used to discretize the continuous equations and the flow variables are calculated and stored at the center of the cells. By applying the integral operator on Equation (36) in a single cell with the volume V as depicted in Figure (16), and then using the Green-Gauss theorem, the continuous equations can be discretized. For example, by applying the Green-Gauss theorem to the integral convection term, the new equation can be written as:

$$\int_V [\nabla.(uu)]dV = \int_S [u(u.\hat{n})]dS \tag{37}$$

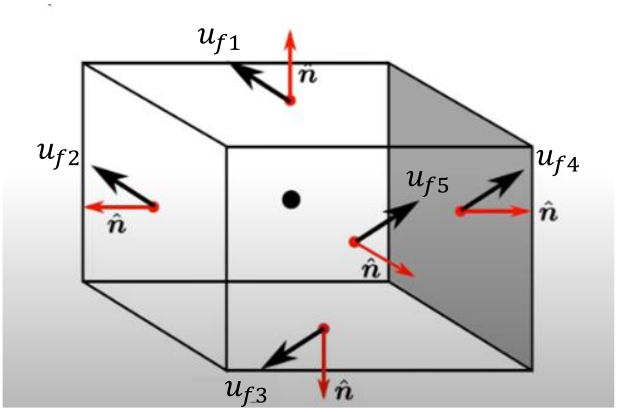

Figure 19: Representation of the face center velocity on a control volume V

where $\int_S$ represents the integral on the face, $\hat{n}$ is the normal vector on each face. Then Equation (37) can then be written as:

$$\int_S [u(u.\hat{n})]dS = \sum_{i=1}^{M} \int_S [u_i(u_i.\hat{n}_i)]dS_i \tag{38}$$

where M is the number of faces of the control volume. Equation (38) can be written as [45]:

$$\sum_{i=1}^{M} \int_S [u_i(u_i.\hat{n}_i)]dS_i = \sum_{i=1}^{M} [u_{fi}(u_{fi}.\hat{n}_{fi})]S_i \tag{39}$$

Where u_{fi} is the face center velocity as shown in Figure 19. By doing the same for each term in Equation (36), this equation can be discretized totally.

In Section 3.4, the description of how to solve these equations with the PISO algorithm [46] will be presented.

3.3 Volume-of-fluid method

When solving only the single-phase Navier-Stokes equation, an additional equation to identify the two fluids is added to the transportation indicator function to mark the fluids. There are many ways to define the indicator function depending on the method, such as the phase-field method or level-set method, but the VOF method is the most common, which is used in commercial and free CFD software such as Converge, Ansys Fluent, Star-CCM, and Basilisk [46–50].

In VOF method, the location of interface is implicitly tracking by this equation:

$$\frac{\partial C}{\partial t} + u.\nabla \mathrm{C} = 0 \tag{40}$$

where C is the void fraction which is defined in Equation (45). The density and the viscosity are updated as given below:

$$\rho = \rho_1 C + \rho_2(1 - C) \tag{41}$$

$$\mu = \mu_1 C + \mu_2(1 - C) \tag{42}$$

The detail of construct C can represent by a indicator function $H(x,t)$ defined as:

$$H(x,t) = \begin{cases} 1 & if\ x\ is\ in\ the\ fluid\ 1, \\ 0 & if\ x\ is\ in\ the\ other\ fluid. \end{cases} \tag{43}$$

As the assumption of immiscible and incompressible fluids is applied, the material derivative of H is zero. The advection of indicator function can be described as:

$$\frac{DH}{Dt} = \frac{\partial H}{\partial t} + \nabla(u.H) - H\nabla.u = 0 \tag{44}$$

By averaging the indicator function H in each computational cell Ω, the average volume fraction in the cell i is C_i. The indicator function H and the void fraction function C are illustrated in Figure 20; H function has only the value 0 or 1 while the C function can have a value between 0 and 1:

$$C_i(t) = \frac{1}{V}\int_{\Omega} H(x,t)dV \tag{45}$$

where V is the volume of the cell i. By integrating Equation (44) in the computational cell i and using Equation (45), one finds:

$$V\frac{\partial C_i(t)}{\partial t} + \int_{\Gamma}(u.n)H(x,t)\,dS = \int_{\Omega} H\nabla.udV \tag{46}$$

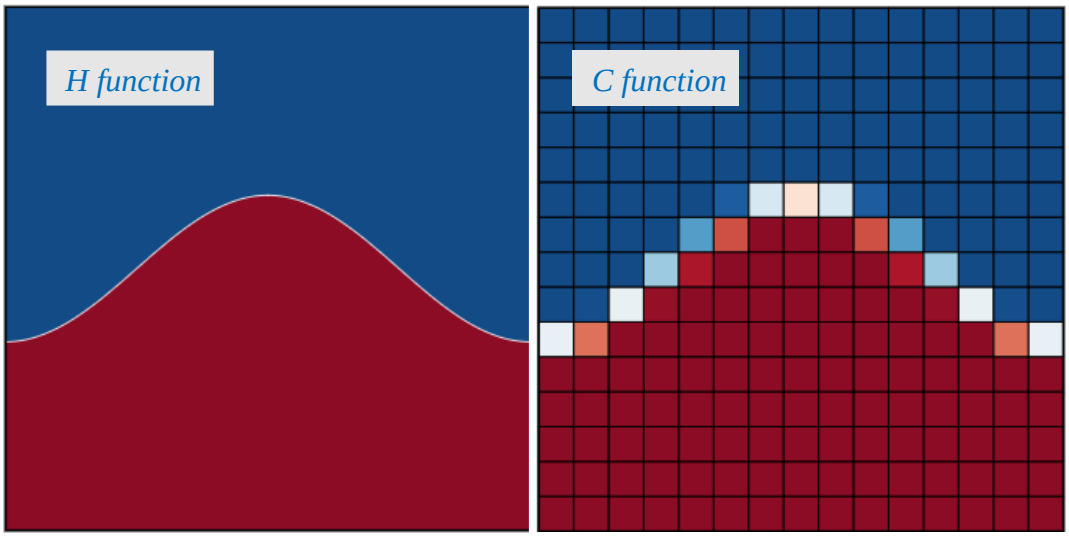

Figure 20: Illustration of VOF method. The indicator function field is on the left. The void fraction field is on the right [51]

Finally, the Equation (46) in time $\Delta t = t^{n+1} - t^n$ can be integrated, and for each direction:

$$\left(C_i^{n+1} - C_i^n\right) = -\tilde{\Phi}_{i+1/2} + \tilde{\Phi}_{i-1/2} + C_i^n\left(\mathrm{u}_{i+1/2} - \mathrm{u}_{i-1/2}\right) \tag{47}$$

Where subscript $i + 1/2$ and $i - 1/2$ indicate the right face and the left face of the computational cell, respectively. To solve Equation (47), the calculation of the flux term $\tilde{\Phi}$ is needed, defined as the amount of C across the face during time Δt. The PLIC method is used to estimate the flux terms accurately by calculated the position of interface in the calculated cell.

3.3.1 PLIC method

The PLIC method is the method used to reconstruct the interface to get the fluxes. There are four steps to do:

Estimate the normal orientation $\boldsymbol{n} = n_1, n_2, n_3$.

Construct the surface with the plane equation:

$$n_1 x + n_2 y + n_3 z + d = 0. \tag{48}$$

Determine d from normal vector and void fraction C.

Solve the void fraction equation.

Step 1: Estimate the normal orientation

Several algorithms have been developed to calculate the normal to the interface. In 1984, Young [52] developed a finite-difference method. For simplicity, the method below is detailed for a 2D mesh, where each coordinate is represented by two indices i, j (Figure 21). The method can easily be extended to 3D.

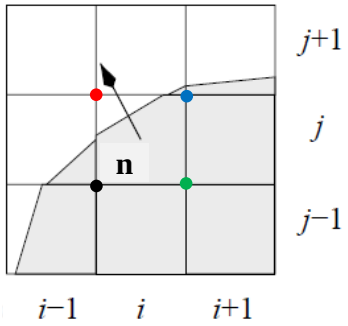

Figure 21: 2D mesh example used to estimate normal vector

In this method, Young estimates the normal vector $\boldsymbol{n}$ as a gradient:

$$\boldsymbol{n}=\nabla \mathbf{C} \tag{49}$$

As highlighted in Figure 21, the normal vector $\boldsymbol{n}$ is evaluated at each node of the mesh. For instance, the two components of the normal vector at the top-right node of cell i (blue point in Figure 21) are calculated as:

$$n_{x:i+1/2,j+1/2}=-\frac{1}{2h}\left(C_{i+1,j}-C_{i,j}+C_{i+1,j+1}-C_{i,j+1}\right) \tag{50}$$

where h is cell side and similarly:

$$n_{y:i+1/2,j+1/2}=-\frac{1}{2h}\left(C_{i,j+1}-C_{i,j}+C_{i+1,j+1}-C_{i+1,j}\right) \tag{51}$$

The normal vector at the cell center is obtained by averaging the value of four nodes as:

$$\boldsymbol{n}_{i,j}=\frac{1}{4}\left(\boldsymbol{n}_{i+1/2,j+1/2}+\boldsymbol{n}_{i+1/2,j-1/2}+\boldsymbol{n}_{i-1/2,j+1/2}+\boldsymbol{n}_{i-1/2,j-1/2}\right) \tag{52}$$

Young's method is robust, but it is not as accurate as the Centered-columns scheme described below. The Centered-columns difference method consist of summing the void fraction in each direction to define the height function ($h_x = f(y)$ and $h_y = g(x)$ for 2D case). For example, in Figure 22(a) and

(b), the heights $h_{y_{i-1}}$ and $h_{x_{j+1}}$ are defined as: $h_{y_{i-1}} = \Delta y \sum_{k=-1}^{1} C_{i-1,j+k}$, $h_{x_{j+1}} = \Delta x \sum_{k=-1}^{1} C_{i+k,j+1}$.

Then the height function in "i" cell is approximated via a linear equation. For example, the height function of the "i" cell in the vertical direction $h_{y_i} = f(x)$ can be written as:

$$sgn(n_y) h_{y_i} = n_x x + l \tag{53}$$

where l is the constant number of a linear line, n_x is the slope of the straight line that can be calculated as:

$$n_x = -\frac{1}{2\Delta y}\left(h_{y_{i+1}} - h_{y_{i-1}}\right) = -\frac{1}{2}\sum_{k=-1}^{1}\left(C_{i+1,j+k} - C_{i-1,j+k}\right) \tag{54}$$

In Equation (53) the sign of the n_y must be calculated explicitly to know the direction of the normal vector because the information on the location of the fluid is lost when summing the void fraction. And the distant l is neglected since it only needs to calculate the normal vector.

Similarly, the height function in the horizontal direction $h_x x = f(x)$ can be linearly approximated by:

$$sgn(n_x) h_{x_i} = -n_y y + w \tag{55}$$

And compute the normal vector n_y based on the horizontal height function as

$$n_y = -\frac{1}{2\Delta x}\left(h_{x_{i+1}} - h_{x_{i-1}}\right) = -\frac{1}{2}\sum_{k=-1}^{1}\left(C_{i+k,j+1} - C_{i+k,j-1}\right) \tag{56}$$

The interface in cell i is now characterized by two different normal vectors. To select between the two normal vectors, as shown in Figure 22 (a), when a line cuts two opposite sides of the stencil 3x3, it gives the correct slope. In this case, in the vertical direction, the interface cuts the left and the right side of the stencil, while in the horizontal direction, the interface does not cut the top and the bottom of the stencil. Hence, in this case, the normal vector estimate based on the vertical direction is more accurate. On the contrary, in Figure 22 (b), the normal vector should be estimated using the horizontal direction height function. Thus, the appropriate normal vector for each cell is chosen according to the following criteria:

$$|n| = min(\lceil n_x \rceil, \lceil n_y \rceil) \quad (57)$$

But there are many cases when the line does not cut the two opposite sides in both directions, as shown in Figure 22 (c). It especially appears for a coarse mesh, that is the drawback of this method.

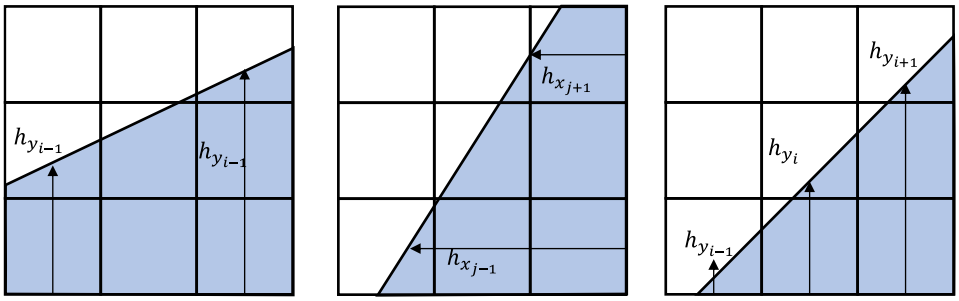

(a) (b) (c)

Figure 22: Volume fraction used to calculate height. (a) column-wise. (b) row-wise. (c) an off-centered scheme

To benefit from the advantages and limit the disadvantages of both Young's scheme and the Centered-columns scheme, Aulisa et al. [53] combined the two methods and named it Mixed Youngs-centered (MYC) method. In this combined method, the normal vector is calculated according to both Young's and Centered-columns method for each direction. Then, the normal vector is chosen for each direction according to the criterion as follows:

$$|n| = min(\lceil n_{x1} \rceil, \lceil n_{x2} \rceil) \quad (58)$$

Where n_{x1} is the slope based on Young's method and n_{x2} is the slope based on the Centered-columns method.

Step 2: Determination of d in Equation (48)

When the normal vector $\boldsymbol{n}$ is specified, the constant value d in Equation (48) needs to be calculated. The key idea to determine d is to represent the grey area in 2D or volume in 3D by a function of d and then use the root-finding algorithm such as Bisection, Newton's method, Steffensen's method to derive the d.

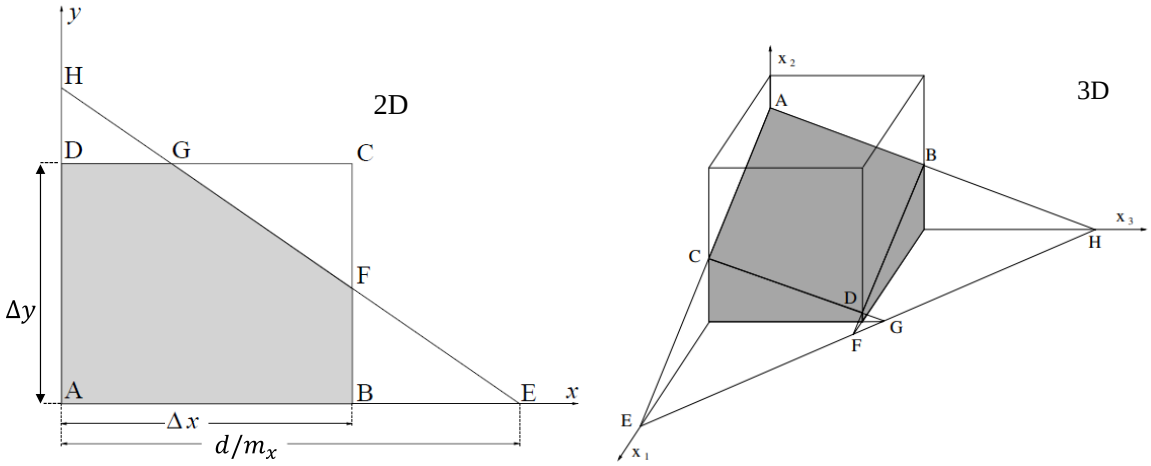

Figure 23: Geometrical basic for 2D and 3D for finding the d parameter of Equation (48). a) The "cut area" is the gray region inside the rectangular cell ABCD. b) The cut volume is the shaded volume inside the grid cell under the polygon ABCD [53,54].

For example, in 2D, the area of ABFGD represent as a function of d that equal $\Delta x \Delta y C$ then the equation can written as:

$$\Delta x \Delta y C = \frac{1}{2 m_x m_y}\left[d^2 - F_2(d - m_x \Delta x) - F_2\left(d - m_y \Delta \mathrm{y}\right)\right] \tag{59}$$

Where $\Delta \mathrm{x}, \Delta \mathrm{y}$ is the size of the cell, m_x, m_y is normal vector determined in the section above, C is the void fraction, $F_2 = z^2$ when z > 0 and zero otherwise. More detail of this method, as well as for 3D extension, can be found in the book of Tryggvason et al. [54].

Step 3: Interface advection

Once the interface is constructed, the flux terms $\widetilde{\Phi}_{k+1/2}, \widetilde{\Phi}_{k-1/2}$ in Equation (47) can be derived, and using the Euler explicit scheme, and set $\tilde{C}_k = C_k^n$:

$$C_k^{n+1} = -\widetilde{\Phi}_{k+1/2} + \widetilde{\Phi}_{k-1/2} + C_k^n\left(\mathrm{u}_{k+1/2} - \mathrm{u}_{k-1/2} + 1\right) \tag{60}$$

3.3.2 Surface Tension Estimation (smooth void fraction)

The calculation of the surface tension term of Equation (36) is based on the continuum surface force (CSF) model of Brackbill [55]:

$$F = \sigma\kappa\delta_s \mathbf{n} = \sigma\kappa\nabla\tilde{C} \tag{61}$$

Where $\tilde{C}$ is a smooth void fraction (SVF) defined by Equation (62):

$$\tilde{C}(x) = \frac{1}{h^3}\int_v \alpha(x')\varphi(x' - x)d^3x' \tag{62}$$

and

$$\varphi(x) = 0 \text{ for } |x| \geq \frac{h}{2} \tag{63}$$

The curvature κ of the interface is calculated as the divergence of the interface normal vector n:

$$\kappa = -\nabla . n \tag{64}$$

with

$$n = \frac{\nabla\tilde{C}}{|\nabla\tilde{C}|} \tag{65}$$

3.4 PISO algorithm for two-phase flow

Before entering the PISO algorithm, VOF advection equation is first solved as detailed in section 3.3. When the new C (volume fraction) field is obtained, density and viscosity are updated from Equation 41 and 42. Then the momentum and continuity equations are solved using the PISO algorithm.

In the PISO algorithm, the first step, also called the predictor step, consists in solving the momentum equation implicitly or semi-implicitly:

$$\rho_c^{n+1}u_c^* = \rho_c^n u_c^n + H^* - \Delta t\rho_c^{n+1}\left\langle\frac{\nabla P}{\rho_f}\right\rangle_{f\to c}^n + \Delta t F^n \tag{66}$$

where the superscript n and $n+1$ represent the current and next timestep, respectively. The superscript * represents the intermediate most up-to-date field values. The subscripts c and f indicate the cell-center and face-center, respectively. H^* represents the convection, diffusion, and source

terms. The angle brackets operator $\langle\,\rangle_{f\to c}$ stands for an averaging of face-center quantity to cell-center. F^n is the surface tension force.

When the new predictor center velocity field is updated in Equation (66), the mass fluxes at the cell's faces need to be evaluated since it is used in Poisson's equation. But in our code, all the transported quantities are collocated at the center of the cell. Hence when using the collocated quantities, there is a decoupling phenomenon between pressure and velocity. This problem can result in fluctuations in the pressure and velocity solution that appear in the checkboard pattern.

However, in 1983 Rhie and Chow proposed a new algorithm to eliminate this problem while maintaining collocated variables. This scheme consists in approximating the effect of the staggered grid but leaving the quantities at the center of the cell. The first term in the RHS of Equation (67) is the average velocity at the cell center. The second and third term of Equation (67) correspond to the pressure gradient term.

$$u^*_{i+1/2} = \frac{u^*_i + u^*_{i+1}}{2} - \frac{dt}{\rho}\left(\frac{P_{i+1} - P_i}{dx}\right) + \frac{dt}{2\rho}\left(\frac{P_{i+1} - P_{i-1}}{2dx} + \frac{P_{i+2} - P_i}{2dx}\right) \tag{67}$$

When the mass fluxes at the cell faces are evaluated, the new pressure is calculated as:

$$\nabla.\left(\frac{\nabla\delta p^*_c}{\rho^n_c}\right) = \nabla.\frac{u^*_i}{\Delta t} \tag{68}$$

Where $\delta p^*_c = p^*_i - p^n_i$. Once the pressure is solved, the velocity can be updated according to Equation (69)

$$\rho^{n+1}_c u^{**}_c = \rho^n_c u^*_c - \Delta t \rho^{n+1}_c \left\langle\frac{\nabla\delta p^*_c}{\rho_f}\right\rangle^n_{f\to c} \tag{69}$$

when velocity is updated, the other transport equations are solved. If necessary, based on the convergence criteria, the correction processes can be repeated, where the convergence criteria based on a tolerance value is represented in Equation (70):

$$\frac{|p^* - p^n|}{|p^*|} \le p_{tol} \tag{70}$$

with p_{tol} is the pressure tolerance value prescribed in the input files. So the PISO algorithm can be summarized as follow:

1. Solve VOF advection Equation (60).
2. Solve the discretized momentum equation to compute an intermediate velocity field Equation (66).
3. Compute the mass fluxes at the cell's faces using Rhie and Chow scheme Equation (67)
4. Solve the pressure Equation (68)
5. Correct the velocities on the basis of the new pressure field using Equation (69)
6. Repeat from 3 depending on the prescribed number of iterations and on convergence criteria.

Go to the next time step and repeat from 1.

3.5 Conclusion

There's a deeper dive into the numerical details required to solve 2-phase flow as utilized in this study. The discussion begins with the Navier-Stokes equation, detailing its general form and the discretization process. Subsequently, the Volume of Fluid method is explained in depth, given its significance in solving two-phase flow. Within the VOF discussion, the process of solving the VOF equation using the PLIC method is elaborated on, as well as how surface tension is estimated and incorporated into the Navier-Stokes equation to complete the mathematical system. The PISO algorithm is also presented to show the procedure for solving the discretized Navier-Stokes equation. This chapter offers a comprehensive understanding of the numerical steps, from the raw equation, discretization, and incorporation of equations for 2-phase flow, to the solving process.

This foundation will be employed for setting up and analyzing 2-phase flow in following chapter.

Chapter 4

Heat transfer enhancement in corrugated falling films

The actual simulation of pre-wet film flow over a corrugated surface is presented (the surface parameter represents the corrugated surface of end-winding). Both the hydrodynamics and heat transfer aspects are simulated and analyzed in detail.

4.1 Introduction

Heat transfer in liquid film flow is a complex phenomenon that plays a crucial role in various engineering applications, such as direct cooling of end windings in electric motors, heat exchangers, and electronics cooling [7,56–58]. The efficiency of these systems is significantly influenced by factors such as the geometry of the flow channel, fluid properties, and flow conditions.

The performance, reliability, and longevity of electric motors depend heavily on efficient cooling mechanisms, particularly for end windings, which are subject to high temperatures during operation [7,57,59]. Direct oil cooling, where some part of the oil flows over the coil surface in a thin film, is an effective method for managing the temperature of end windings. However, the coil surfaces often exhibit complex geometries (Figure 1), necessitating a comprehensive understanding of the hydrodynamic and heat transfer properties of the liquid film flow for effective cooling.

At low Reynolds numbers, the flow in these channels is often laminar and can be modeled as a thin film flowing over the channel walls [60]. In this study, the effects of varying the Reynolds and Prandtl number on the heat transfer characteristics of a thin film flowing over flat and corrugated surfaces are investigated. The Reynolds number is a dimensionless quantity that describes the relative importance of inertial forces to viscous forces in a fluid flow, while the Prandtl number is a dimensionless quantity that describes the relative importance of momentum and thermal diffusivities. The corrugated surfaces used in this study have a corrugated wall configuration. It is based on the size of the actual size of American Wire Gauge (AWG).

This section focusses on the pre-wetting surface, a phenomenon that frequently occurs when direct oil is injected onto the coil surface. Investigating the pre-wetting surface is crucial for understanding the behavior of the liquid film flow and its impact on heat transfer performance. By examining the properties of pre-wetted surfaces and the associated hydrodynamics and heat transfer characteristics, valuable information on the characteristics of film and heat transfer can be obtained to help engineers estimate the best system for increasing the effectiveness of direct oil cooling in electric motor end windings (Figure 25).

The results of this study are used to gain the understanding of the interactions occurring among flow behavior, surface geometry, heat transfer, and fluid properties in such configurations. This

understanding is crucial for implementing a new thermal wall law (a PhD project in our department) for both high and low Pr numbers.

Figure 24. The experiment of Bennion film flow over end winding [57]

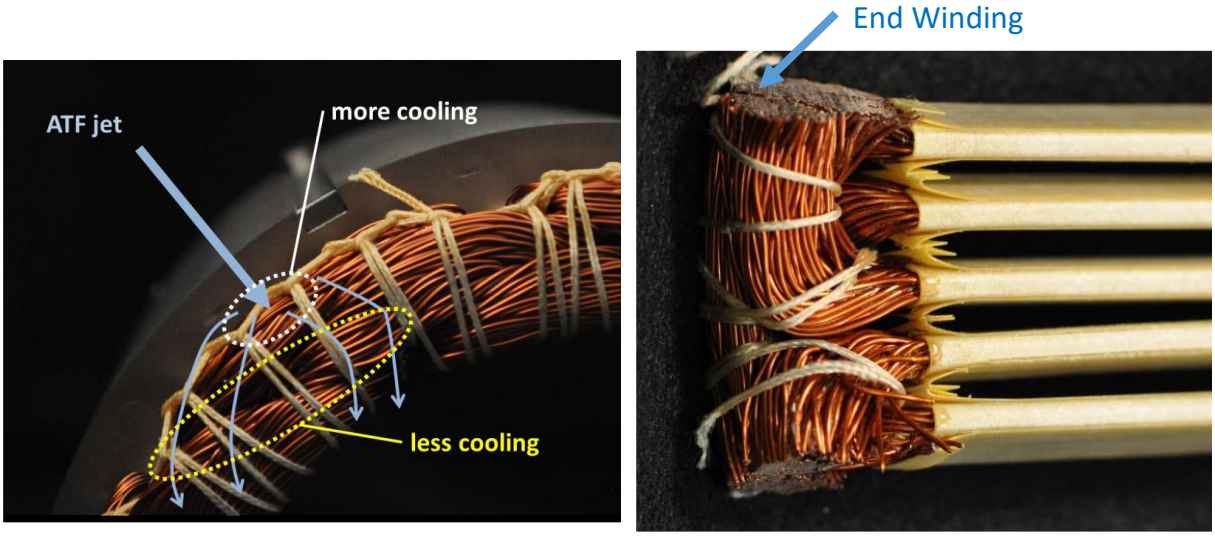

Figure 25: End winding of real electric motor [57]

4.2 Liquid film flow, state of the art

In order to understand prior results and identify potential knowledge gaps related to film flow over corrugated surfaces and heat transfer, a detailed review of relevant studies is provided in this section. Wang and Chen [61] numerically investigate forced convection in a single-phase flow through a periodic array of wavy-wall channels. They find out that the peaks of skin-friction coefficients and

Nusselt numbers occur near the peak of the wavy wall. As the wavy amplitude wavelength ratio (R_{α}) and Reynolds number increase, the local Nusselt number notably increases in the converging section of the wavy-wall channel, while showing a small change in the diverging section (Figure 2). This suggests that corrugated surfaces are effective heat transfer devices at significantly larger amplitude-wavelength ratios, particularly at higher Reynolds numbers. However, it's crucial to indicate that this understanding is based on a single-phase flow model, thereby not accounting for the critical parameters intrinsic to two-phase flows such as the capillary number and surface tension forces.

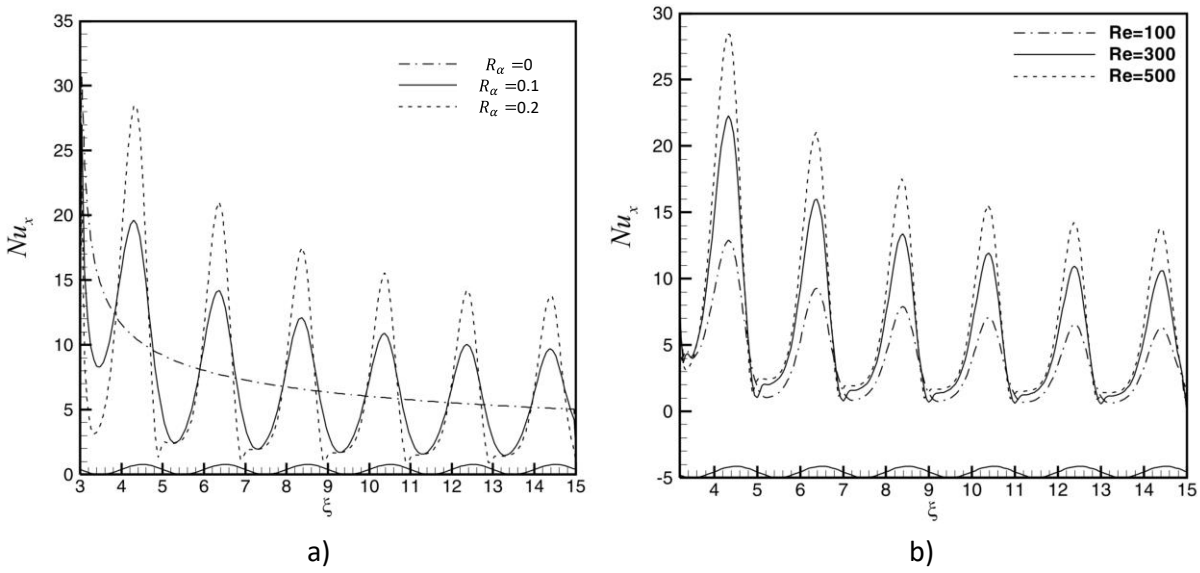

Figure 26. Distribution of Nusselt number at Pr=6.93; a) Re=500; b) $R_{\alpha} = 0.2$ [61]

Similarly, Mehta et al. [62] studied the impact of wall amplitude on the thermal and hydrodynamic characteristics of laminar flow in a corrugated channel. Adopting the same methodological approach as Wang and Chen, they manipulated the channel topologies by progressively increasing and decreasing the corrugation amplitude. The Reynolds number in their study varied from 5 to 200. Their findings highlight that the average Nusselt number exhibits independence from geometric variation at very low Reynolds numbers. However, a significant difference from this trend is observed at a Reynolds number of 200. In this case, the average Nusselt number exhibits a substantial increase, ranging from 10% to 40%, depending upon the geometrical topology of the channel.

Zhao and Cerro [63] experimentally provided a detailed exploration of fluid dynamics on the behavior of liquid films on complex surfaces. They indicated an interesting insight into the behavior of liquid films at different ratios of film thickness to solid surface amplitude (R_{δ}). For large ratios ($R_{\delta} > 1$), the film has a nearly flat surface, while at ratios ($R_{\delta} < 1$), the film starts following the contour of the solid surfaces (Figure 27).

$$R_\delta = \frac{\delta_{film\ theory}}{H} \tag{71}$$

Where $\delta_{film\ theory}$ is film thickness by Nusselt theory, H is the depth of the corrugation or amplitude of corrugation.

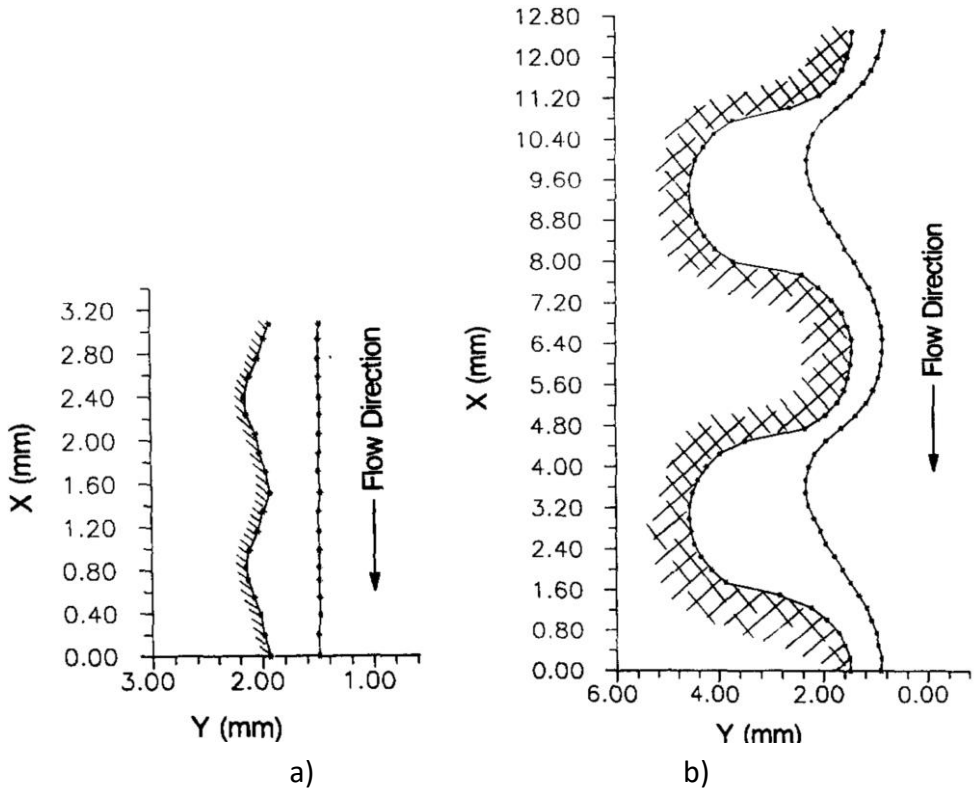

Figure 27. Film thickness on a surface; a) $R_\delta = 2.29$, the free surface is nearly flat b) $R_\delta = 0.258$, the free surface partially follows the contour of the wall [63]

Malamataris and Bontozoglou [64] carried out numerical tests of viscous flow along an inclined wall with varying wall corrugation in the laminar flow regime, similar to the test of Zhao and Cerro [63]. The study finds that the oscillations of the free surface depend on the wall geometry and liquid surface tension. They also indicated that the formation of a recirculation region corresponds to the highest flow rates. However, these are not adequately described due to low mesh resolution and the highly distorted finite element mesh in that region. Similaly, Trifonow [65] numerically studies film flow over a corrugated channel and concludes that while increasing Re, the free surface flattens and becomes parallel to the flow direction. And the average film thickness is away higher than the film thickness calculated by Nusselt theory. Another numerical test about high-viscosity fluids falling

down the vertical wavy wall was carried on by Chen et al. [66]. He points out that the free interface becomes flatter and film thickness is thicker when the viscosity increase.

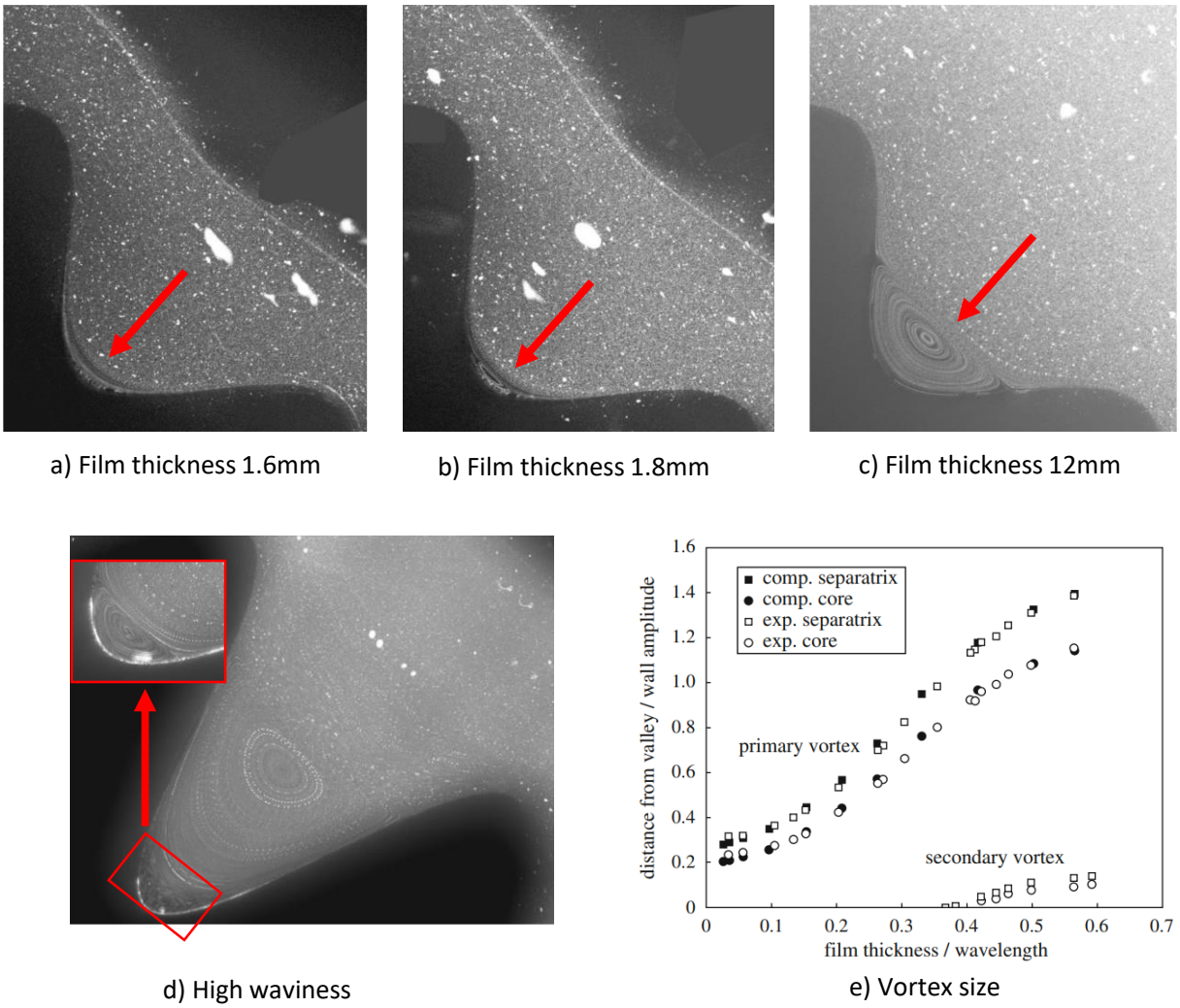

a) Film thickness 1.6mm

b) Film thickness 1.8mm

c) Film thickness 12mm

d) High waviness

e) Vortex size

Figure 28. The effect of film thickness and corrugated profile on the formulation of circulation [67]

Wierschem and Aksel [67] studied the formulation of vortices in film flow over strong corrugated bottom profiles at low Reynolds numbers. This study provides some interesting insights into the behavior of vortices in gravity-driven films on sinusoidal bottom profiles. They clearly indicated that both the waviness (ratio of wave amplitude/wavelength) of the bottom profile and the film thickness play significant roles in the formation of these vortices. Figure 28 a), b), c) show the vortices that appear when the film thickness increase, and when the waviness is very high, the second vortex appear (Figure 28 d), e)). A follow-up experiment [68] was conducted regarding film flow over intensely undulated substrates. The study focused on the impact of inertia on the formation of circulation zones within the channel. The findings revealed that the size of eddies expanded with an increase in

Reynolds number. However, the influence of inertia force in low Reynolds number laminar flow was relatively insignificant.

Scholle et al. [69] applied a novel numerical approach to investigate film flows over corrugated surfaces. They highlighted numerically that conventional methods such as the lubrication approximation and perturbation method were not adequate for channels with strong undulation. They introduced an innovative analytical method that utilized the representation of Stokes equation solutions in the form of holomorphic functions. Their results exhibited a strong correlation with their experimental findings.

There are other studies on film flow and heat transfer over tubes [70–75]. They intensively studied the structure of flow hydrodynamic as well as heat transfer phenomena around the hot tube (Figure 29). Surprisingly, there is a lack of research specifically focusing on the heat transfer of film flow over corrugated surfaces. In this study, the comprehensive research on the film flow over these channels is undertaken, specifically looking into the characteristics of heat transfer.

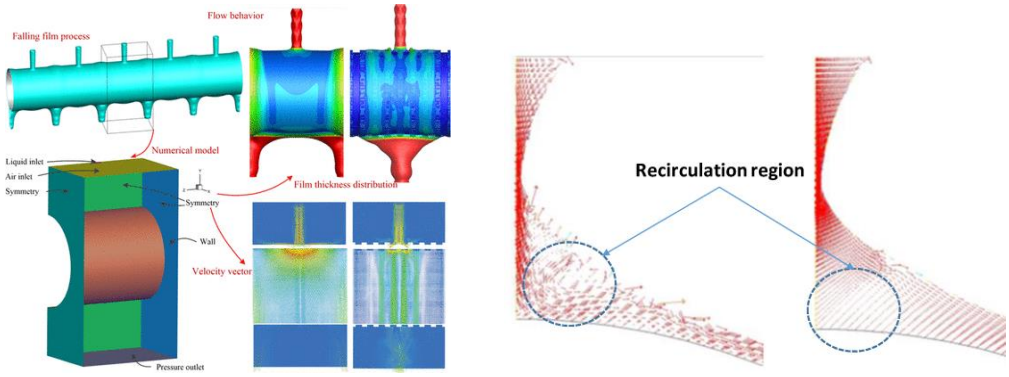

Figure 29. Hydrodynamic and heat transfer of film flow over a tube; a) [75]; b) [74]

4.3 Numerical setup and validation

This section discusses the computational setup, numerical methods, and validation of the VOF PLIC method used in the study. The primary focus is on ensuring the accuracy and reliability of the simulation results for both flat and corrugated surfaces.

4.3.1 Computational domain and boundary conditions

The simulation study utilized two 2D geometries, namely a flat channel and a corrugated channel. The flat channel is characterized by a rectangular inlet section with a length of 1P and a high of 0.64P,

which led to a downstream rectangular section with a length of 49P and a high of 1.96P. On the other hand, the corrugated channel shares the same geometrical dimensions as the flat channel, but with a corrugation pattern based on American Wire Gauge 18, with a wire radius of 0.536P and a corrugation wavelength of P=1.02mm. The corrugation also featured a small radius at the lowest point rounded by a radius of 0.0745P (Figure 30 a)).

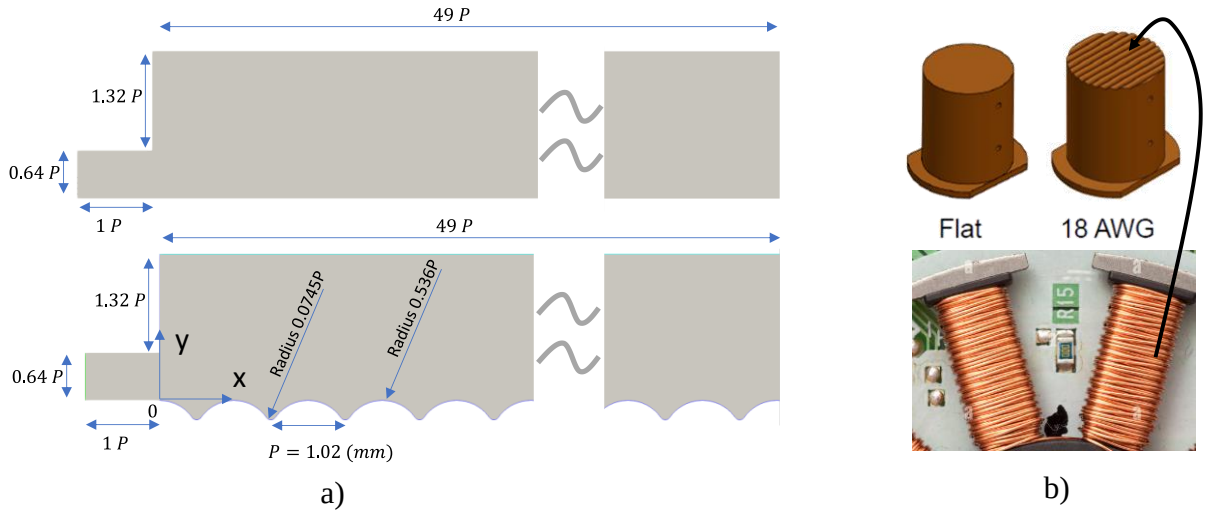

Figure 30. a) Schematic view of the flat and corrugated channel; b) Test surface [59] and the actual electromagnetic coil of an electric motor.

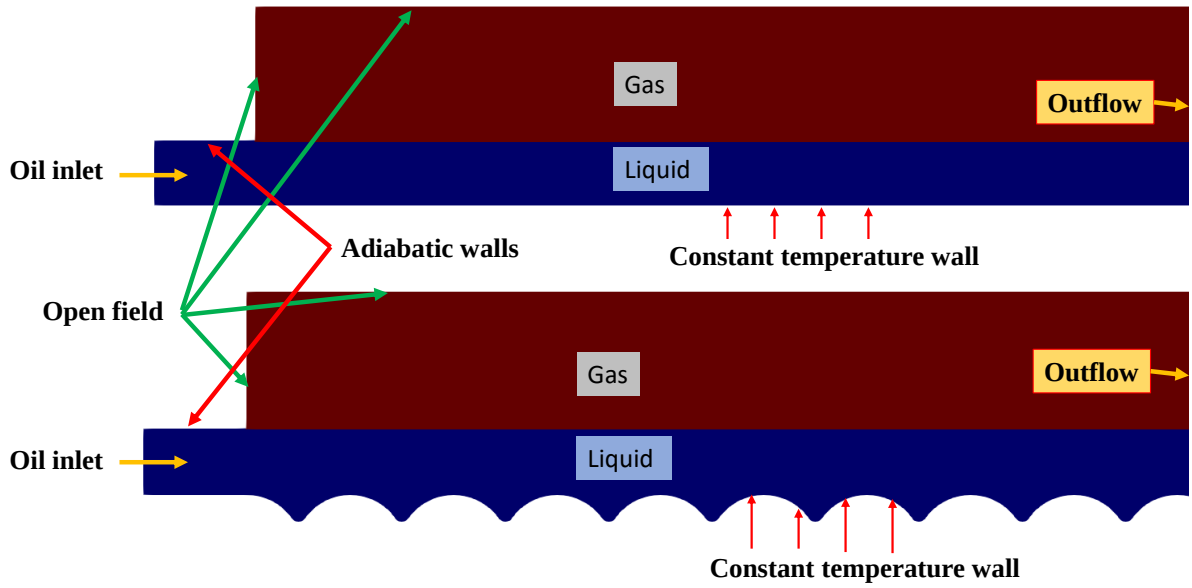

Figure 31. Schematic view of applied boundary conditions of the *flat and* corrugated channel

The boundary conditions for the fluid flow simulation are illustrated in Figure 31. The initial domain is pre-wetted by a liquid, while the rest of the domain is filled with air. The inlet velocity varies depending on the Reynolds number, but all the cases are still laminar flow, while the inlet temperature was set to 343 K. The outlet was subjected to a constant pressure boundary condition, while the top and side walls were set to open field. The walls of the inlet rectangle were set to no-slip adiabatic boundary conditions. Finally, the bottom wall was set to a constant temperature of 373 K.

For the properties of the liquid, the automatic transmission oil at 343 K listed in Table 2 was used, while the air properties were set to those of air at a pressure of 1 atm and a temperature of 300 K.

Table 2: Boundary conditions and liquid properties

$\boldsymbol{\rho_f}$	$\boldsymbol{c_{p,f}}$	$\boldsymbol{\mu_f}$	$\boldsymbol{k_f}$	$\boldsymbol{T_{hot\_wall}}$	$\boldsymbol{T_{input}}$	$\boldsymbol{Pr}$	$\boldsymbol{Re}$
803.6 $kg/m3$	$2247.28\,J/(kg*K)$	0.00770027 $N*s/m\text{^}2$	0.13 $N*s/m\text{^}2$	$373K$	$343K$	6.65-133.1 -	17-101.8 -

4.3.2 Mesh generation

In this section, a structured mesh used to simulate the bulk region of two different geometries. The mesh generation process for the flat and corrugated channel was described. Three different mesh (Mesh flat 1, Mesh flat 2, Mesh flat 3) and (Mesh corrugated 1, Mesh corrugated 2, Mesh corrugated 3) configurations were created and illustrated in Figure 32.

To avoid the adverse effects of irregular meshes on the wall and to improve the accuracy of heat flux calculations, the denser mesh was applied along the wall for flat channel and the inlaid mesh method (Figure 32) was employed for the heat wall boundary. The inlaid mesh method ensures that the distance from the center of the boundary cell to the wall is nearly constant and as heat flux depends on $T_{gradient}$, it can increase the reliability of heat flux calculation.

For the first mesh configuration, Mesh Flat 1, the base grid size was established at 12.5 μm. In the second configuration, Mesh Flat 2, the base grid size was halved and maintained at 6.25 μm. Finally, in Mesh Flat 3, the base grid size was kept constant, but the grid size at the wall was reduced by half to 3.125 μm.

In terms of the corrugated mesh configurations, Mesh Corrugated 1 had a base grid size and an inlaid mesh size both set at 12.5 μm. For Mesh Corrugated 2, the inlaid mesh size was held steady at 6.5

μm while the base grid size was halved. In Mesh Corrugated 3, the inlaid layer was further reduced to 3.125 μm.

Given the complexity of the mesh in the corrugated channel, it requires more meticulous examination. The corrugated mesh quality was first verified by the estimation of the thermal boundary layer and hydrodynamic boundary layer. As mentioned earlier, for laminar flow, the hydrodynamic layer for the open channel can be approximated as follow [76]:

$$\delta = \frac{4.92x}{\sqrt{Re_x}} \tag{72}$$

where x represents the distance from the origin in the x-direction and Re_x is the Reynolds number based on the characteristic length of x.

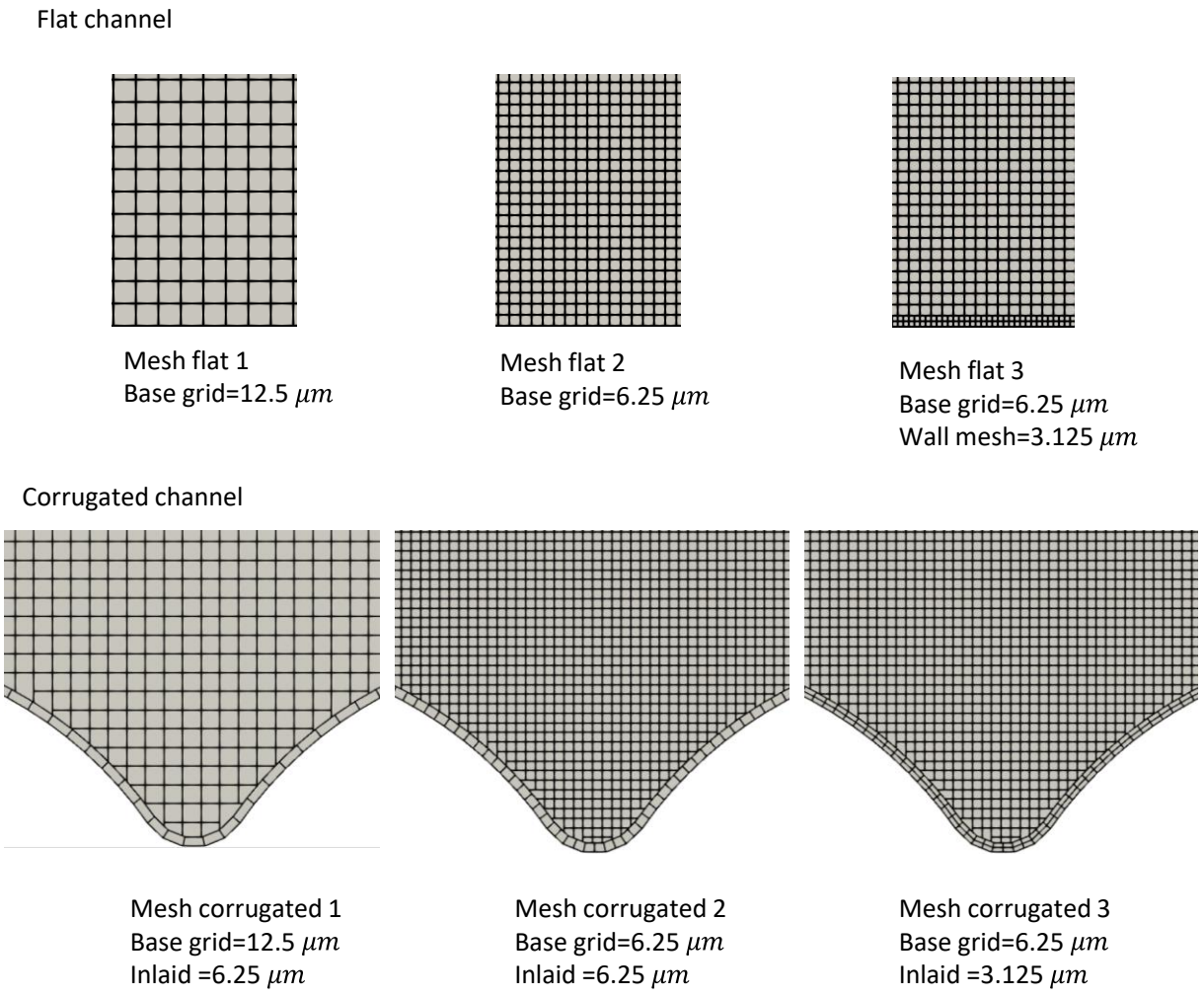

Figure 32. Three different mesh topologies for flat and corrugated channel

The thermal boundary layer δ_t is calculated based on the hydrodynamic boundary layer as:

$$\delta_t = \delta Pr^{-\frac{1}{3}} \tag{73}$$

Using these equations, one can estimate the number of mesh cells that fall within the thermal boundary layer thickness at different positions along the channel. The worst-case scenario is when the Reynolds and Prandtl numbers are at their highest values, which means that δ, δ_t are thinner and more mesh cells are needed to resolve them.

The given information states that in this worst-case scenario, 92% of the domain has a number of mesh cells inside δ_t higher than 24.64. This suggests that the mesh quality is adequate for resolving the thermal boundary layer and hydrodynamic boundary layer in the simulation.

Subsequently, the numerical results in Section 0 were studied to ensure that the mesh was of sufficient quality and density to accurately capture the flow and thermal features of interest.

4.3.3 Validation

In order to estimate accuracy, balance between the computational resource, the time convergence, grid independence, validation tests war carried out and are presented hereafter

(Figure 33). Therefore, a simulation time of 0.5 s was chosen as a fixed time for all other simulations.

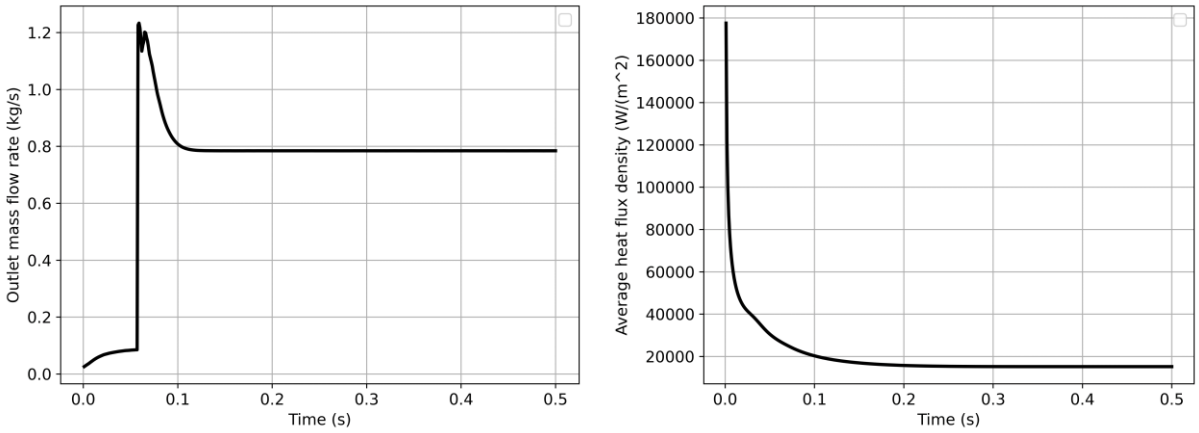

Figure 33. Time convergence study test of the corrugated channel (Mesh corrugated 3) at $Re = 101.8, Pr = 133$; a) Outlet mass flow rate; b) Average heat flux density

Time convergence study

To validate the simulation time, the simulation with the highest Reynolds and Prandtl number in Mesh corrugated 3 were selected because it represents the most challenging scenario for the simulation due to the thin thermal boundary layer.

The simulation achieved convergence at Time = 0.2 s for mass flow rate and 0.3 s for average heat flux density (Figure 33). However, the simulation was run until Time = 0.5 s to ensure strict convergence

Grid dependency tests and validation

Performing grid independence tests is crucial in terms of the reliability and accuracy of the outcomes derived from CFD simulations. The objective of these tests is to establish whether the solution produced by a CFD simulation remains unaffected by alterations in the resolution of the computational grid employed.

The mesh independence test outcomes for the corrugated channel at $Re = 101.8$ and $Pr = 133$ are exhibited in Figure 34 and Figure 35, for the three distinct meshes studied both flat and corrugated channel. The reason for selecting the highest Re and Pr within the test range of this study is due to the thinnest thermal boundary layer; if validated for this case, it should be considered valid for all other cases in the study. Figure 34 shows the average wall stress and average heat flux, while Figure 35 highlights the local changes, specifically wall stress magnitude and local heat flux, at positions $P = (24 - 26)$. (Wall stress is determined by multiplying the dynamic viscosity with the velocity gradient perpendicular to the wall. Heat flux is computed by multiplying the thermal conductivity with the temperature gradient at the wall.)

In reference to Figure 34, the flat channel exhibits minimal dependence on mesh of this size, indicating that increasing the mesh doesn't significantly affect convergence (as shown in Figure 11 a) and b)). In contrast, for the corrugated channel, the situation is noticeably different. The average wall stress demonstrated convergence between Mesh corrugated 2 and Mesh corrugated 3, with a minimal difference of 0.04%. Likewise, the average heat flux indicated convergence from Mesh corrugated 2 to Mesh corrugated 3, with a difference of 0.4% (the average is calculated along the heated wall; henceforth, any mention of ‘average’ refers to this calculation). These findings validate the mesh's appropriateness for calculating average wall stress and average heat flux values.

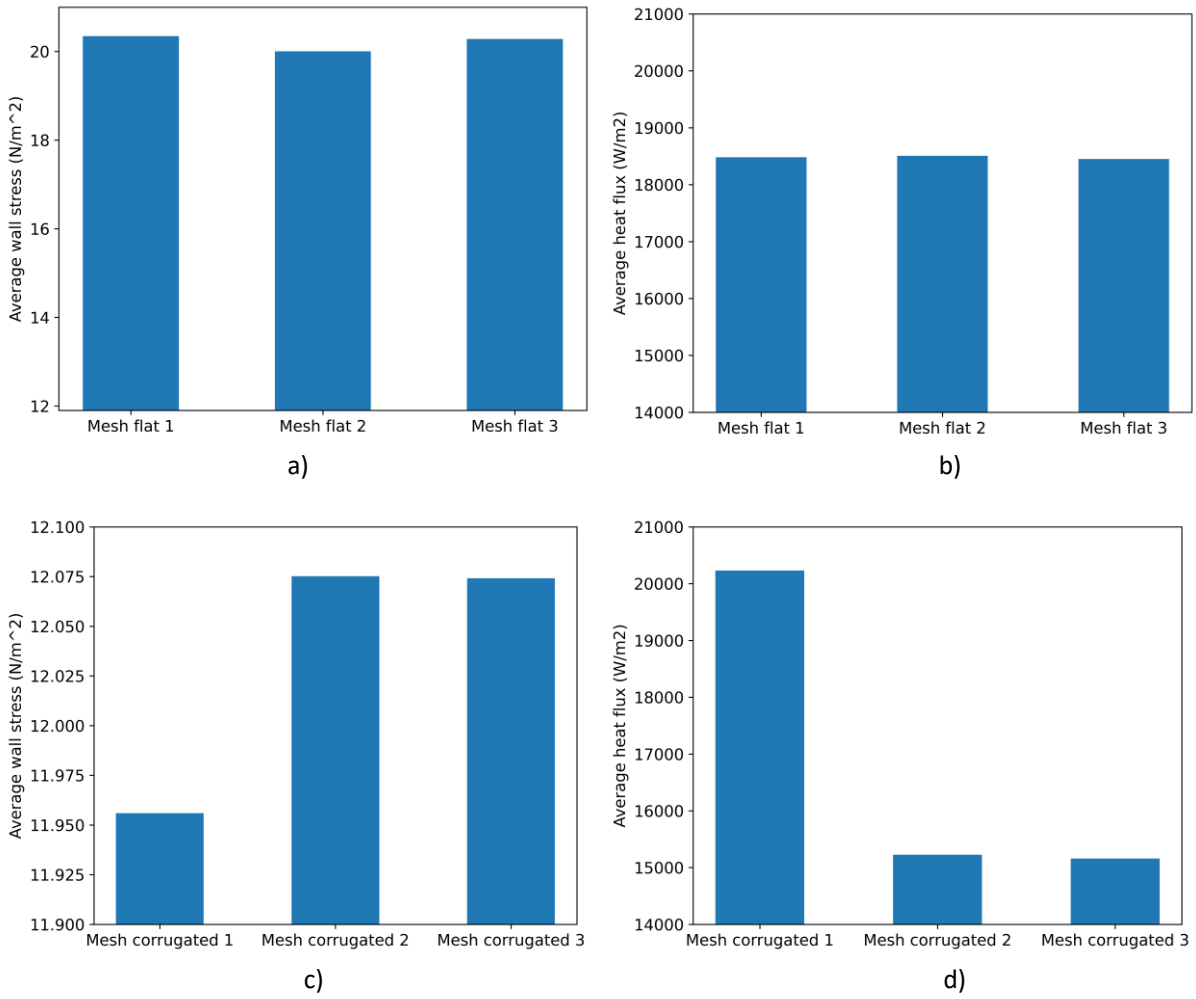

Figure 34. Mesh independence test of corrugated channel at $Re = 101.8, Pr = 133$; a) Average wall stress of flat channel; b) Average heat flux of flat channel; c) Average wall stress of corrugated channel; b) Average heat flux of corrugated surfaces

In Figure 35, the local impact of the mesh is emphasized at dimensionless positions $P = (24 - 26)$. Similarly, the flat channel achieves convergence effortlessly at this mesh scale. The local wall stress magnitude (Figure 35a) doesn't exhibit substantial dependency on the mesh configuration, although there's a minor deviation in the case of Mesh Corrugated 1. In contrast, the local heat flux (Figure 35b) displays considerable sensitivity to the mesh arrangement, especially at the coarse mesh of the corrugated channel. The local heat flux deviates notably from the outcomes observed between Mesh corrugated 1 and Mesh corrugated 2. Convergence of Mesh corrugated 2 and Mesh corrugated 3 is obtained.

Considering these findings, Mesh flat 3 and Mesh corrugated 3 has been chosen as the optimal mesh for all subsequent simulations, as it ensures sufficient convergence for both global and local variables.

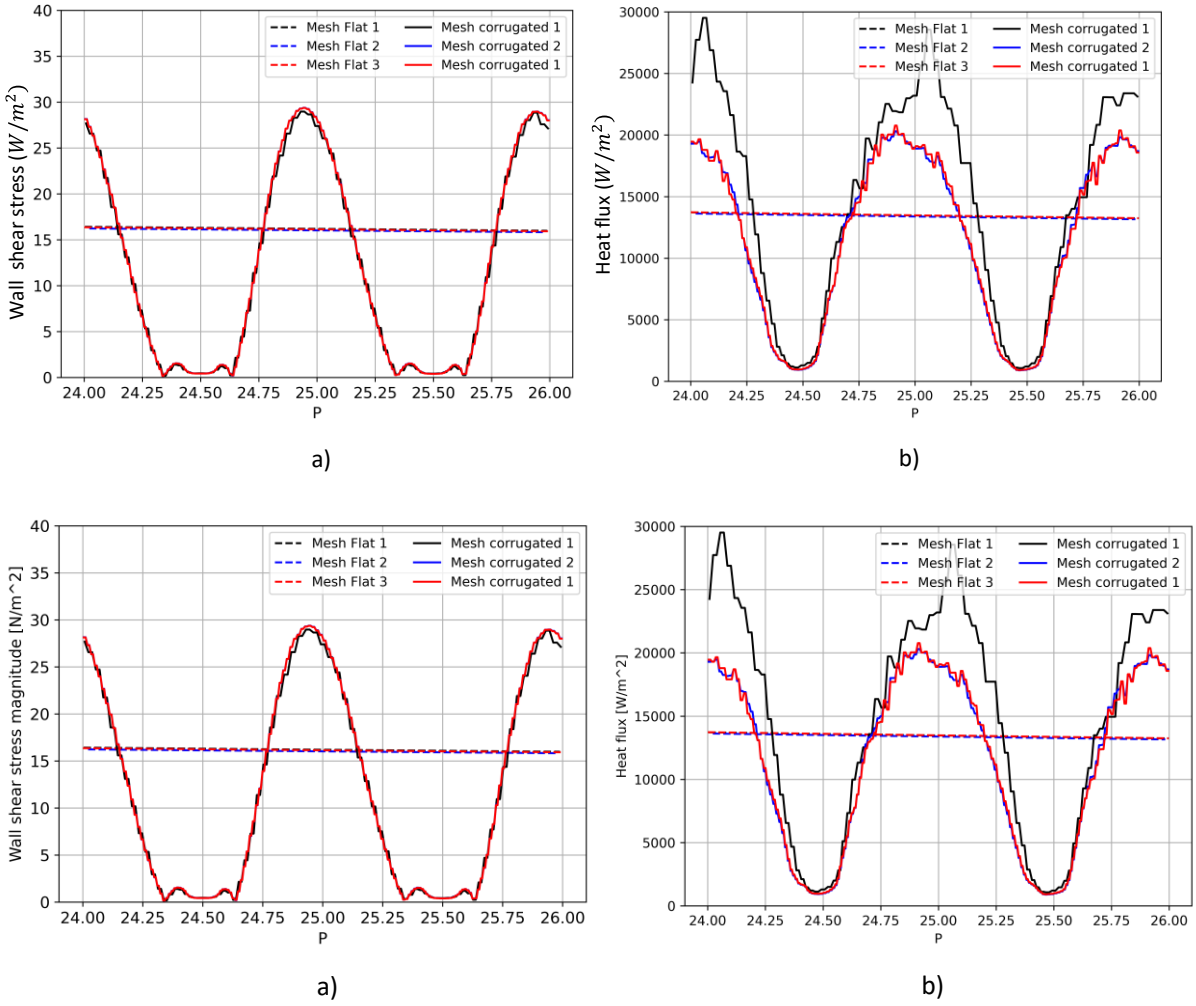

Figure 35. Mesh independence test of corrugated channel at $Re = 101.8, Pr = 133$ for local variables from $P = (24 - 26)$; a) Local wall stress magnitude; b) Local heat flux

Validating CFD results with Nusselt's theory was conducted by many researchers to check the accuracy of the employed numerical simulation. As mentioned earlier, Nusselt's theory provides an analytical solution for the laminar flow of a thin liquid film along a smooth plate, which can be used to predict the film thickness.

To validate numerical simulation, the film thickness is first calculated using Nusselt's theory for the laminar flow of a thin liquid film:

$$\delta_{film} = \left(\frac{3v_f^2 Re}{g}\right)^{\frac{1}{3}} \tag{74}$$

where δ_{film} is the film thickness, υ_f is the fluid kinematic viscosity, and g is the acceleration due to gravity.

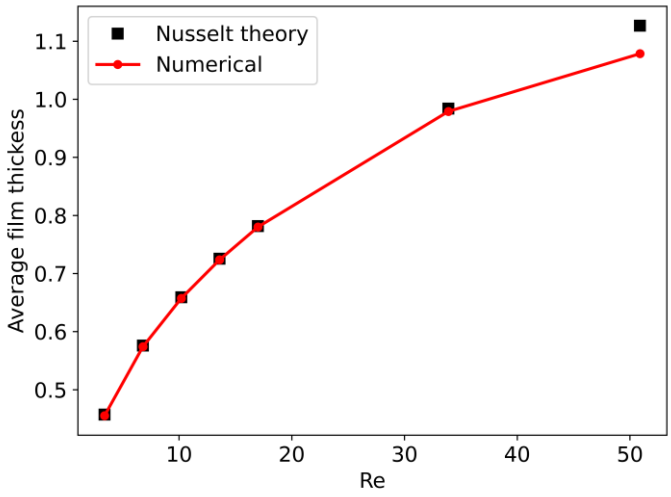

Figure 36. Film thickness of numerical simulation and Nusselt theory

The calculated film thickness is subsequently compared to the film thickness derived from the Computational Fluid Dynamics (CFD) simulations. Figure 9 illustrates the comparison between the film thickness predicted by Nusselt's theory and that obtained from the CFD simulations across various Reynolds numbers. As the film thickness develops throughout the channel, only the section from *P*=30 to *P*=50 is considered to retrieve the average film thickness value.

The results demonstrate that the numerical simulation outcomes align well with Nusselt's theory for low Reynolds numbers. However, as the Reynolds number increases, the discrepancies between the CFD simulation outcomes and Nusselt's theory become more pronounced. This can be attributed to the simplifying assumptions in Nusselt's theory, such as assuming uniform flow and disregarding the effects of waves and instabilities. Another possible reason is that the channel might not be long enough, causing the film to not fully develop at higher Reynolds numbers, which could result in larger errors for the average film thickness.

4.4 Influence of the geometry

4.4.1 Film flowing over a flat plate

To start with, let’s consider a fundamental study of fluid flow over a flat surface. The primary aim of this section is to develop a comprehensive understanding of the film flow dynamics along a flat plate. This fundamental knowledge will enable us and engineers to get essential fluid dynamics concepts

such as the evolution of the boundary layer and the heat transfer. This is a critical study that show the behavior of fluids near solid boundaries, the influence of viscous forces on flow patterns, and the associated heat transfer properties.

❖ Flow and heat transfer analysis

As presented in Section 4.3, the Nusselt theory is not very accurate when Reynold is higher than 20, due to instability of the interface. And to detail the film flow over a flat plate, a reference case at $Pr = 133$ is presented first.

This section aims to investigate the behavior of a liquid film flowing over a flat plate. Specifically, analyzing the thickness distribution, and thermal boundary layer. Figure 37 shows the evolution of film thickness, hydrodynamic boundary thickness and thermal boundary layer in a flat channel at $Re = 67.8$ and $Pr = 133$. The film thickness equals $0.65\ mm$ at $P = 0$, which is influenced by the inlet conditions. As the flow progresses, the film thickness gradually increases. The hydrodynamic boundary layer develops and extends towards the free interface at P around $5\ mm$.

On the other hand, the thermal boundary layer is thinner than the hydrodynamic boundary layer throughout the channel. This observation indicates that heat transfer primarily occurs within the liquid phase, and the effect of the interface between the liquid and the surrounding environment is negligible.

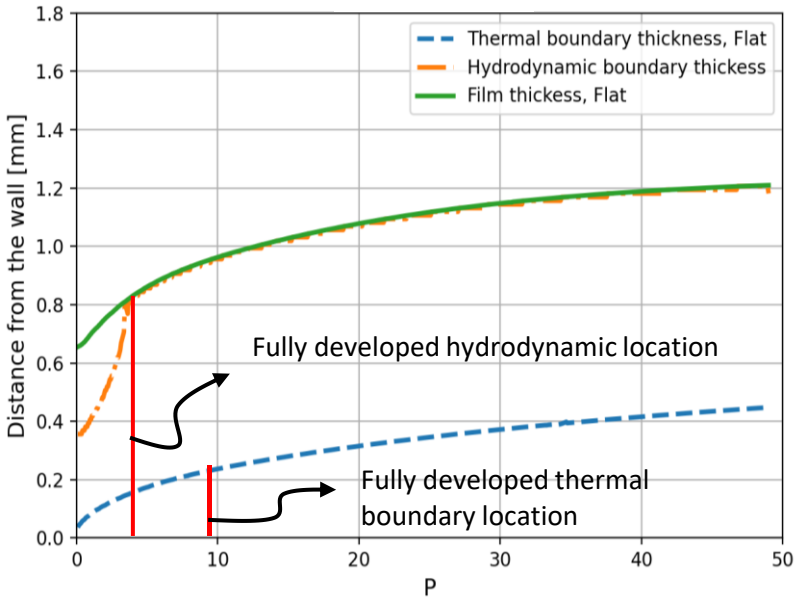

Figure 37. The evolution of film thickness, hydrodynamic boundary thickness and thermal boundary layer in a flat channel at Re=67.8 and Pr=133

Figure 38 shows the influent of Reynold's number on the average heat flux of flat chanel. As the Reynolds number increase, the average heat flux increase. The average heat flux gradually increases

from around 12500 [W/m^2] at Re =17 to around 17500 [W/m^2] at Re =101.8. It indicates in this test of Reynold range, when Re increases, the heat flux nearly linearly increases as well.

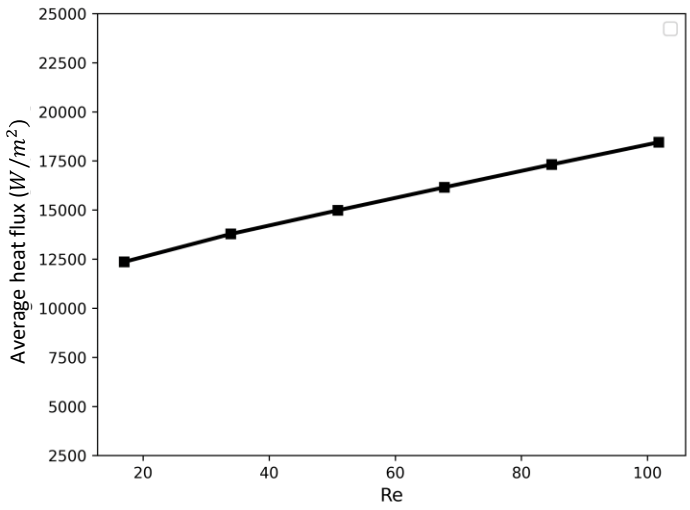

Figure 38. Average heat flux of flat channel

❖ Nusselt correlation for flat channel

The Nusselt correlation serves as a critical tool for quantifying convective heat transfer, streamlining complex heat transfer problems, and conserving time and resources. This proves particularly beneficial in scenarios involving a flat channel, such as when conducting experimental tests for the cooling of electric motors.

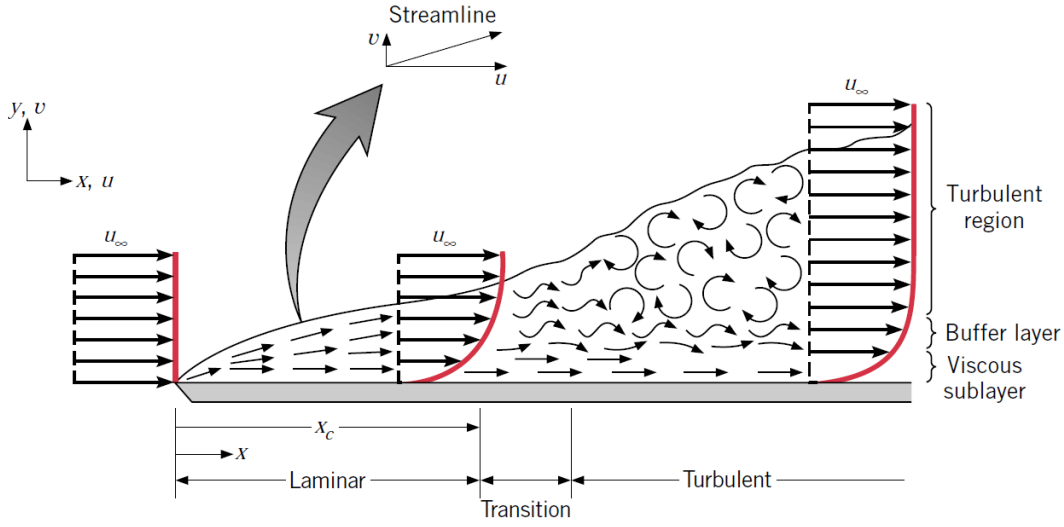

Figure 39. Velocity boundary layer development on a flat plate [77]

For open channel heat transfer single phase flow, Incropera and DeWitt [77] elaborate on the nondimensionalization of the boundary layer equations., introducing dimensionless numbers such as Reynolds, Prandtl, and Nusselt numbers to represent the local and average convection coefficients. These dimensionless numbers are used to provide a general form for the heat transfer problem, such as the function of the local Nusselt number depending on position, local Reynolds and Prandtl number:

$$Nu_x = f(x, Re_x, Pr) \tag{75}$$

And by using an analytical method, Incropera and DeWitt [77] introduce the local Nusselt number as:

$$Nu_x = 0.332 Re_x^{\frac{1}{2}} Pr^{\frac{1}{3}} \qquad Pr \geq 0.6 \tag{76}$$

Where Re_x instead depend on inlet diameter. In this case, it depends on the position in the x direction of the flat plate.

As shown in Figure 37, the thermal boundary layer, in this case, is thinner than the liquid interface and hydrodynamic boundary, which means that the heat transfer in this case only happens inside the liquid phase. Hence, by separating x in Equation 76, the new equation is as follows:

$$Nu_x = a x^b Re^c Pr^{\frac{1}{3}} \tag{77}$$

where

$$Re = \frac{d \rho_f u_f}{\mu_f} \tag{78}$$

Here is the step-by-step procedure:

Step 1: Local Nusselt number are calculated based on numerical results as reference:

$$Nu_x = \frac{hx}{k_f} \tag{79}$$

Step 2: From the numerical data of Nu_x, Re and Pr, the a,b,c parameters can be generated based on Equation (77). In this step, the a,b and c were calculated by linear regression method. The new Nu_x correlation estimated based on the data from numerical results as a=1.728, b=0.6, c=0.159:

$$Nu_x = 1.728x^{0.6}Re^{0.159}Pr^{\frac{1}{3}} \tag{80}$$

Step 3: Error Verification.

Once the parameters have been generated, it is crucial to validate their fit with the numerical data. Figure 40 illustrates the discrepancy between the Nusselt numbers computed by the new correlation and the numerical results. It indicated that the Nusselt calculated by Equation (80) shows good agreement with numerical results. To quantitatively estimate the error between these data, error chart needs to be delivered. Figure 41 shows the error of Nu correlation compared with numerical results. The results suggest that the overall error is less than 10%, with the most significant deviation found around the initial region. This area likely corresponds to the location where the thermal boundary layer hasn't fully developed yet. This error check helps ensure the new correlation's accuracy and reliability.

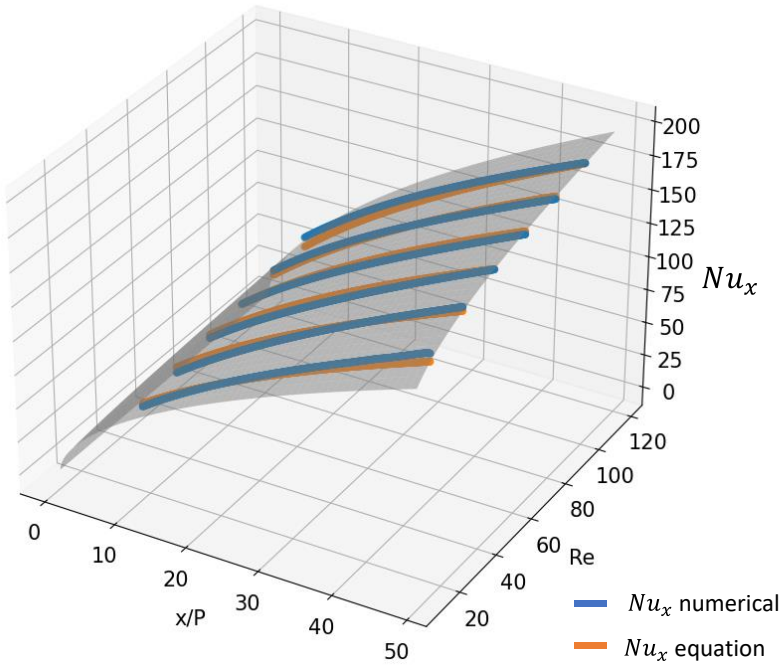

Figure 40. Comparison between the Nusselts calculated by new correlation and the numerical results

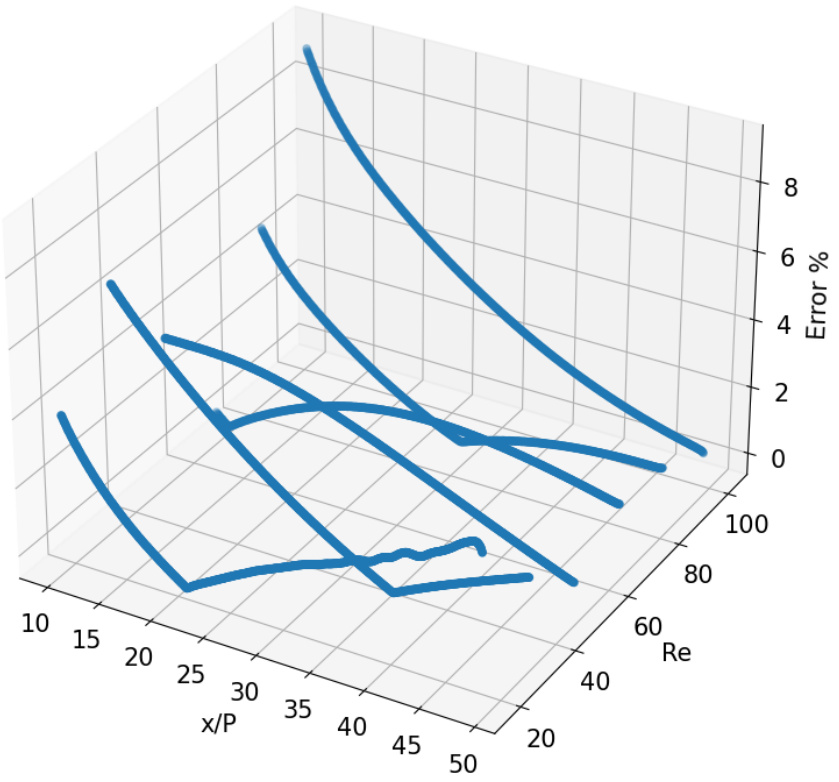

Figure 41. The error of Nu correlation compared with numerical results

4.4.2 Effect of corrugation

In this section, the case study $Re = 67.8$, $Pr = 133$ is the boundary condition for both flat and corrugated surface.

Figure 42 presents the velocity field with velocity direction represented by black arrows and iso-contours of temperature at 50% of the absolute temperature difference, $T_{hotwall} - (T_{hotwall} - T_{inlet}) * 0.5$ (white line), for both flat and corrugated surfaces in the range $P = 24 - 26$. Firstly, the velocity magnitude is zero at the wall and increases towards the core region for both flat and corrugated surface. However, the effect of corrugation on the velocity field is clearly observed, creating recirculation zones at the valleys of the corrugated channel, which is not present in the flat channel. In the flat channel, the velocity remains stable along the channel length, while in the corrugated channel, the velocity varies abruptly depending on the location. The flow accelerates at the peaks, as indicated by the thinner blue regions, whereas larger areas of low-velocity magnitude are observed in the valleys. This phenomenon significantly influences the shape of the iso-contours of temperature (white line). The iso-contours of temperature remain stable for the flat channel but become thinner at the peaks and expand dramatically at the valleys for the corrugated channel.

The corrugated channel's geometry creates recirculation zones and varying flow conditions, leading to a non-uniform thermal boundary layer. These observations demonstrate the significant impact of channel geometry on flow characteristics and heat transfer performance.

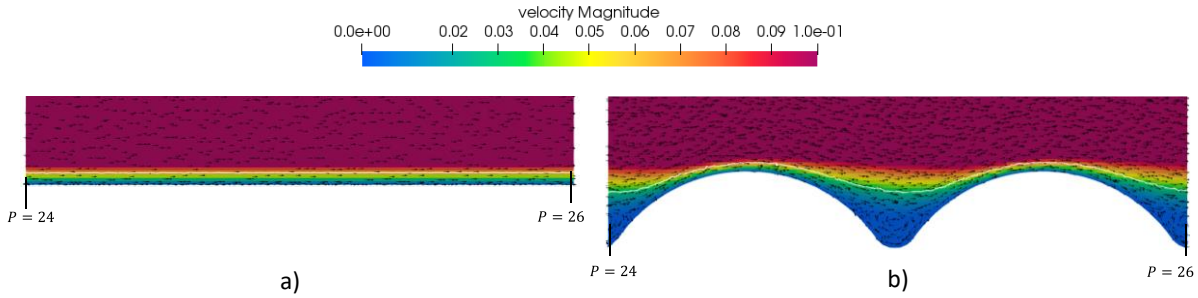

Figure 42. Velocity filed with velocity direction represented by black arrows and iso-contour of temperature at 50% of absolute different temperature (white line) at $Re = 67.8$, $Pr = 133$; a) flat; b) Corrugated

A quantitative analysis is presented in Figure 43, which displays the local wall shear stress magnitude and heat flux for flat and corrugated surfaces at $Re = 67.8, Pr = 133$ within the range $P = 24 - 26$. In the flat channel, the wall stress appears constant, while the heat flux gradually decreases over distance. In contrast, for the corrugated channel, both wall shear stress and heat flux are highly dependent on location due to the corrugation. For more details on the corrugated channel. Figure 43 a) illustrates that wall shear stress peaks earlier than the geometry, around $P = 24.9$. This suggests that the fluid exerts the strongest force on the side of the wall where the wall's normal vector opposes the main flow direction. At the channel's valley, the wall shear stress decreases significantly,. On the other hand, the local heat flux follows a similar trend, peaking at the same position as wall stress at over $14000\ W/m^2$ and reaching its lowest values in the area around the valley at $1000\ W/m^2$.

However, the average heat flux and wall stress values within this corrugated range are lower than those in the flat channel, suggesting that the corrugated channel's heat flux performance is less efficient than that of the flat channel. Such issue will be explored in Section 4.5.

In conclusion, the comparison of flat and corrugated surfaces at Re=67.8, Pr=133 reveals significant differences in flow characteristics and heat transfer performance. The corrugated channel's geometry induces recirculation zones and variable flow conditions, resulting in a non-uniform thermal boundary layer.

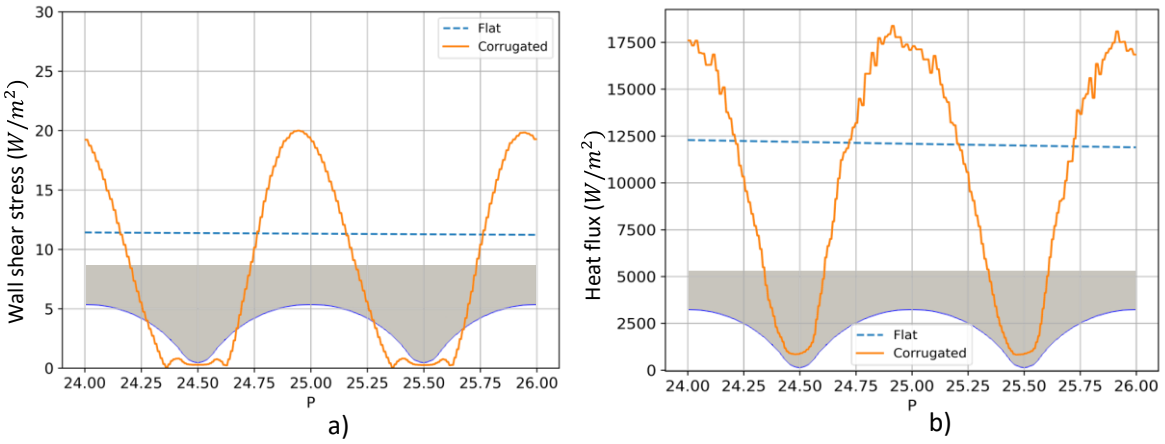

Figure 43. Local variables of flat and corrugated channel at $Re = 67.8$, $Pr = 133$ a) Wall shear stress magnitude; b) Heat flux

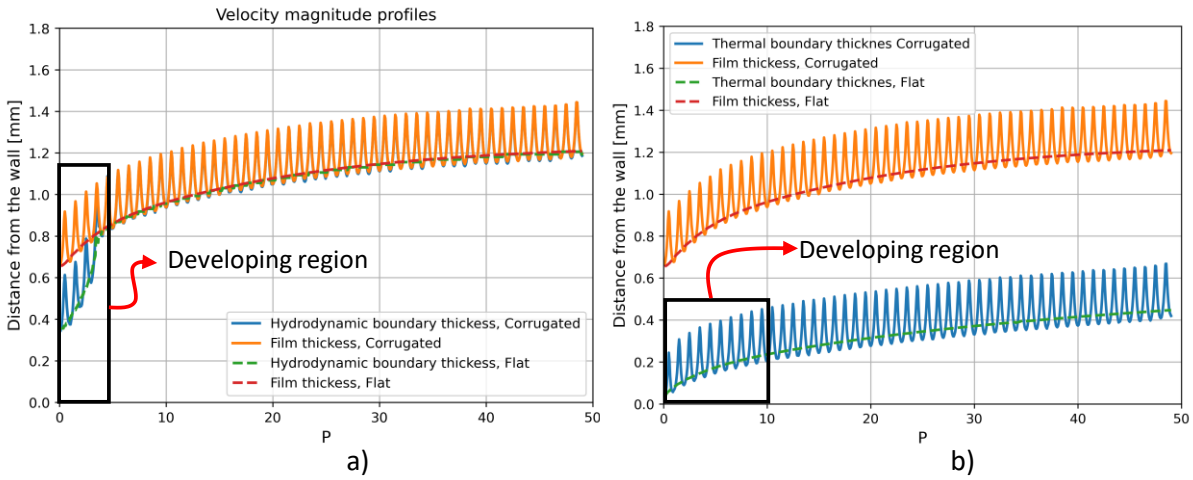

Figure 44. Thermal boundary layer, hydrodynamic boundary layer, and film thickness

To determine the hydrodynamic boundary layer thickness, different criteria are used for closed and open channel flows. In closed channels, the boundary layer edge is commonly defined as the point where the fluid velocity reaches 99% of the local average free-stream velocity. On the other hand, in open channel flows, the hydrodynamic boundary layer thickness is determined by analyzing the fluid velocity profile, with the maximum velocity used as a reference instead of the mean fluid velocity.

4.4.3 Effect of corrugation height ratio

In this section, the impact of varying geometries based on the ratio of bottom top height is compared to a reference case (1H). Three different geometries based on the ratio of the height of the bottom top,

namely 0.75H, 1H (reference case), and 1.5H are studied. Here, 'H' represents the ratio between the reference case and the other geometries.

In Figure 45 a), these three different cases corresponding to the three height ratios are illustrated. However, due to the modifications in the geometries, inlaid mesh is difficult to use. A cut-cell mesh strategy, which can easily mesh any type of wall pattern, has been adopted for the wall area as demonstrated in Figure 45 b). This strategy can handle complex geometries more effectively than a structured grid. In the bulk region, the mesh is kept identical across all cases.

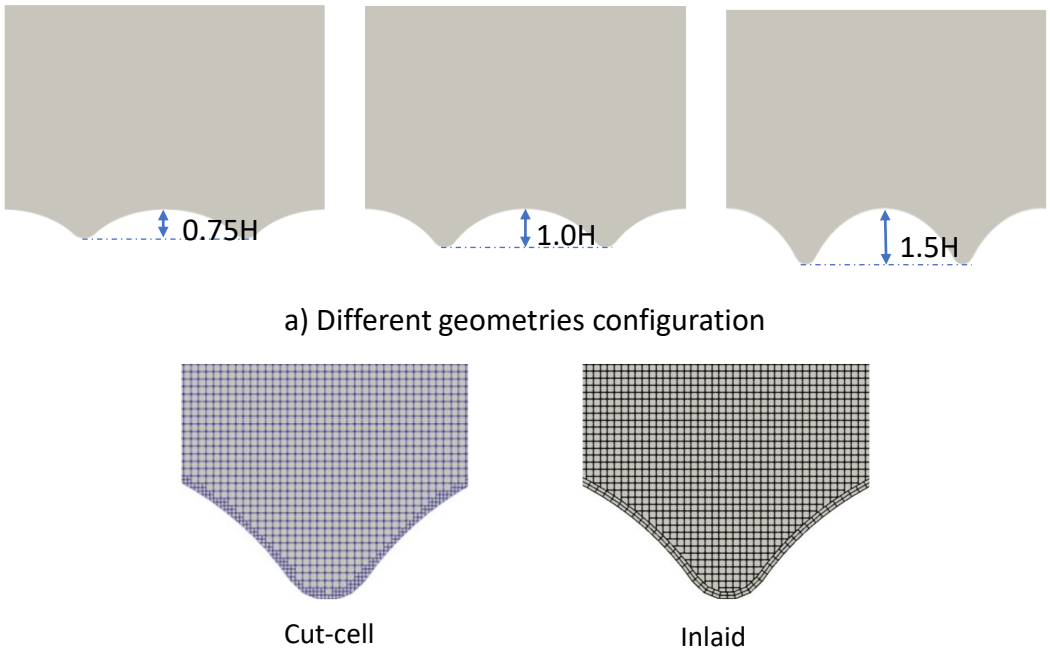

Figure 45. Geometries configuration and mesh strategy

To ensure that this change in mesh strategy does not significantly impact the results, a comparison of two mesh cases is provided in Figure 46. This comparison is carried out at a Re=101.8 and Pr= 133, which represent the highest Re and Pr in this studied. The purpose of this comparison is to validate the effectiveness of our revised meshing strategy, affirming that the overall and local results remain reliable and accurate despite the changes in meshing techniques. Figure 46 a) presents a comparison of the local heat flux distribution between the inlaid and cut-cell mesh strategies in the range P=24 to P=26. It can be observed that the cut-cell mesh exhibits good agreement with the inlaid mesh, particularly in the valley areas. However, some fluctuations occur, and stronger errors become apparent when the cut-cell strategy is applied to the wall in comparison to the structured inlaid mesh at the top area. In Figure 46 b), the average heat flux over time is presented. While the local heat flux

can exhibit fluctuations, the average heat flux is nearly identical for both the inlaid and cut-cell mesh strategies. Therefore, in order to simplify our analysis in this section, the cut-cell mesh strategy is applied in all forthcoming calculation.

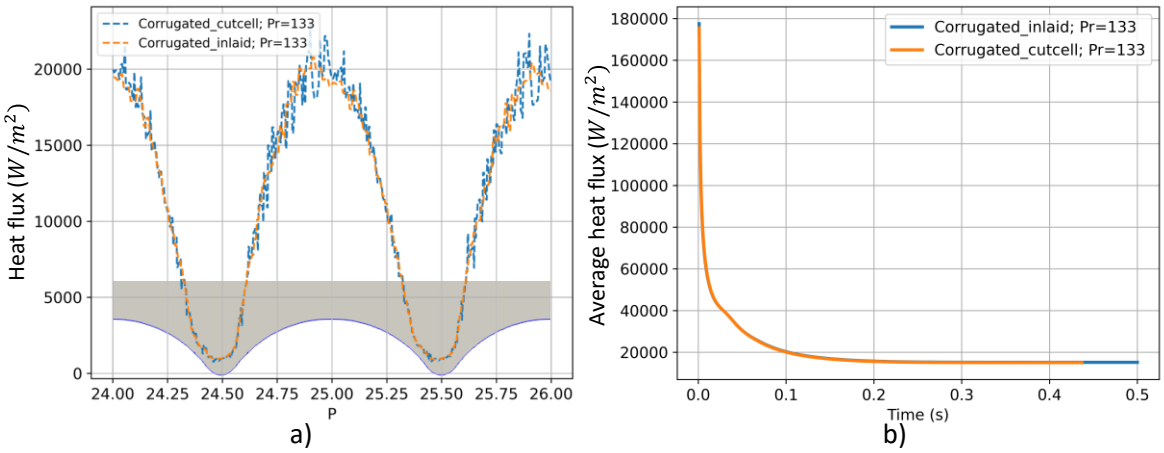

Figure 46. Comparative analysis of cut-cell and inlaid mesh strategies at Re=101.8 and Pr=133: a) local heat flux distribution; b) evolution of average heat flux along the channel

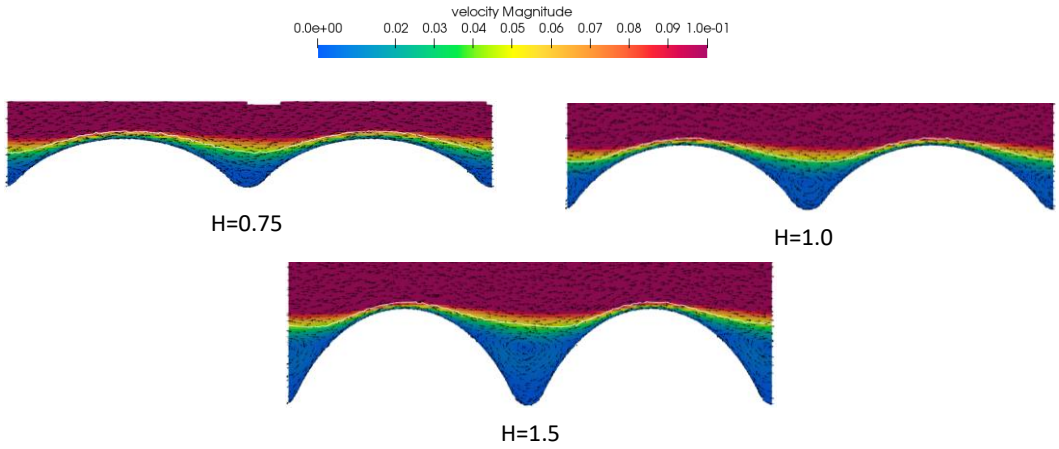

Figure 47. Velocity filed with velocity direction represent by black arrows and iso-contour of temperature at 50% of absolute different temperature $T_{wall} - (T_{wall} - T_{inlet}) * 0.5$ (white line) at $Re = 67.8, Pr = 133$

The velocity magnitude fields , thermal boundary layers, and velocity directions are visualized in Figure 47. Circulation can be observed at the valley of the channel. This circulation appears to move further away from the wall as the depth of the corrugation increases. This shift leads to the high-

temperature area becoming thicker as the depth of the corrugation increases, as indicated by the height of the isocountor (white line). Furthermore, the strength of the circulation appears to increase along with the depth of the corrugation.

To analyze the impact of Reynolds number on local heat flux of different geometries, the data for two distinct Re values: Re=17 and Re=101.8 has been presented. The subsequent data and figures will provide insights into how these different Reynolds number influence the local heat flux in different geometry configurations. Overall, the results clearly indicate that a higher Reynolds number leads to an increased heat flux Figure 48 a) and Figure 48 b). However, upon closer examination, there are an increase in the depth of corrugation results in higher heat flux at the top of the corrugation but significantly lower at the bottom.

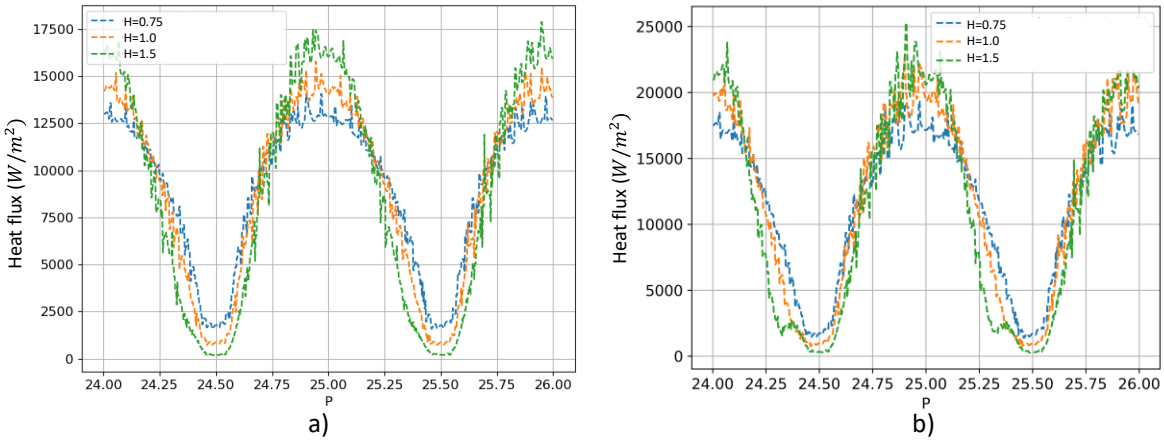

Figure 48. Local heat flux for different ratio at Pr=133; a) Re=17; b) Re=101.8

Therefore, an evaluation of the average heat flux is necessary to understand the overall impact of the depth of corrugation. Figure 49 displays the average heat flux for three different corrugation geometries, as well as for a flat channel. Interestingly, the average heat flux of the flat channel is the highest and decreases as the depth of corrugation increases for all tested Reynolds numbers. This finding provides a counter-intuitive insight into the interplay between geometric factors and heat flux in fluid dynamics.

In this section, the influence of varying corrugation height ratios (0.75H, 1H, and 1.5H has been analyzed. The depth of the corrugation was found to have notable effects on the flow and heat transfer characteristics. Circulation in the valley of the channel became stronger and moved further away from the wall as the depth of the corrugation increased. The average heat flux of the flat channel was found to be the highest and it decreases as the depth of corrugation increased for all tested Reynolds numbers.

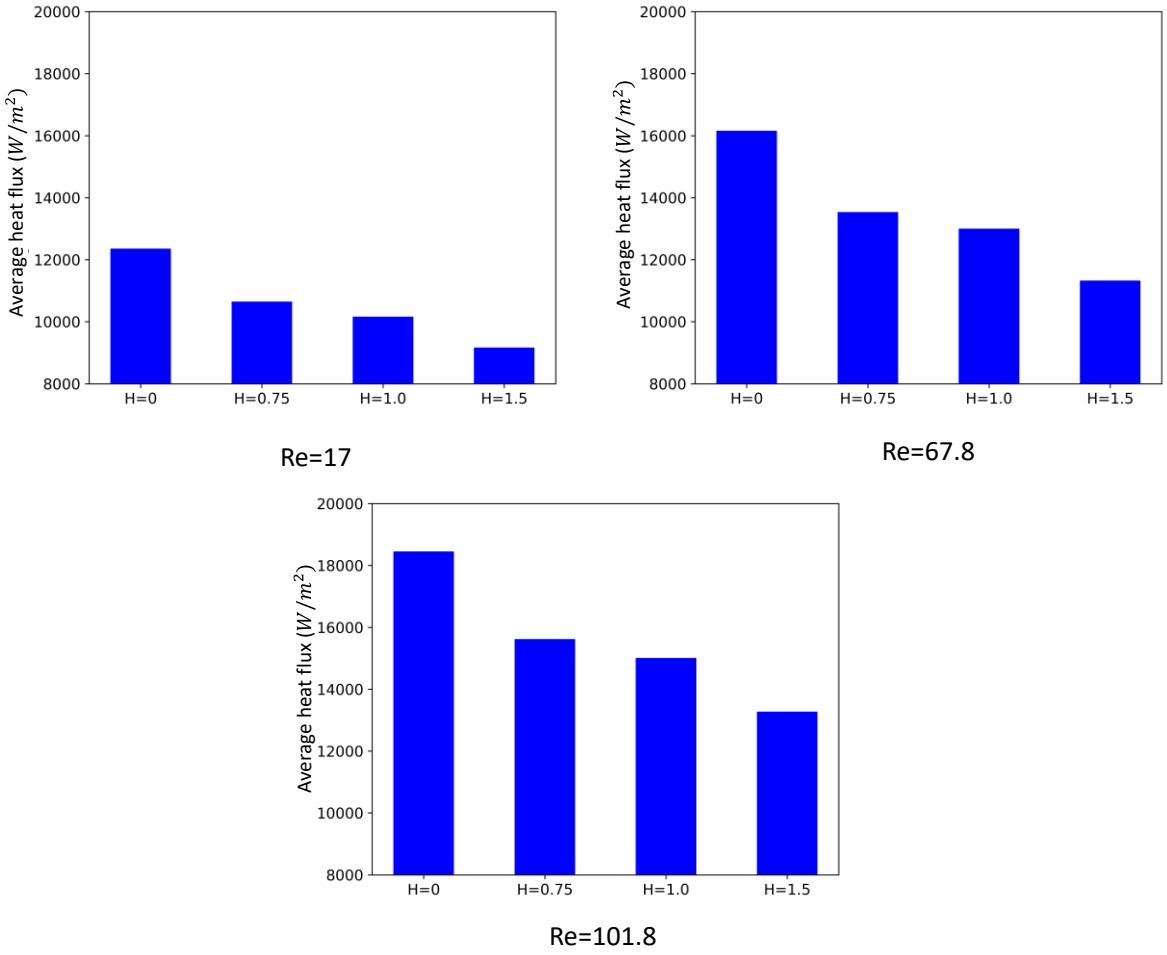

Figure 49. Average heat flux comparison at 3 different Re for 3 different geometries and flat channel (H=0)

4.5 Influent of fluid properties

4.5.1 Effect of Prandtl number on heat transfer

In this section, the influence of the Prandtl number on heat transfer in both flat and corrugated surfaces at three different Reynolds numbers (17, 67.8, and 101.8) are analyzed, noting that the flow regime is laminar. The results, illustrated in Figure 50, depict the average heat flux as a function of the Prandtl number for each channel configuration and Reynolds number.

Upon examining the data, it becomes apparent that the average heat flux in the corrugated channel is consistently lower than that in the flat channel. This difference in heat flux becomes more pronounced as the Prandtl number increases. For instance, at $Re = 17$ and $Pr = 6.65$, the difference in average heat flux between the flat and corrugated surfaces is approximately 100 W/m^2. However, when the

Prandtl number increases to 133 at the same Reynolds number (Re=17), the difference in average heat flux between the two channels rises to around 250 W/m^2.

This observation suggests that the heat transfer performance in corrugated surfaces is not only dependent on the channel geometry and Reynolds number but is also significantly influenced by the Prandtl number.

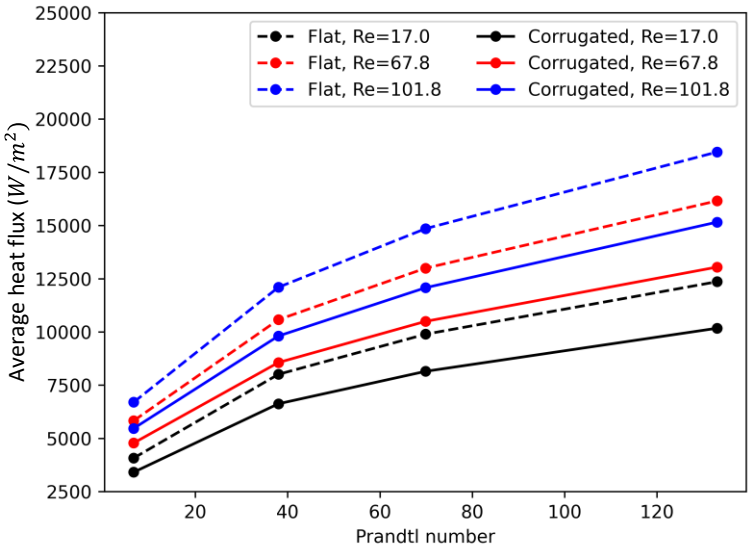

Figure 50. Average heat flux versus Prandtl number of the flat and corrugated channel at 3 different Reynolds number

Further investigation into the local regions of the channel is required to better understand the underlying mechanisms responsible for these variations in heat transfer performance. Figure 51 reveals the local heat transfer at $Re = 67.8$ for different Prandtl numbers, illustrating the local heat flux effect influenced by the Prandtl number. As indicated in section 4.4, the magnitude of heat flux strongly depends on location for corrugated surfaces, whereas this is not the case for flat channels. Figure 51 also reveals that when the Prandtl number increases, both corrugated and flat channels require more heat flux compared to lower Prandtl numbers. However, in corrugated surfaces, when the Prandtl number increases, only the sections with high altitude require more heat flux, while in the valleys, the heat flux appears to remain constant.

This observation implies that the heat transfer performance in corrugated surfaces is more complex than in flat channels, with the channel geometry, Reynolds number, and Prandtl number all playing significant roles. The local variations in heat transfer performance in corrugated surfaces may be attributed to factors such as flow separation, vortex formation, and enhanced mixing caused by the

corrugated geometry. Further research is needed to better understand these effects and optimize heat transfer performance in corrugated surfaces for various flow conditions and fluid properties.

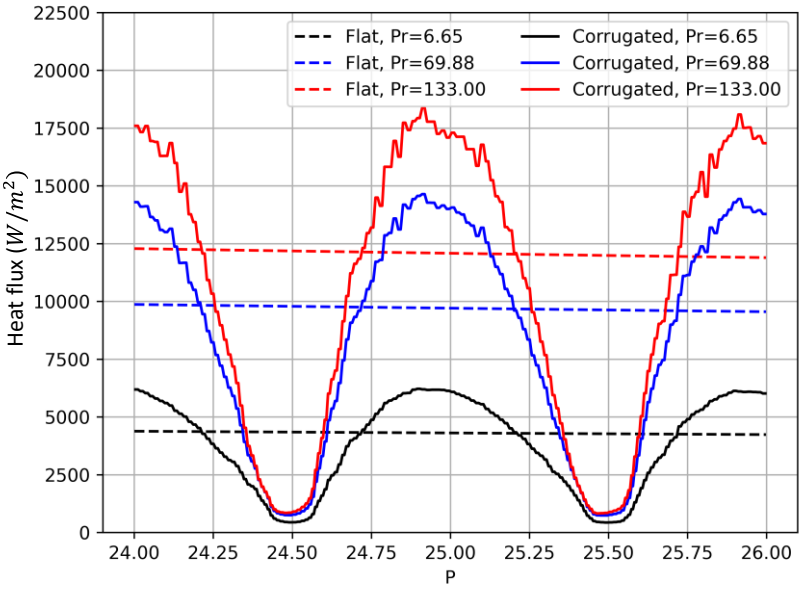

Figure 51. Local heat flux of flat and corrugated channel at $Re = 67.8$

For a more in-depth exploration of local hydrodynamics and heat transfer phenomena, it is necessary to evaluate the temperature and velocity profiles. Figure 52 presents the velocity profile for Prandtl numbers of 6.65 and 133. At a P of 25, the velocity profile in the flat channel is fully developed and does not change significantly. However, the situation in the corrugated channel is entirely different. At P=25, the velocity magnitude in the corrugated channel surpasses that of the flat channel due to the influence of corrugation. This effect is particularly noticeable at distances from 0.16 to 0.6 from the wall.

Conversely, at the valleys (P=24.5 and P=25.5), the velocity magnitude is virtually zero when the distance from the wall is less than 0.1 mm. This condition suggests these regions are less effective for heat transfer compared to others. The variations in the velocity profile in the corrugated channel significantly influence the heat transfer characteristics in these regions.

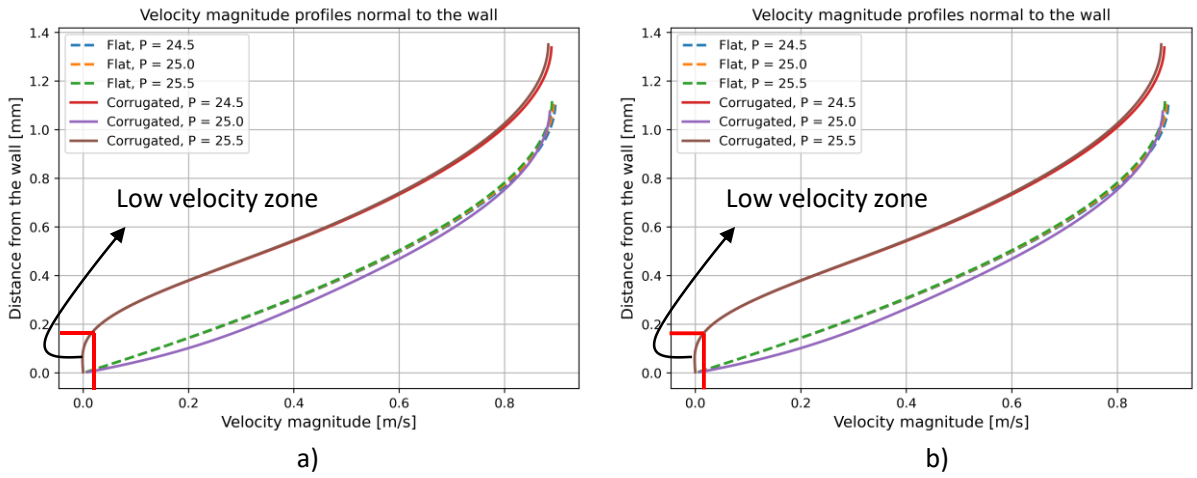

Figure 52. Velocity profile at Re=67.8; a) Pr=6.65; b) Pr=133

Figure 53 displays the temperature profile at both low and high Prandtl numbers. In the case of the flat channel, the thermal boundary layer is completely developed, with a thickness of less than 1mm at Pr=6.65 and less than 0.4 at Pr=133. On the contrary, the temperature profile undergoes a dramatic shift in the corrugated channel. At P=25, the temperature is less steep compared to the flat channel, indicating that heat transfer is more efficient here. However, at P=24.5 and P=25.5, the temperature profile of the corrugated channel near the wall is steeper than the flat channel, suggesting that the temperature gradient in this area is smaller. Consequently, this leads to a decrease in heat flux, which is also suggested in Figure 51. These distinct variations underline the considerable impact that the channel's structural characteristics exert on heat transfer properties.

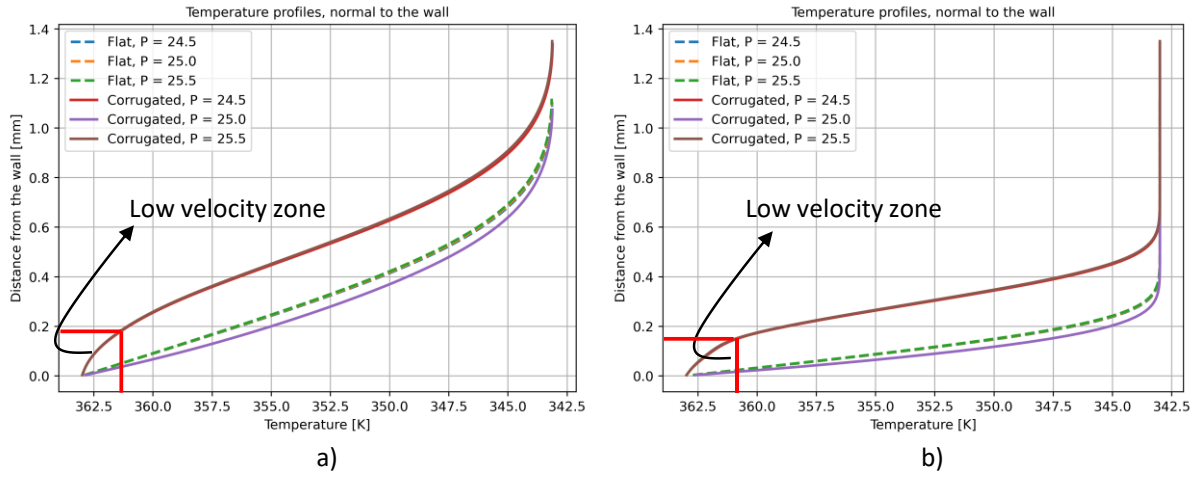

Figure 53. Temperature profile at Re=67.8; a) Pr=6.65; b) Pr=133

4.5.2 Effect of Reynolds number on heat transfer

This section focus on a detailed analysis of the Reynolds number's effect. Initially, the relationship between the average heat flux and the Reynolds number (Figure 54) is examined. As observed in the previous section, a similar trend emerges, indicating that the average heat flux is lower in corrugated surfaces within a Reynolds range of 17 to 101.8 and a Prandtl range of 6.65 to 133. The absolute difference between the flat and corrugated surfaces increases with an increase in the Prandtl number. Similarly, as the Reynolds number increases, the difference in average heat flux between the flat and corrugated surfaces also increases, providing a more detailed explanation of this phenomenon, showing local heat flux at Pr=133 and three different Reynolds numbers, namely 17, 67.8, and 101.8.

The detail of this phenomenon can be explained in Figure 55, where local heat flux at $Pr = 133$ and 3 different Reynolds 17, 67.8 and 101.8 are revealed. The figure compares the heat flux in both corrugated and flat channels. As the Reynolds number increases, the heat flux in both types of channels also increases. For instance, at P= 25, the heat flux in the flat channel increases from 8000 W/m² to 11000 W/m² as the Reynolds number increases from 17 to 101.8. Similarly, for the corrugated channel, the heat flux increases from 11500 W/m² to 15500 W/m² with the same increase in Reynolds number. However, an interesting phenomenon is observed at the valleys (P= 24.5 and P= 25.5), where the heat flux does not increase even when the Reynolds number is increased. This can be attributed to the structure of the wall in these areas, which causes circulation to occur, trapping hot fluid inside. Consequently, heat transfer to the bulk area becomes difficult, resulting in no change in the heat flux in these regions.

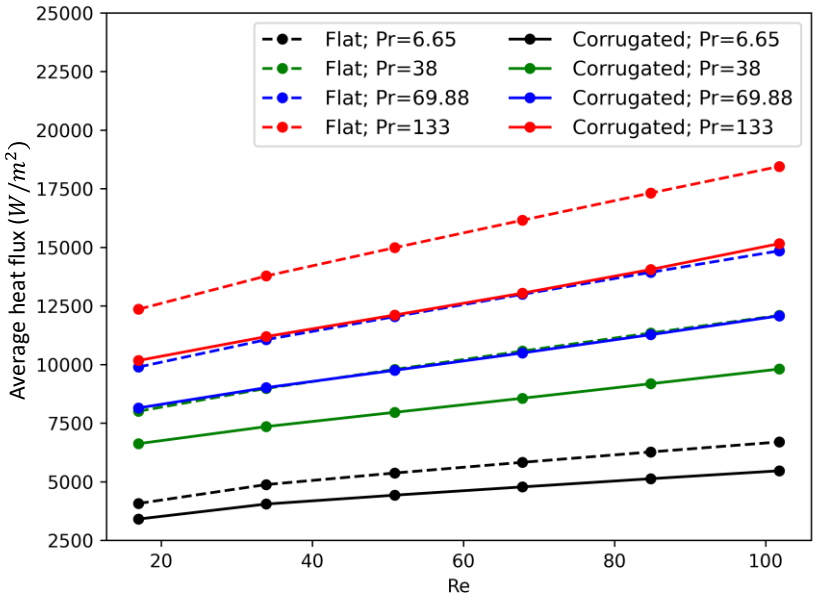

Figure 54. Average heat flux versus Reynolds number of flat and corrugated channel for different Prandtl number

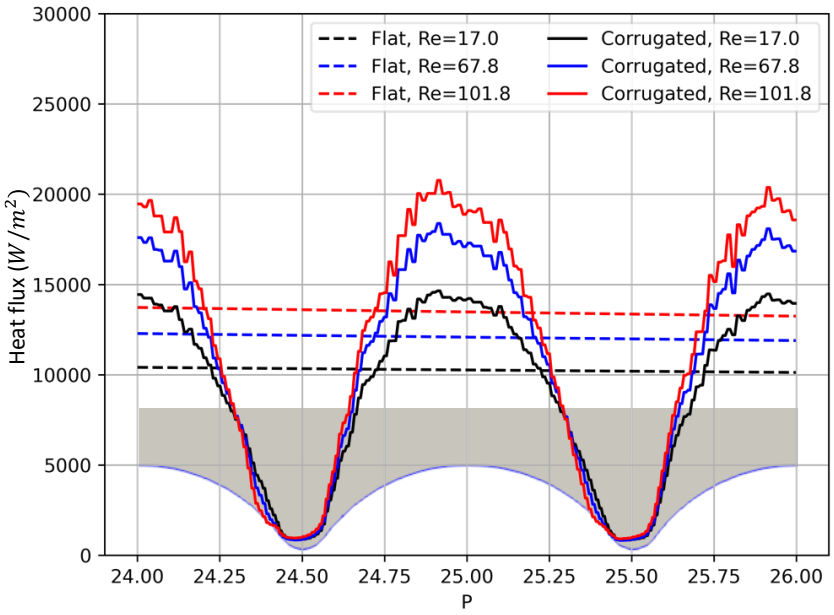

Figure 55. Local heat flux of flat and corrugated channel at $Pr = 133$

Figure 56 illustrates two distinct velocity profiles at Re=17 and Re=101.8. For both cases, the velocity in the flat channel doesn't change significantly. However, the situation in the corrugated channel is entirely different. The velocity profile is highly dependent on location. At P=25, the velocity magnitude of the corrugated channel exceeds that of the flat channel. In contrast, at P=24.5 and P=25.5, the velocity magnitude is considerably lower than in the flat channel. These differences highlight the significant role of channel geometry in influencing the velocity profiles, which in turn impacts heat transfer characteristics. Interestingly, regardless of whether the Reynolds number is low or high, there is not a significant difference in the velocity.

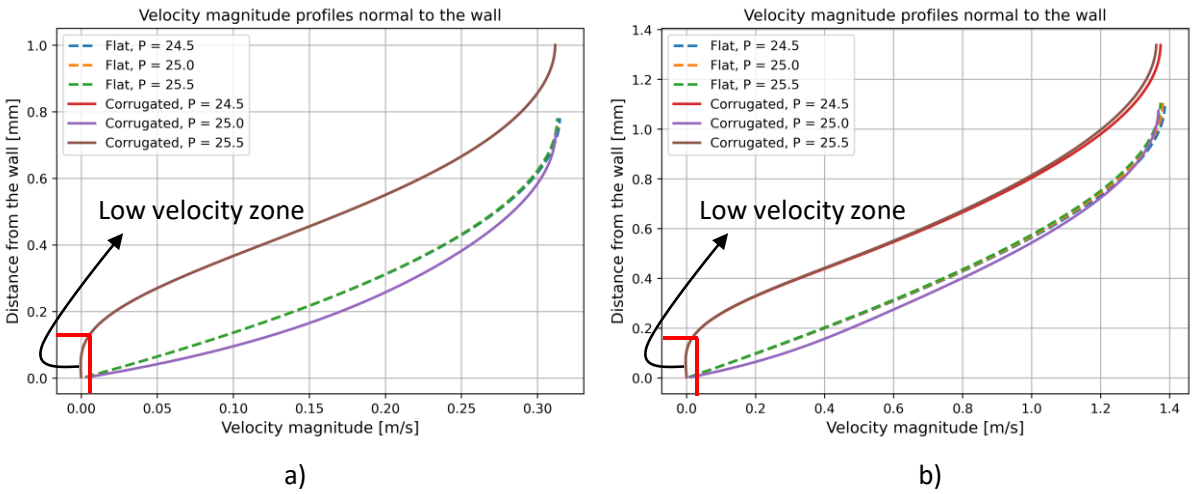

Figure 56. Velocity profile at Pr=133; a) Re=17, b) Re=101.8

Figure 57 presents the temperature profile at Pr=133 with two different Reynolds numbers, 17 and 101.8. Similar to the earlier observation, the temperature profile exhibits a consistent trend, with a steeper profile at low Reynolds numbers and a flatter one at higher Reynolds numbers. Specifically, at a P=25, the temperature within the corrugated channel decreases more rapidly compared to the flat channel, leading to a higher heat flux in this area. However, at P= 24.5 and 25.5, the presence of a low-velocity zone hampers effective heat transfer, resulting in a reduced temperature gradient in this region and, consequently, a lower heat flux.

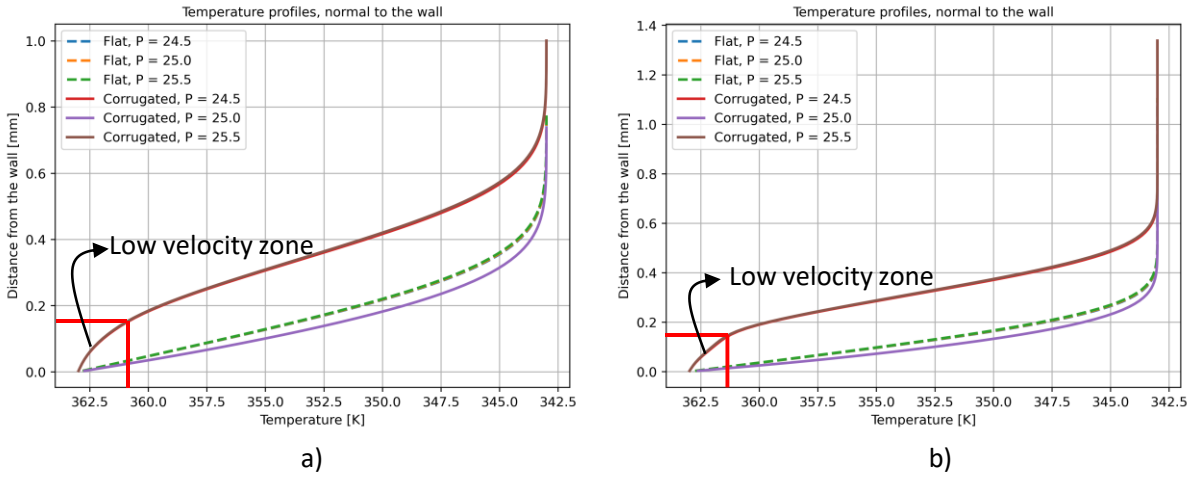

Figure 57. Temperature profile at Pr=133; a) Re=17, b) Re=101.8

4.6 Conclusions

Based on the knowledge gain in the previous section, in this section, hydrodynamics and heat transfer of film flow within corrugated surfaces for Reynolds numbers less than 101.8 and Prandtl numbers less than 133 were examined using VOF method. The primary objective was to gain a deeper understanding of the interactions occurring among flow behavior, surface geometry, heat transfer and fluid properties in such configurations. The influence of channel geometry on flow behavior and heat transfer characteristics has been studied. A flat channel was used as the reference model, providing detailed insights into heat transfer mechanisms, flow behavior patterns, and enabling the application of Nusselt correlations for comparative purposes. A thorough analysis was performed to discern the differences between flat and corrugated surfaces, revealing notable disparities in flow characteristics and heat transfer performance. The corrugated channel's geometry was found to induce recirculation zones and create variable flow conditions, leading to a non-uniform thermal boundary layer. While these features may initially seem advantageous, the average heat flux and wall stress values within the studied range of corrugations were found to be lower 10 to 30% than those observed in flat channels. This result suggests that the heat transfer performance of corrugated surfaces is less effective than that of their flat counterparts.

This study represents an initial effort to comprehend the hydrodynamic phenomena of liquid flow across complex surfaces, as well as their heat transfer properties. The findings from this research are important in the development and implementation of a new thermal wall law (as part of another PhD project in our department) suitable for low Reynolds and high Prandtl flows on both smooth and detailed surfaces.

Chapter 5

Numerical method for moving contact line flow

The detailed presentation of a newly developed method to accurately capture wetting phenomena is provided. This includes the mathematical equations and the specifics of how they are implemented into the CFD software.

5.1 Background

In Chapter 3, a detailed discussion on two-phase flow methodologies is presented, emphasizing the continuum surface force (CSF) method. This method, which employs a smooth void fraction (SVF) approach, is widely used in commercial Computational Fluid Dynamics (CFD) applications, including CONVERGE CFD [78]. The CSF method has been extensively used to model surface tension across various fixed mesh formulations for interfacial flows. This is particularly seen in volume-of-fluid (VOF) [79], level-set (LS) [80], and front tracking (FT) [81] interface representation techniques.

In the CFS methodology, surface tension forces acting on the interface are transformed into volume forces in regions near the interface via delta functions of void fraction. This transformation results in discontinuous interfacial jump conditions which is suitable for multiphase flow simulations. However, a critical issue with the SVF method is the generation of unphysical flows, often referred to as "spurious currents". These currents become particularly problematic when dealing with contact angles, where capillary forces dominate the inertial forces. Spurious currents are notably highlighted in the case of an inviscid static drop in equilibrium without gravity, where Laplace's formula applies [82,83]. These currents mainly originate from a numerical imbalance between the surface tension force and the associated pressure gradient and from an inaccurate estimate of the curvature.

Numerous studies have proposed various solutions to reduce these spurious currents. These methods range from improving curvature estimation [41], enhancing the flow algorithm [84], or combining superior algorithms with better interface curvatures estimation [85]. Francois et al. [85] have successfully eliminated these spurious currents by using well-balanced and height function method. However, this achievement is currently limited to a projection correction method.

In this chapter, a balanced-force algorithm designed specifically for the Pressure-Implicit with Splitting of Operators (PISO) algorithm is introduced. This algorithm is characterized by a unique pressure-correction method, which ensures an exact balance between the pressure gradient and the surface tension force, thereby significantly reducing the occurrence of spurious currents.

We also provide the implementation of the contact angle model for both the Smoothed Void Fraction (SVF) and height function methods. Our work aims to illuminate the inner workings of these complex

calculations, and their impacts on the performance and results of CFD analyses will be provided in the Chapter 6.

5.2 Well-balanced PISO algorithm for two-phase flow

It is not easy to design a numerical scheme to solve partial differential equations that can ensure the specific equilibrium of the continuous equations when it is discretized numerically, in particular when developing the numerical method to solve two-phase flow.

This section will present in detail the Well-balanced PISO algorithm that implemented in the Converge code. It is developed to ensure that the surface tension force is exactly balanced with the pressure gradient force.

To ensure the balanced force, the discrete approximations of both pressure gradient and surface tension need to be discretized at the same time and at the same place. As a consequence, the PISO loop is changed accordingly.

First, the discretized first-order momentum equation at the predictor step Equation (66) has to be modified and can be re-written as [46,85]:

$$\rho_c^n u_c^* = \rho_c^n u_c^n + H^* - \Delta t \rho_c^n \left\langle \frac{\nabla P}{\rho_f} - \frac{F_f}{\rho_f} \right\rangle_{f\to c}^{n} \tag{81}$$

The pressure term and surface tension term are interpolated from face to cell-center in Equation (81) as detailed below for x direction only:

$$\begin{aligned} \left\langle \frac{\nabla P}{\rho_f} - \frac{F_f}{\rho_f} \right\rangle_{f\to c}^{n} = & \left(\frac{A_{i+1/2} n_{i+1/2}}{1/2 \rho_{i+1/2}} \left(\frac{P_{i+1} - P_i}{dx} - \frac{\sigma \kappa_{i+1/2} (\alpha_{i+1} - \alpha_i)}{dx} \right) \right. \\ & \left. + \frac{A_{i-1/2} n_{i-1/2}}{1/2 \rho_{i-1/2}} \left(\frac{P_i - P_{i-1}}{dx} - \frac{\sigma \kappa_{i-1/2} (\alpha_i - \alpha_{i-1})}{dx} \right) \right) \end{aligned} \tag{82}$$

Where $A_{i+1/2}$ and $n_{i+1/2}$ indicates the face area and the normal vector of the right face, respectively (Figure 58). To calculate this term in 3D, a loop on the three directions is required.

The Rhie and Chow Algorithm has originally been developed for single-phase flow. Hence there is a need to modify and adapt the Rhie and Chow Algorithm to two-phase flow by adding the surface tension force in Equation 67 in order to balance the pressure forces. The modified Rhie and Chow algorithm is written as:

Since Equation 67 is too long, the authors split the modified RHS terms in three parts. The first term does not change:

$$1st: \frac{u_i^* + u_{i+1}^*}{2} \tag{83}$$

The second and third terms are modified as:

$$2nd: \frac{dt}{\left(\rho_{i+1/2}\right)^{n+1}}\left(\frac{P_{i+1}-P_i}{dx} - \left(\frac{\sigma\kappa_{i+1/2}(\alpha_{i+1}-\alpha_i)}{dx}\right)^{n+1}\right) \tag{84}$$

$$\begin{aligned} 3rd: \frac{dt}{4\rho_{i+1/2}}\left(\frac{P_{i+1}-P_i}{dx} - \frac{\sigma\kappa_{i+1/2}(\alpha_{i+1}-\alpha_i)}{dx}\right) + \frac{dt}{4\rho_{i-1/2}}\left(\frac{P_i-P_{i-1}}{dx} - \frac{\sigma\kappa_{i-1/2}(\alpha_i-\alpha_{i-1})}{dx}\right) + \\ \frac{dt}{4\rho_{i+3/2}}\left(\frac{P_{i+2}-P_{i+1}}{dx} - \frac{\sigma\kappa_{i+3/2}(\alpha_{i+2}-\alpha_{i+1})}{dx}\right) + \frac{dt}{4\rho_{i+1/2}}\left(\frac{P_{i+1}-P_i}{dx} - \frac{\sigma\kappa_{i+1/2}(\alpha_{i+1}-\alpha_i)}{dx}\right) \end{aligned} \tag{85}$$

Finally, $u_{i+1/2}^*$ can be calculated as:

$$u_{i+1/2}^* = 1st - 2st + 3st \tag{86}$$

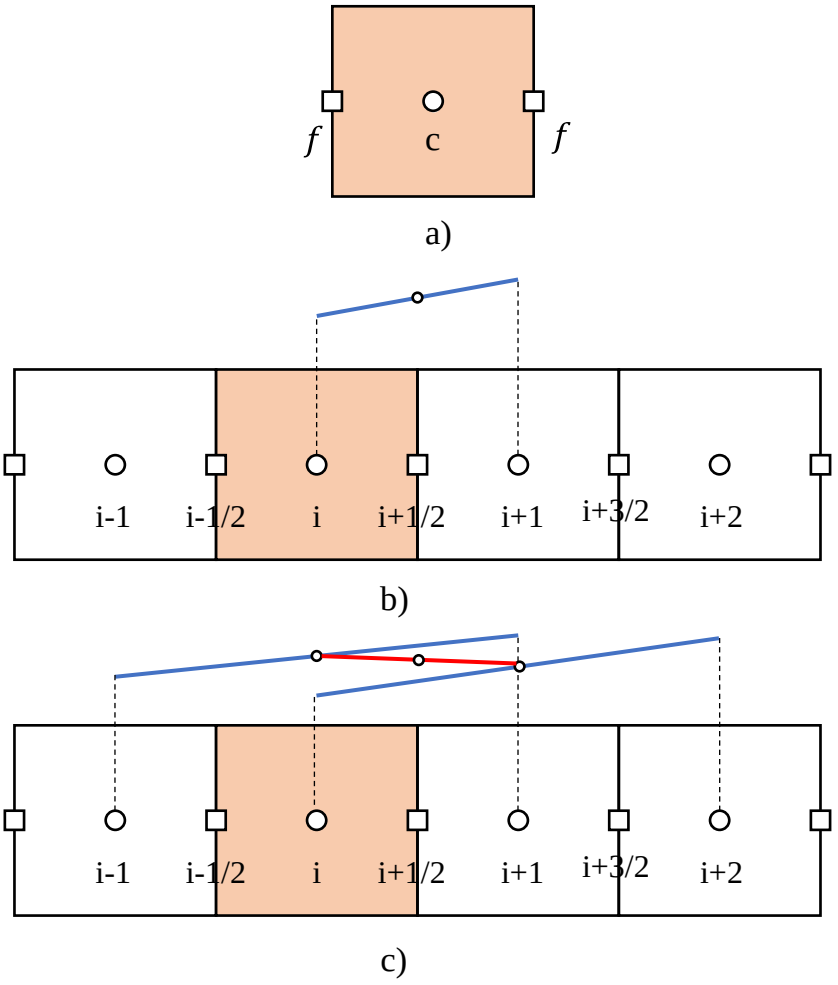

Figure 58: Cell index notation for the Rhie and Chow correction. A) cell-center c and face *f* location, b) stencil used to calculate the first term of pressure correction, c) stencil used to calculate the second term of pressure correction

5.3 Height Function method

As pointed out by Popinet [82], the smooth void fraction method is one of the causes of spurious currents. Hence, the estimate of curvature must be changed. The Height Function (HF) method is a good candidate to solve this problem. It is based on the idea that a local coordinate system can always be defined to determine the interface curvature which mean that in each cell we always can construct a stencil for capturing curvature. In this method, the interface curvature κ is calculated from the derivatives of the height occupied by the fluid, constructed by integrating the void fraction along the direction of the largest component of the normal interface vector [86]. However, the HF method can only be successfully achieved if the mesh is adequately refined. There have been several efforts to calculated HF:

5.3.1 Standard Height Function (SHF)

To evaluate the Standerd Height Function (SHF), few steps are followed:

Find the maximum normal component vector and construct a $3 \times 3 \times 7$ stencil centered on the cell where the curvature is evaluated. The direction of the stencil will be aligned with the largest interface component vector.

Integrate the local interface height.

Compute the curvature using finite-difference derivatives of the HF.

To clarify the HF idea, an example of this technique is used to evaluate 3D curvature. Consider the largest direction of the normal vector is z direction. Nine local heights are constructed in the z direction by summing the volume fraction inside the created stencil. The local HF in a i, j, k Cartesian grid can be depicted as:

$$H_{i,j,k} = \sum_{k-3}^{k+3} \alpha_{i,j,k}\, \Delta z_k \tag{87}$$

With $i = i' - 1, i', i' + 1$ and $j = j' - 1, j', j' + 1$. $H_{i,j,k}$ are local height functions, the index ranged over 7 cells from cell $i, j, k - 3$ to cell $i, j, k + 3$ and Δz_k is the grid size in the z direction (Figure 59).

The curvature κ is calculated from the height functions using second-order operator:

$$\kappa = \frac{H_{xx} + H_{yy} + H_{xx}H_y^2 + H_{yy}H_x^2 - 2H_{xy}H_xH_y}{\left(1 + H_x^2 + H_y^2\right)^{\frac{3}{2}}} \tag{88}$$

Where the derivatives $H_x, H_y, \ldots$ are calculated using a second-order finite differencing scheme.

$$H_x = \frac{H_{i+1,j,k} - H_{i-1,j,k}}{2\Delta x} \tag{89}$$

$$H_y = \frac{H_{i,j+1,k} - H_{i,j+1,k}}{2\Delta y} \tag{90}$$

$$H_{xx} = \frac{H_{i+1,j,k} - 2H_{i,j,k} + H_{i-1,j,k}}{2\Delta x^2} \tag{91}$$

$$H_{yy} = \frac{H_{i,j+1,k} - 2H_{i,j,k} + H_{i,j-1,k}}{2\Delta y^2} \tag{92}$$

$$H_{xy} = \frac{H_{i+1,j+1,k} - H_{i+1,j-,k} - H_{i-1,j+1,k} + H_{i-1,j-1,k}}{2\Delta x \Delta y} \tag{93}$$

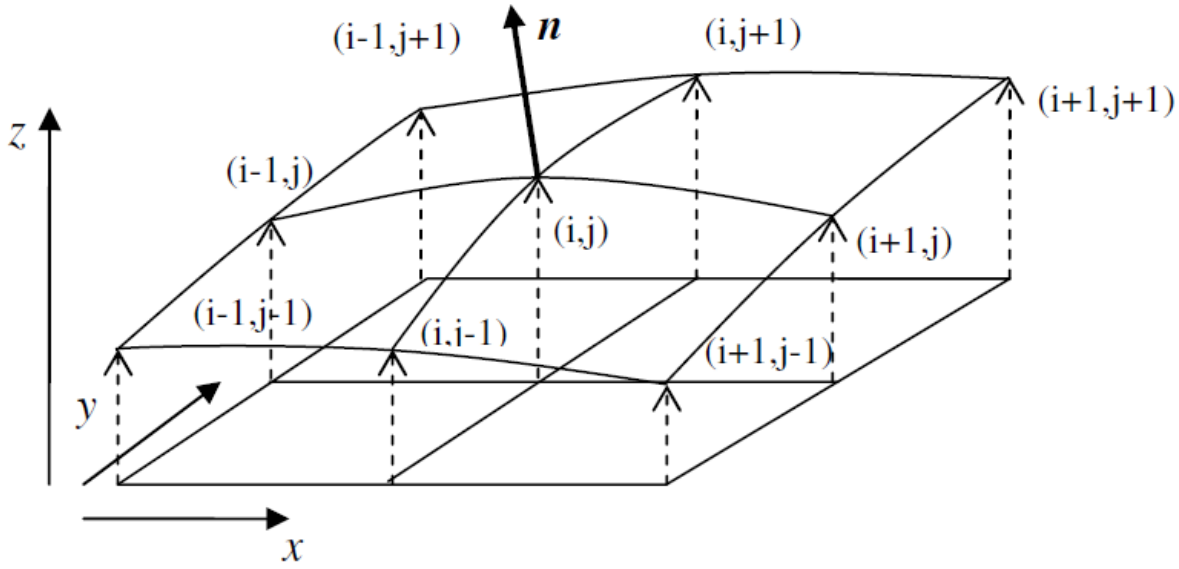

Figure 59: Illustration of the nine local height functions for curvature estimation in 3D [85]

5.3.2 Generalized Height Function (GHF)

The limitations of the Standard Height Function (illustrated red dashed in Figure 60) method become increasingly apparent in specific interface configurations, particularly when dealing with under-resolved curvature, as illustrated in Figure 60. The Generalized Height Function method employs an adaptive stencil to compute heights, providing a more accurate estimate of curvature, especially in complex topologies. Unlike the SHF method, which uses a fixed stencil, the GHF method dynamically constructs its stencil. Initially, it searches in the direction where the normal vector is largest until it finds cells with void fractions of both 0 and 1, and then constructs the height. If the search yields an inconsistent column (i.e., cells with void fractions other than 0 and 1), the method adjusts the direction of the stencil and conducts a new search. Once all heights are identified, the method calculates curvature in a manner similar to the SHF method. As shown in Figure 60, the curvature calculated by GHF is -0.229, compared to -0.313 by the SHF method, while the exact curvature is -0.189. This suggests that GHF is more accurate, particularly in critical cells.

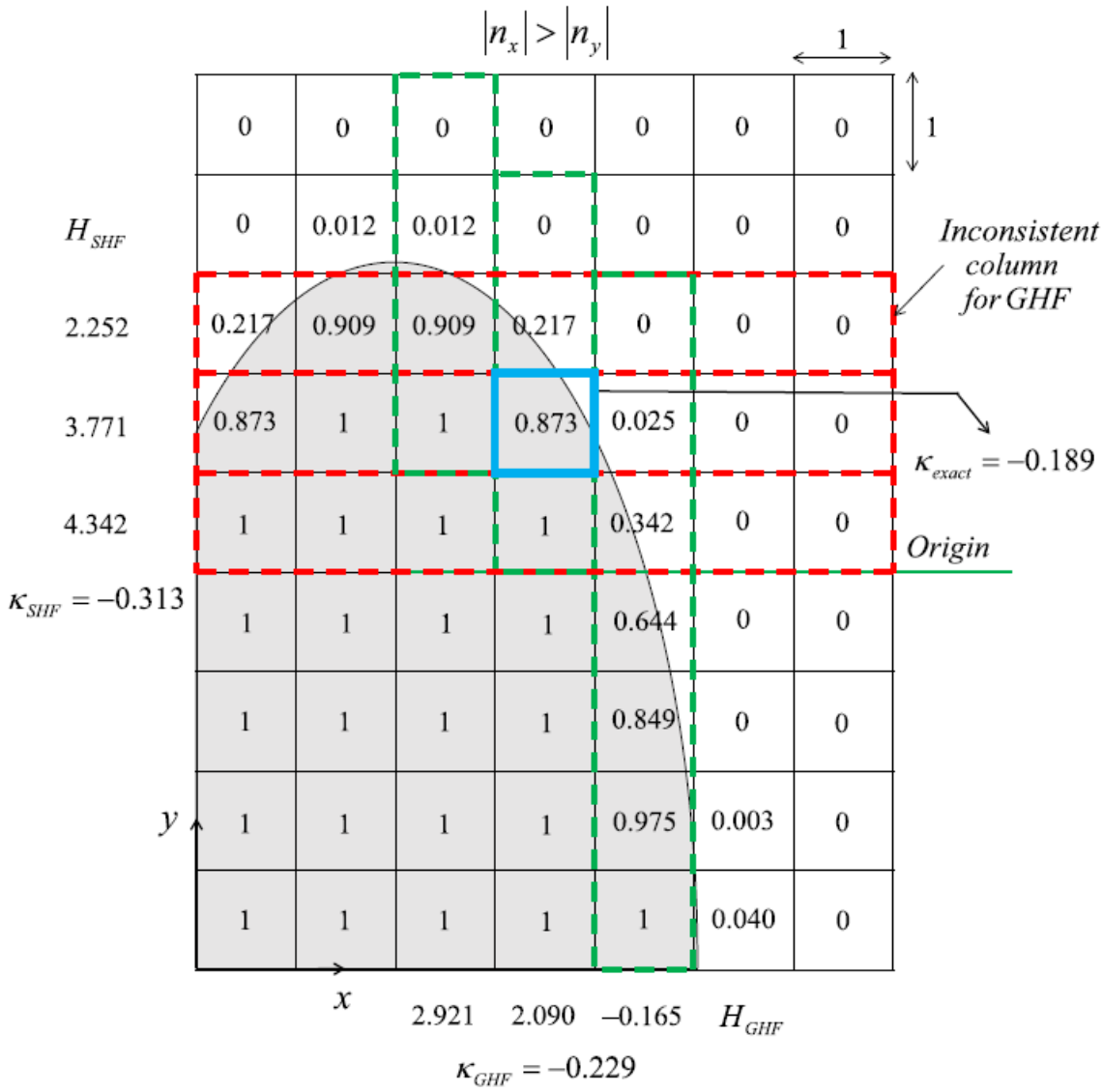

Figure 60. Comparison the accuracy of SHF and GHF methods at critical cell. SHF stencil (- -) and GHF stencil (- -) are built around critical cell [87].

5.3.3 Mesh decoupling

Another case is shown in Figure 61a), where even the Generalized Height Function is not sufficient for calculating curvature. This typically occurs when the mesh is either too coarse or the curvature is so pronounced that its diameter is smaller than about 4 to 6 times the mesh size. The concept of mesh-decoupling in Height Function was initially introduced by Liovic et al. [88]. Their method constructs the HF along the diagonal direction of an orthogonal mesh. Results have shown that this approach significantly reduces the maximum error in curvature calculations for a sphere (Figure 61b).

Owkes and Desjardins [89] further refined this methodology by computing the HF in a coordinate system that is orthonormal to the interface normal. Their method employs columns with parameterized width and depth, as depicted in Figure 61c), where the width is less than the mesh size. Results confirm that this technique is robust and does not fail in curvature calculations, provided the radius of curvature is greater than $2\Delta x$.

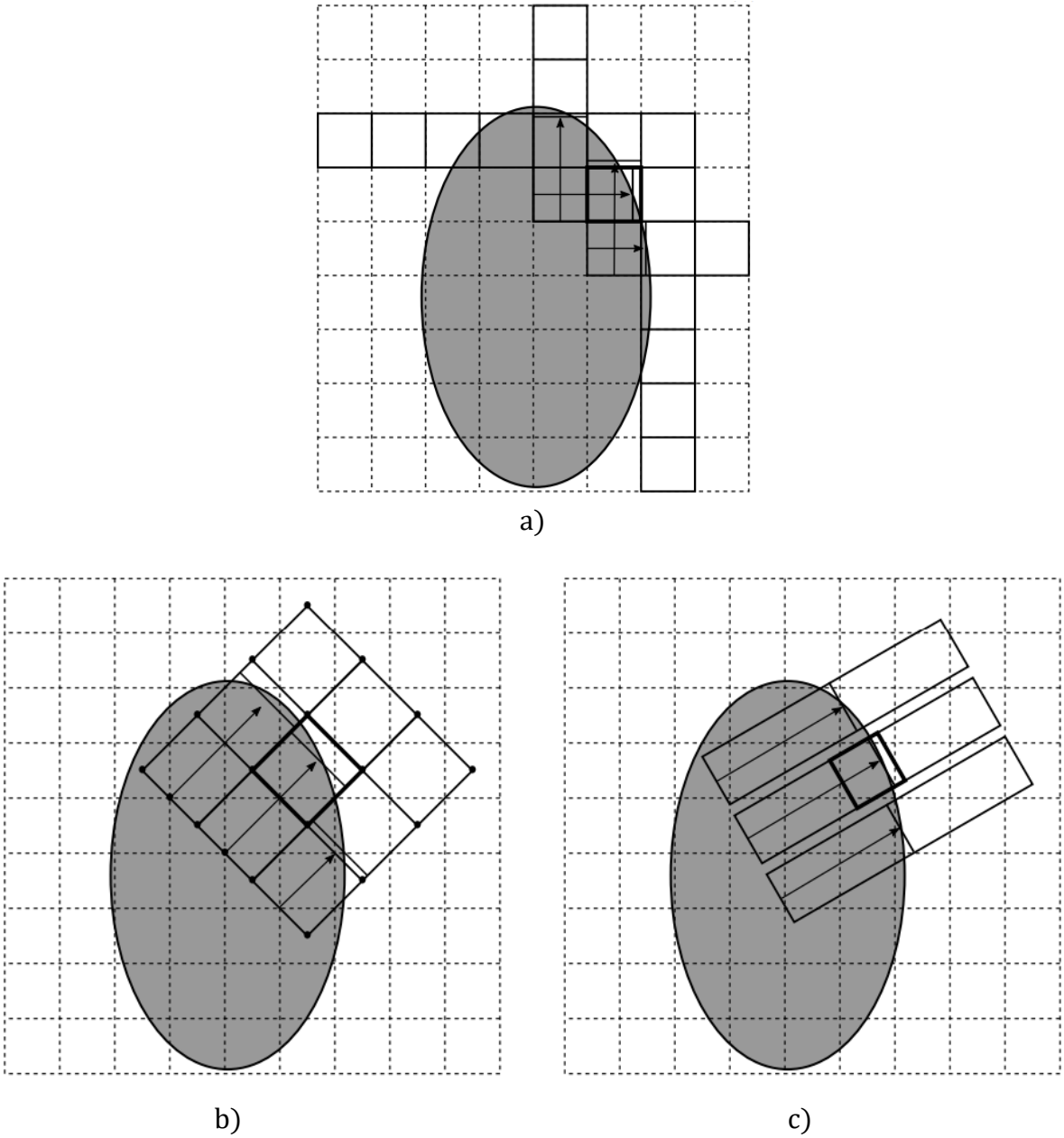

Figure 61. Boniou schematic [90] a) Non consistent HF reconstructions; b) Liovic et al. [88] mesh decoupled HF methodology; c) Owkes et al. [89] mesh decoupled HF methodology

Although the mesh decoupling method is robust and effective, it only shows significant improvement when the mesh at the interface is very coarse. This is rarely encountered in two-phase flow, where the interface is typically refined to accurately capture it. To avoid complexity in implementation, only GHF is implemented in the Converge code. For simplicity, we will use the term 'HF' from this point forward in the thesis, implicitly indicating that it refers to GHF.

5.4 Implementation of the contact angle model

In this section, the implementation of the Cox's model presented in Section 2.3.4 in Converge is shown in details. The contact angle is implemented as a boundary condition by altering the interface curvature at the wall boundary cells (Figure 62). This is done by rotating interface normal in order to account for the contact angle as [40,55]:

$$n = n_s \cos(\theta) + n_t \cos(\theta) \tag{94}$$

Where n is the normal interface vector at the boundary, n_s is the wall surface normal vector, n_t is the tangential vector pointing along the wall into liquid, and θ is the static or dynamic contact angle. The main difference between the static versus dynamic contact angle model is that θ vary with time for the dynamic contact angle model.

The direction of the tangential vector is given by [40]:

$$n_t = n_s \times \frac{\nabla C}{|\nabla C|} \times n_s \tag{95}$$

As shown by the algorithm of Figure 62, before retrieving the dynamic contact angle, the contact line velocity V_{cl} based on the tangential component of the fluid velocity in the first cell close to the wall, u_{cell} [40,91] needs to be calculated:

$$V_{cl} = n_s \times u_{cell} \times n_s \tag{96}$$

The direction of the contact line velocity V_{cl} is also needed to establish the receding or advancing state. Then θ is calculated by Equation (33).

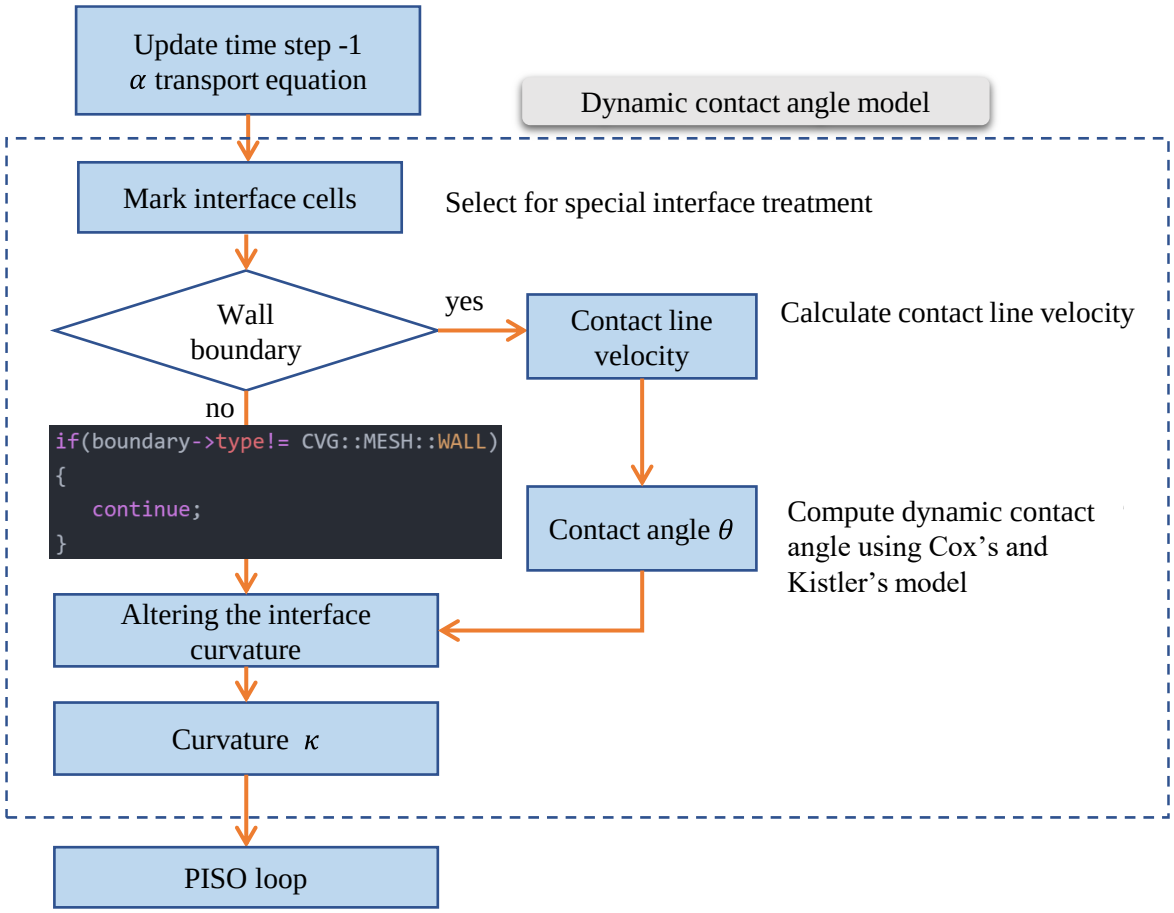

Figure 62: The workflow for the implementation of the dynamic contact angle in Converge

5.4.1 Contact angle implementation with the SVF method

In the SVF method, the contact angle is implemented as a boundary condition by altering the normal of the interface at the wall boundary cells, $\mathbf{n_{cl}}$. This is done by rotating the normal to the interface by an angle equal to the dynamic contact angle as:

$$\mathbf{n_{cl}} = n_s \cos(\theta_d) + n_t \cos(\theta_d) \tag{97}$$

where the unit vectors n_s and n_t are the normal and tangential vectors to the wall, respectively. The dynamic contact angle θ_d is calculated based on the Kistler model or the Cox model. Then, the curvature is updated in the contact line cell and used to calculate the surface tension term, equation (1).

5.4.2 Contact angle implementation with the HF method

In the HF method, the curvature will be directly modified in the contact line cell using fluid heights. For example, in 2D, for contact angle between 45° and 135, height functions are constructed horizontally (Figure 63a). It requires h_{i-1} parallel to the solid surface, that is defined so that the angle between the interface normal in the contact line cell and the solid normal is the dynamic contact angle:

$$h_{i-1} = h_i + \frac{\Delta}{tan\theta_d} \tag{98}$$

where Δ is the mesh size. This method is extended for contact angle smaller than 45° or larger than 135°.

To compute the curvature in the contact line cell in 3D, nine local heights are required to complete the stencil; but only six heights above the wall can be directly retrieved from the void fraction field. The three height functions below the wall ($H_{i-1,j-1}; H_{i,j-1}; H_{i+1,j-1}$) are calculated based on the dynamic contact angle and the existed heights as:

$$\begin{aligned} H_{i-1,j-1} &= H_{i-1,j} + \frac{\Delta}{tan\theta_d cos\beta} \\ H_{i,j-1} &= H_{i,j} + \frac{\Delta}{tan\theta_d\, cos\beta} \\ H_{i+1,j-1} &= H_{i+1,j} + \frac{\Delta}{tan\theta_d cos\beta} \end{aligned} \tag{99}$$

where $cos\beta$ is defined as:

$$cos\beta = \frac{(n_{xy} \cdot n_h)}{|n_{xy}||n_h|} \tag{100}$$

with n_{xy}, the projection on xy plane of the interface normal **n:**

$$n_{xy} = \mathbf{n} - \left(\frac{(\mathbf{n} \cdot n_s)}{\|n_s\|^2}\right) n_s \tag{101}$$

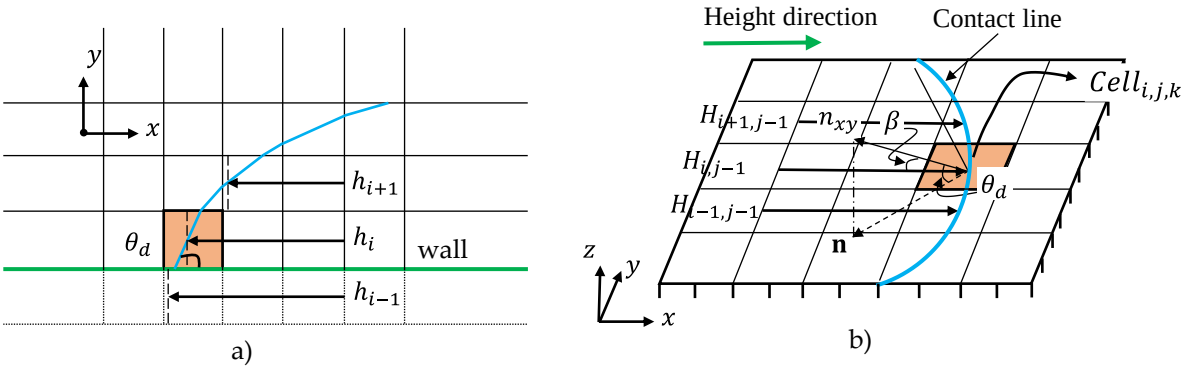

Figure 63: 2D and 3D construction of height functions for contact angle between 45° and 135°

5.5 Conclusion

The updated numerical model has been introduced in the current Converge CFD software with the aim to more accurately capture the simulation of physical phenomena and reduce errors. First, a well-balanced algorithm for the PISO procedure in two-phase flow is presented, which utilizes a collocated grid. This method discretizes surface tension and pressure gradient simultaneously at the same location, ensuring equilibrium. This equilibrium is crucial in minimizing spurious currents during 2-phase flow simulations. Next, the Height Function method is introduced as an alternative to the traditional SVF method found in Converge CFD code. This approach offers a more accurate estimation of curvature, which is essential for accurately calculating surface tension force, thus reducing undesired spurious velocities. Additionally, the dynamic contact angle has been incorporated to better capture the surface tension force at the wall boundary. This aligns with the objectives detailed in Chapter 2, aiming to accurately depict the physical interactions between liquid-gas and solid surfaces at the contact line.

Chapter 6

Stationary and spreading droplet

This chapter focuses on validating the advancements introduced in Chapter 5 using various cases. These include a stationary droplet, a spreading droplet driven by the contact line, and a droplet spreading due to both gravity and the contact line.

6.1 Introduction

The well-balanced formulation for PISO algorithm, the HF method as well as the dynamic contact angle models have been implemented in Converge software [92]. Several tests were carried out in this chapter to evaluate the improvement provided by these methods. The unbalanced formulation of the PISO algorithm combined with the Smooth Void Fraction method is referred to as NWB-SVF method. The unbalanced formulation of the PISO algorithm combined with the Height Function method is referred to as NWB-HF method. Finally, the well-balanced PISO algorithm combined with the Height Function method is referred to as WB-HF method.

In two-phase flow simulation with PLIC method, the max timestep of simulation to get the numerical stability is given by [82]:

$$\Delta t = \sqrt{\frac{0{,}5 * (\rho_1 + \rho_2)\Delta^3}{\pi\sigma}} \tag{102}$$

Where ρ_1, ρ_2 are the density on either side through the interface.

For droplet simulation, the mesh resolution performs well when the computational domain is meshed at a size range from 25-64 cells per radius [40,93,94]. Hence in this study, the minimum mesh size 1/30 radius is used for all simulations.

6.2 Two-dimensional stationary droplet

To evaluate the improvement provided by the WB-HF method, the case of a 2D static droplet at equilibrium without the effect of gravity is considered. The computational domain is a 2 m square and a droplet with a radius of 0.4 m is initially positioned at the center of the domain (Figure 64). This case corresponds to the test case analyzed by Abadie [95]. The density of the two fluids is equally fixed to 1000, the viscosity of the two fluids is set equally to 0.2582 $N\frac{s}{m^2}$. The surface tension coefficient σ is 1.

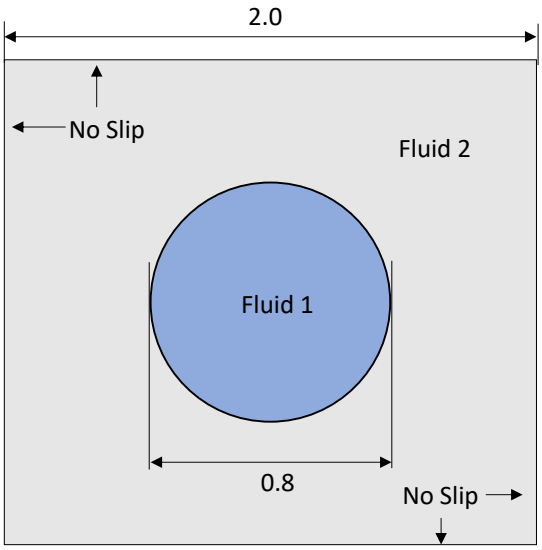

Figure 64. Computational domain for the stationary droplet case

Under these conditions, the steady-state momentum equation is reduced to:

$$\Delta p = F \Leftrightarrow\ p_1 - p_2 = \sigma \kappa_{exact} \tag{103}$$

Since the interface of the 2D droplet is a circle, the curvature κ_{exact} can theoretically be calculated as follows:

$$\kappa_{exact} = \frac{1}{R} \tag{104}$$

By replacing $R = 0.4$, the exact curvature κ_{exact} is equal to 2.5 and therefore the pressure difference across the interface Δp is equal to 2.5.

The magnitude of parasitic velocity is evaluated with the maximum of the Capillary number defined as:

$$Ca_{max} = \frac{U_{max}}{U_\sigma} \tag{105}$$

Where $U_{max} = \max(|\boldsymbol{U}|)$ is the absolute magnitude of parasitic velocity, $U_\sigma = \frac{\sigma}{\mu_1}$ is a non-dimensional velocity scale; a non-dimensional time scale $t_\sigma = \sqrt{\frac{\rho D_0^3}{\sigma}}$ is also defined for post-processing.

Figure 65 shows the spurious currents field at $\frac{t}{t_\sigma} = 10$ for a fixed grid of 30 cells per radius, obtained with the NWB-SVF method (Figure 65a), with the NWB-HF method (Figure 65b) and with the WB-HF method (Figure 65c). Using the SVF method to calculate the curvature results in spurious currents about 20 times larger than with the HF method (Figure 65a vs. Figure 65b). A better estimation of the curvature allows to decrease the spurious currents but also to preserve the roundness of the interface. However, the spurious currents in Figure 65b remain highly concentrated around the interface. Furthermore, as shown in Figure 65c, when the PISO algorithm is well-balanced, the spurious currents are reduced by about a factor of 40 and the parasitic velocity has almost disappeared around the interface. Hence the accuracy of the curvature calculation, as well as a consistent discretization scheme for the pressure gradient and surface tension force, is therefore essential to minimize spurious currents.

Figure 65d presents the time evolution of the magnitude of the spurious currents. With unbalanced treatment of the pressure gradient and surface tension force, the SVF curvature calculation method gives a stable Ca_{max} at 3.10^{-3}, about 20 times greater than with the HF method. Combining the well-balanced PISO algorithm with the HF method, Ca_{max} is again reduced by 2 to 3 orders of magnitude despite some oscillations. The oscillations can be attributed to the fact that the HF method is not perfect when the height direction is strongly misaligned with the normal interface vector [83].

The pressure jump at the interface is also impacted by the numerical methods used to discretize the pressure and surface tension terms and by the curvature calculation, as illustrated in Figure 66. Indeed, the pressure field in Figure 66b shows strong fluctuations around the interface, whereas the pressure jump is sharper with the HF method and does not show any fluctuation. The pressure difference across the interface $(p_1 - p_2)$ is calculated and compared to the exact pressure Δp_{exact} The error on the pressure jump defined by is about 29.8% with the NWB-SVF method but drops dramatically to 0.4% with the WB-HF method.

$$\frac{(p_1 - p_2)}{\Delta p_{exact}} \times 100\% \tag{106}$$

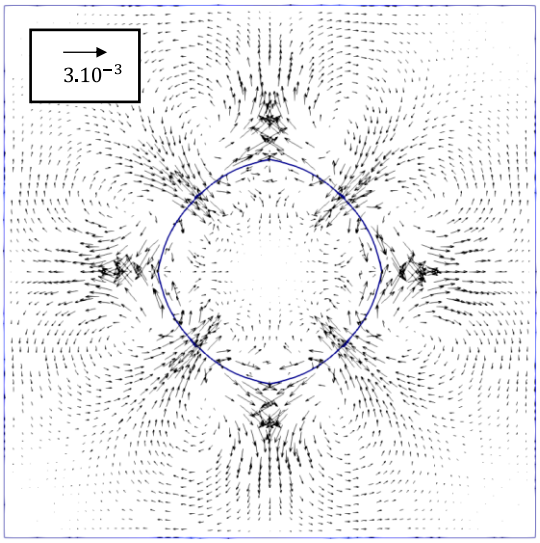

a) $\max(|\boldsymbol{U}|) = 4.10^{-3}$

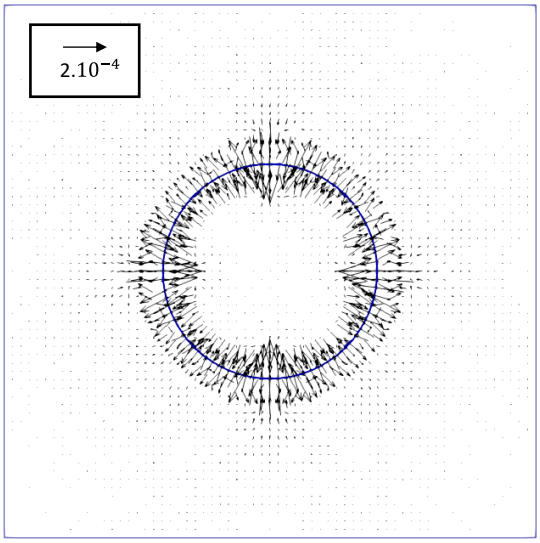

b) $\max(|\boldsymbol{U}|) = 3{,}5.10^{-4}$

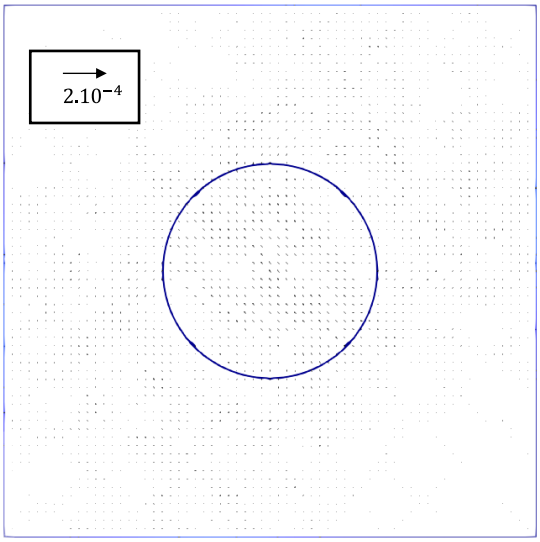

c) $\max(|\boldsymbol{U}|) = 8.10^{-6}$

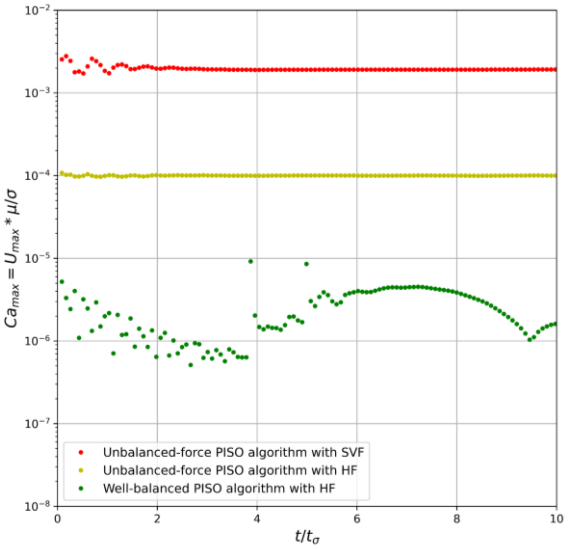

d)

Figure 65. Velocity field (arrows) and droplet shapes (C = 0.5 contours) for the stationary droplet case at $\frac{t}{t_\sigma} = 10$: a) Unbalanced-force PISO algorithm with SVF method (NWB-SVF); b) Unbalanced-force PISO algorithm with HF method (NWB-HF); c) Well-balanced PISO algorithm with HF method (WB-HF); d) Comparison of the time evolution of the maximal spurious currents in the computational domain

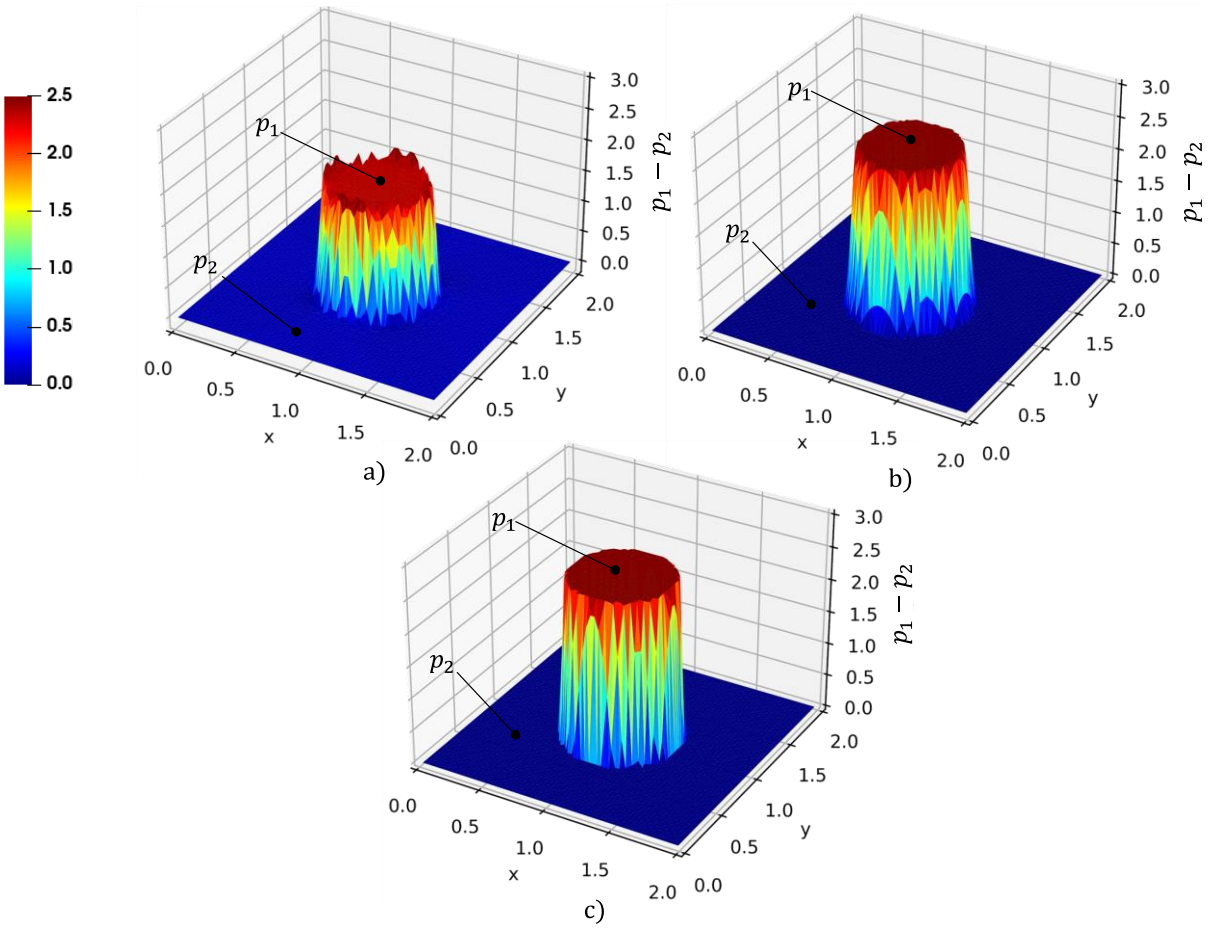

Figure 66. Pressure field for the stationary droplet case at $\frac{t}{t_\sigma} = 10$; a) NWB-SVF method; b) NWB-HF method; c) WB-HF method

6.3 Spreading of a droplet driven by the contact line

The objective of this section is to evaluate the impact of the method used to calculate the curvature on the behavior of the contact line. The test case presented in this section is reported by Legendre [94] and Afkhami [37]. A 3D spherical cap droplet of radius $R_0 = 1$ is initialized on a horizontal flat surface at equilibrium (no gravity effect). The computational domain is a $2R_0$ square box. The initial shape of the droplet corresponds to an initial contact angle of $\theta_i = 90°$ (Figure 67). The wetting condition (no slip and contact angle) is imposed on the bottom horizontal wall whereas no slip conditions are imposed on the other walls of the domain. The fluid properties used in this simulation are: $\rho_{loquid} = \rho_{gas}$=1, $\mu_{liquid} = \mu_{gas} = 0.25$, $\sigma = 7.5$.

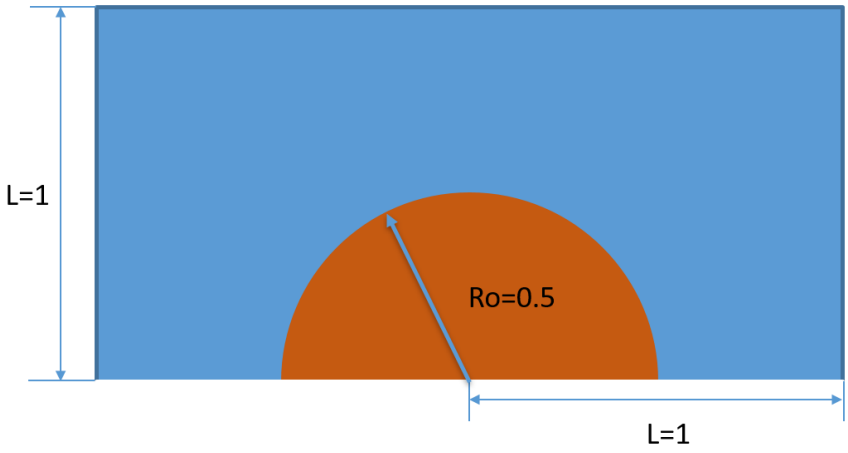

Figure 67. Initial drop shape and computational domain

The computational domain is meshed at the resolution of D/64 dimension of initial diameter as notation as D-64 (Figure 68).

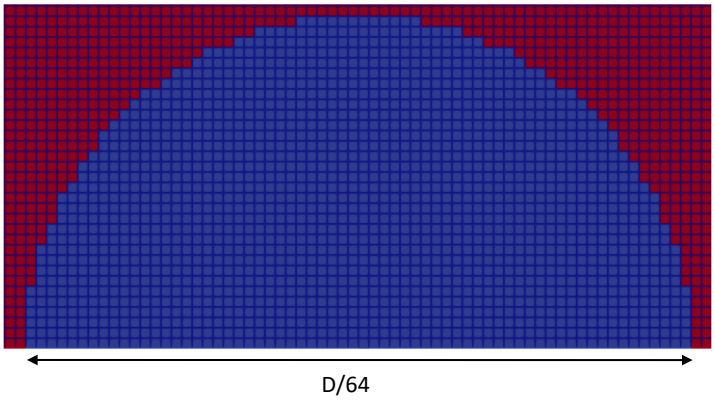

Figure 68 An example of regular mesh at the resolution of D/64

Figure 69 presents a comparative analysis of the wetting radius ratio, specifically the initial wetting radius to the instantaneous wetting radius, during a fluid spreading process. This simulation was conducted with an equilibrium contact angle of 60° and was designed to simulate the spreading until a fully developed stage was reached, over a period of 4 seconds.

In this analysis, two distinct models were employed: the Static Contact Angle (SCA) model and the Dynamic Contact Angle (Cox) model. As the simulation began, both models exhibited an increasing wetting radius, signifying droplet spreading. However, the wetting radius of the SCA model reached a plateau faster than the DCA model. This divergence in behavior can be attributed to the inherent characteristics of these models. The SCA model imposes a fixed contact angle of 60° throughout the process, while the DCA model dynamically adjusts the contact angle in accordance with the real-time progression of the droplet spreading.

This adaptation of the DCA model provides a smoother depiction of physical wetting phenomena. However, the final spreading ratio revealed errors of 2.05% and 3.62% for the SVF-SCA and SVF-DCA models respectively. As outlined in section 6.2, these errors may originate from the SVF model's influence on the fluid interface. This will be discussed in greater detail in the following section.

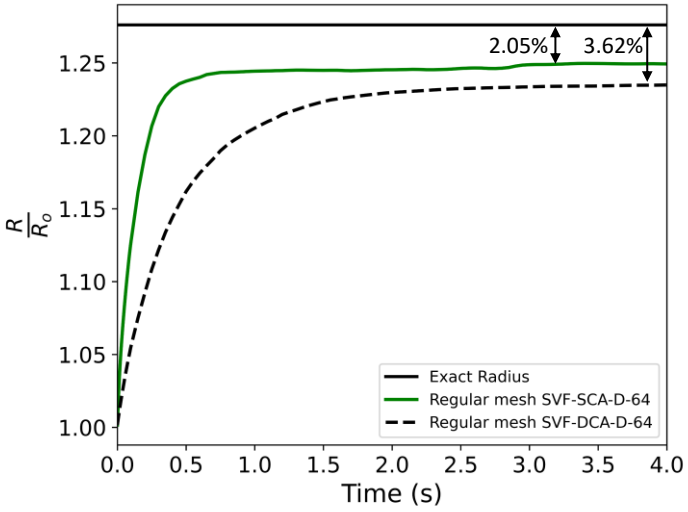

Figure 69 Time evolution of the wetted radius – comparison between the SVF-SCA model and SVF-DCA model for equilibrium contact angles: $\theta_e = 60°$; Mesh resolution was assigned at D-64 (D/64)

A significant technical challenge encountered during these simulations is the limited computational resources, a factor exacerbated by the complexity of a three-dimensional simulation. The simulations

require a substantial number of cells if implemented with a regular mesh, which becomes a constraint considering the resources at hand.

Given that the global velocity in these simulations is low and the capillary forces predominate, capturing the fluid interface with high accuracy is crucial. As such, a reasonable mesh scale is required at the interface, while resolution at other locations could be reduced without compromising overall accuracy. This led us to test the Adaptive Mesh Refinement (AMR) method, aimed at maintaining a constant mesh resolution around the interface while reducing the total number of cells (as shown in Figure 70).

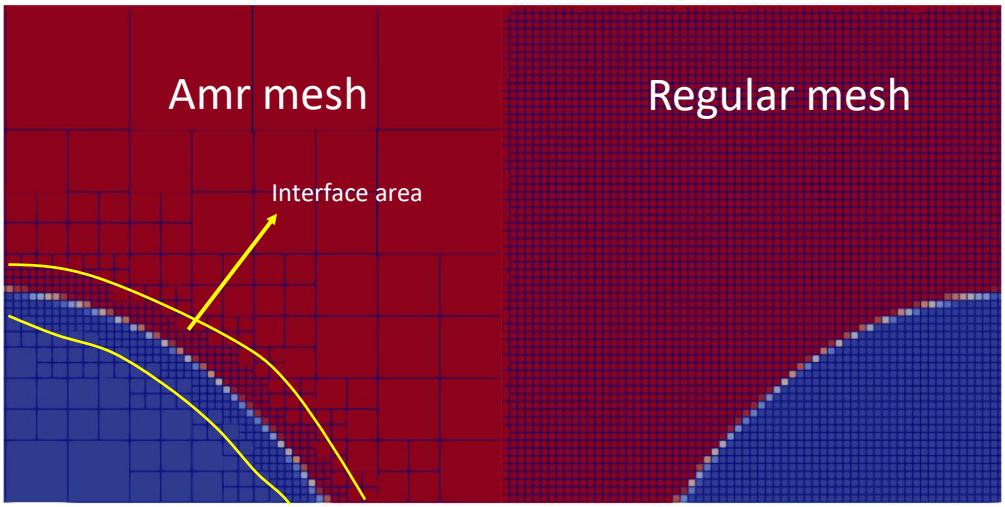

Figure 70 Comparison of AMR mesh structure and regular mesh structure at the resolution of D/64, $\theta_e = 60°$

6.3.1 Impact of mesh strategy

In Figure 71, the spreading ratios of different cases using AMR and regular mesh is compared, with mesh resolution at D/64, for both DCA and SCA models. The results indicate that using AMR compared to a regular mesh has only a negligible impact. With the DCA model, there is hardly no discernible difference between the results obtained with AMR and the regular mesh. However, with the SCA model, a minor difference (less than 0.2%) becomes apparent from the time point of 2.7 seconds onward.

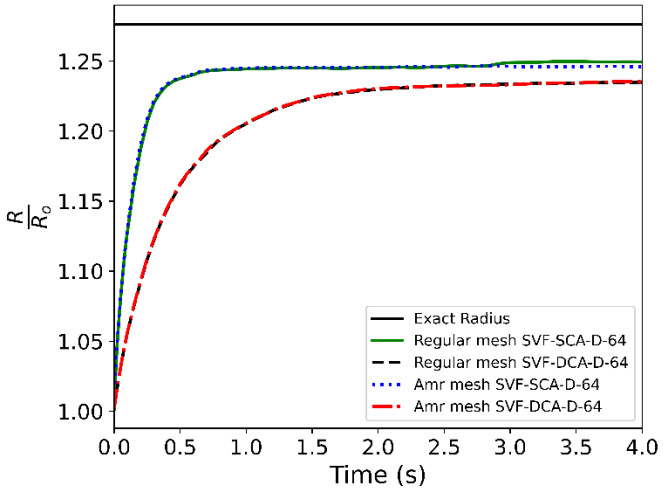

Figure 71 Time evolution of the wetted radius. Comparison of spreading ratio between AMR mesh and regular mesh at the resolution of D/64, $\theta_e = 60°$;

Though this difference is small, the use of AMR results in substantial computational savings, reducing simulation time by almost 20 times (as demonstrated in Table 3). The average simulation time per timestep for AMR is approximately 2 seconds, whereas a regular mesh configuration requires about 40 seconds per time step.

Table 3 Comparison CPU time of AMR mesh and regular mesh

Case	Average CPU time per time-step (time-step* #processors)	Number of cells
Regular mesh SVF-sca-D-64	39.744	2097152
Regular mesh SVF-dca-D-64	41.184	2097152
Amr mesh SVF-sca-D-64	2.088	≈ 22689
Amr mesh SVF-dca-D-64	2.099	≈ 22689

Given this balance between cost and benefits, the application of AMR proves highly beneficial for this kind of simulation. Accordingly, AMR will be the chosen method for all further simulations discussed in Chapter 5.

6.3.2 Mesh convergence review

In this study, the PLIC-VOF method is used to track the interface. This method utilizes cell face normal velocities to advect volume fraction, as described in Chapter 2. This implies that the method includes an implicit slip length at the no-slip boundary. However, this implicit slip length is proportional to the mesh at the contact line. Even with a no-slip boundary condition where $v_{wall} = 0$, the contact line can move because the velocity at the face of the contact line cell is different from zero. This means that when resizing the mesh at the contact line, the face velocity decreases, leading to a reduced implicit slip length. This results in convergence breaking when the mesh size decreases, as indicated by Afkhami [37]. Figure 72 shows a withdrawing plate test conducted by Afkhami [37] with different mesh sizes. As expected, the interface does not converge as $\Delta \rightarrow 0$; the height of the contact line increases as the mesh size decreases. Therefore, to allow the liquid phase to slide on the wall, one must carefully choose the mesh so that the implicit slip-length is large enough to let the liquid slide, while ensuring the mesh is fine enough to yield reliable results. Put in the conclusion that we should try to use navier slip boundary condition. (out in the perspective_

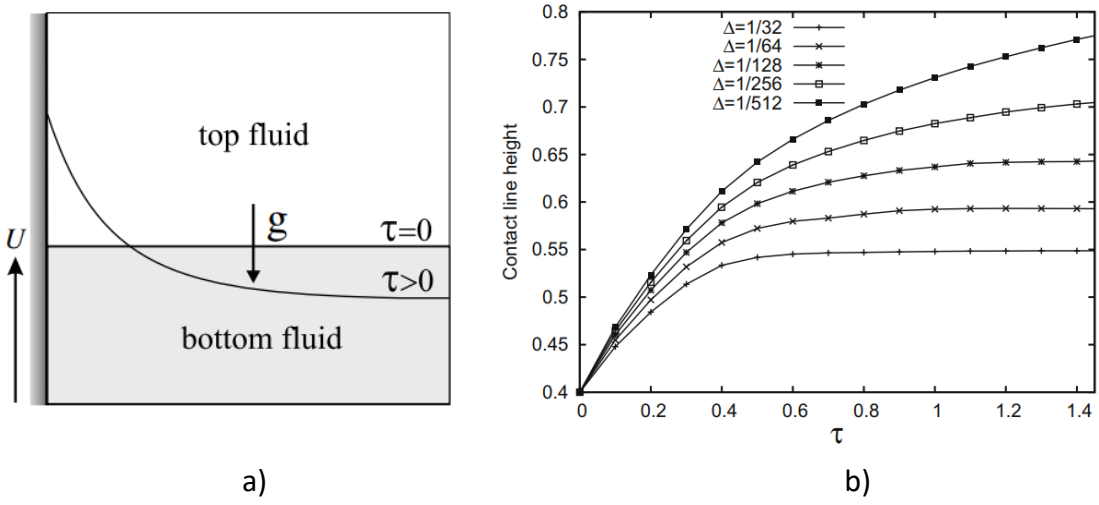

Figure 72. a) The withdrawing plate; b) Contact line height when apply a no-slip boundary condition along the wall [37]

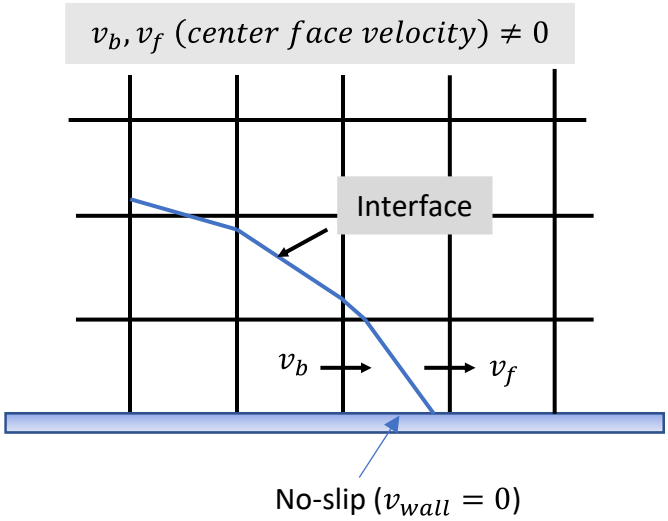

Figure 73. PLIC method use cell face normal velocities to advect the void fraction

6.3.3 Mesh sensitivity study

The results presented so far have focused on a mesh resolution of D/64. However, it is important to conduct a mesh convergence test, particularly for capillary flow simulations to see if there are any effects of mesh divergence.

Figure 74 presents the comparison of three different mesh resolutions (ranging from D/16 to D/64) for two models: Smooth Void Fraction-SCA (SVF-SCA) and Smooth Void Fraction-DCA (SVF-DCA). It is obvious that mesh convergence is not achieved upon refining the mesh. This can be attributed to the unbalanced of solver and curvature calculation method. The PLIC approach relies on cell center face velocity to advect the void fraction. Face velocity near the wall is particularly sensitive to mesh quality, making the wetted area similarly sensitive to mesh refinement, as discussed in more detail in Chapter 7. Curvature calculated by SVF method also contribute to the error of wetted radius due to the degree of one order accuracy. Nonetheless, refining the mesh does lead to a mesh convergence for both SVF-SCA and SVF-DCA when compared with the theoretical radius.

For a more in-depth look, as the simulation is launched, the radius ratio of both SCA and DCA models increase, influenced by the equilibrium contact angle ($\theta_e = 60$) (Figure 74). The SVF-SCA model reaches a plateau much more rapidly compared to the SVF-DCA model. Across all three mesh scales, the radius ratio of SVF-DCA model is at around 0.4, a behavior attributed to the SCA model's fixed contact angle of 60°. In contrast, the DCA model's contact angle evolves in tandem with the contact line velocity, leading it to reach the plateau at varied times. For instance, at a mesh scale of D-32, the radius ratio for the SVF-SCA case reaches 1.23 after only 0.4 seconds, while the DCA model takes

about 3 seconds to plateau at a radius ratio of 1.22. This suggests that it take longer and the final wetting area in the DCA model is smaller than that in the SCA model.

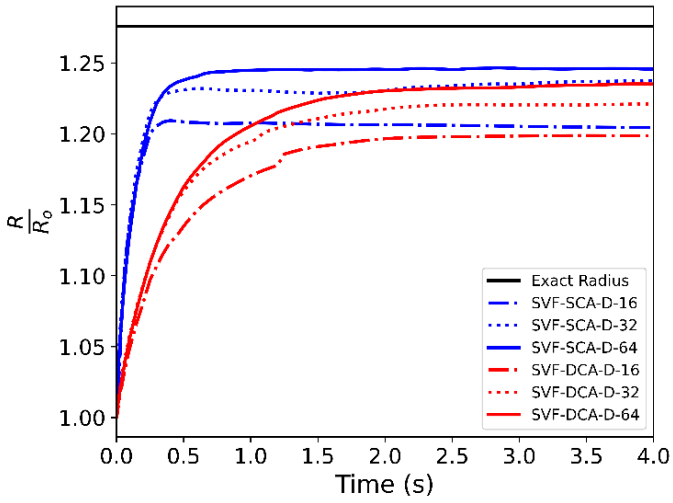

Figure 74 Time evolution of the wetted radius. Grid sensitivity tests of SVF-SCA and SVF-DCA, $\theta_e = 60°$

Contrasting these results, simulations conducted using the HF method (as illustrated in Figure 75) portrayed a different scenario. Both the HF-SCA and HF-DCA models showed excellent agreement with the theoretical exact radius, especially at mesh resolution higher than D/32. Moreover, at the same mesh resolution, both HF-SCA and HF-DCA converged at the same radius, unlike their SVF counterparts. For additional context, the HF-SCA and HF-DCA share the same trends with SVF-SCA and SVF-DCA. Where the radius ratio for HF-SCA reaches a plateau more quickly than HF-DCA. However, the HF method results are more closely aligned with theoretical predictions than those from the SVF method.

At a coarser mesh resolution of D-16, neither HF model successfully converges to the theoretical radius. When the mesh size is reduced to D-32, both appear to align accurately with theoretical data. Interestingly, at an even finer mesh of D-64, only HF-DCA continues to slightly converge towards the theoretical radius, while HF-SCA starts to overestimate it.

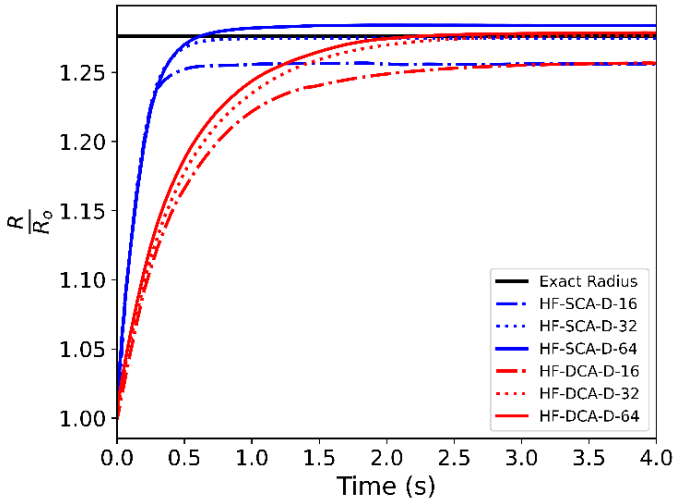

Figure 75 Time evolution of the wetted radius. Grid independence test of HF-SCA and HF-DCA, $\theta_e = 60°$

To comparing our findings with other research in this simulation to see any improvement, the results is compared with Legendre's results [39]. Legendre's work employed a two-dimensional axisymmetric computational domain, the interface location is control by Flux-Corrected-Transport schemes and the interface force is solved using the classical Continuum Surface Force model. Due to 2D simulation can impact the curvature shape. To further emphasize this phenomenon, a specific 1/4 domain case is introduced, which makes use of two symmetry boundary faces as shown in Figure 76c). This scenario can be viewed as a transitional case between Legendre's setup and our fully three-dimensional setup (the final shape of the spreading droplet is depicted in Figure 76).

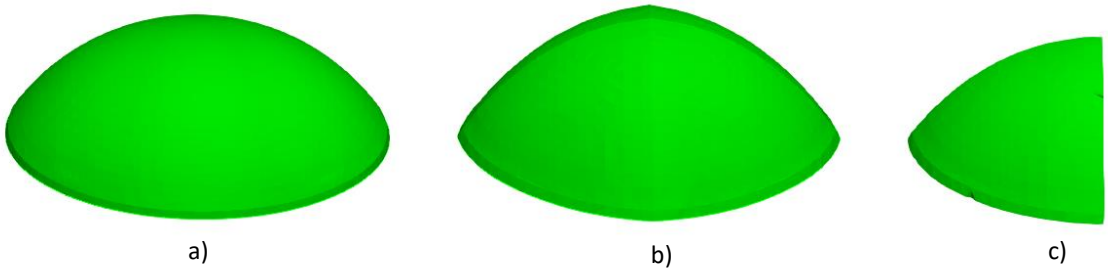

Figure 76 Numerical results of spreading droplet at final state, $\theta_e = 60°$; a) HF-DCA b) SVF-DCA, b) ¼ domain SVF-DCA

Figure 77a) displays the spreading ratio results. The error in the spreading ratio decreases when symmetry boundary conditions are applied. This result is attributed to the fact that the SVF method

calculates curvature at the first order of accuracy. Contrastingly, the HF method calculates curvature at the second order, hence, even in fully 3D domain, it shows higher accuracy. In fact, the HF method even demonstrates less error compared to Legendre's results [39]. In a more detail, there are significant different between HF-DCA and SVF-DCA at final radius ratio at time equal 3s. Where the error of SVF-DCA is significantly higher than HF-DCA. This error is suspected to be due to its inability to maintain the droplet's spherical shape, a phenomenon potentially attributed to the presence of spurious currents and one order accuracy. Hence to SVF-DC cannot maintain the spherical shape lead to final radius ratio is big different (Figure 76and Figure 77a)).

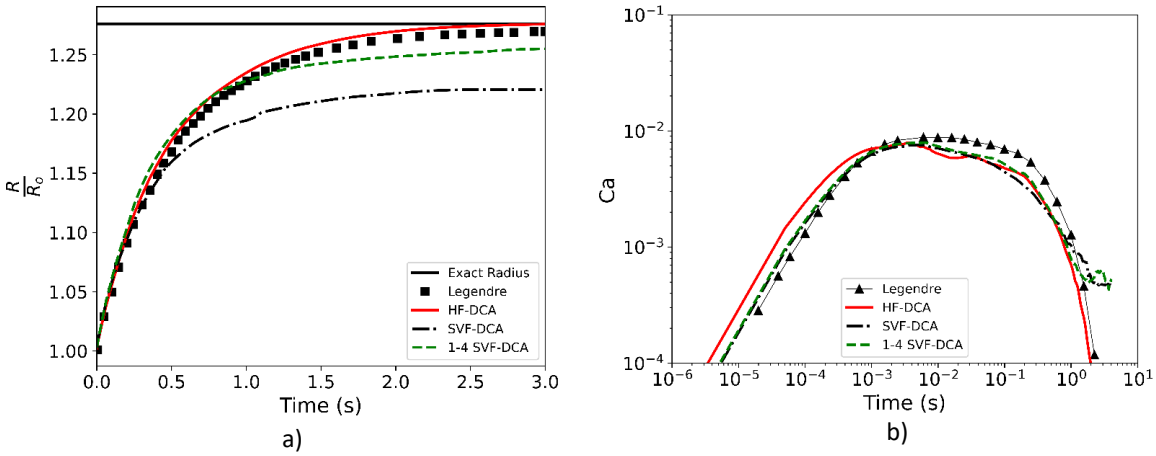

Figure 77 Comparison with Legendre. a) spreading ratio b) Capillary number

Figure 77b) presents the temporal evolution of the contact line velocity, using the same simulation data as Figure 77a). An important feature of these results is the rapid initial change in the contact line velocity, followed by a gradual decrease as it approaches the final state.

The results indicate that the contact line velocity for all simulations, including the Legendre case [39], initially increases swiftly. Thereafter, the velocity plateaus from $10^{-3}s$ to $8.10^{-1}s$ before eventually decreasing over time to reach the final state. Notably, both the 1/4 SVF-DCA and SVF-DCA simulations exhibit similar trends, with minor differences occurring from $4.10^{-1}s$ onward. However, the HF-DCA model demonstrates a slightly different trend, reaching the plateau phase slightly faster than the other cases. Moreover, beyond a simulation time of 1s, the Capillary numbers for the 1/4 SVF-DCA and SVF-DCA remain robust at around 10^{-3}, while the HF-DCA's Capillary number is less than 10^{-4}. This is critical especially when simulating capillary flow, as it alleviates the errors associated with spurious currents in the contact line model.

In an attempt to model a hydrophobic surface where the final contact angle equals 120 degrees, new simulations were conducted (Figure 78 and Figure 79). The results, as displayed in Figure 78, reveal that at the beginning of the simulation, with a contact angle of 120 degrees, the wetting radius of both cases decrease. However, the wetting radius in the SVF-DCA scenario is smaller than the exact radius and lacks stability. Contrastingly, the radius ratio in the HF-DCA model aligns with the theoretical exact ratio and demonstrates stability. This can be attributed to the previously discussed shortcomings of the SVF method in accurately capturing the interface, as further illustrated in Figure 79.

For further clarification, the wetting areas of both HF-DCA and SVF-DCA models decrease at the same rate until approximately 0.2 seconds, after which they start to diverge. Around the 0.4-second mark, the radius ratio of the HF-DCA method converges strictly to the theoretical value of $\frac{R}{R_0} = 0.74$. On other hand, the radius ratio for SVF-DCA method fluctuates around 0.7. Additionally, examination of the iso-contours of the void fraction at the final state, as shown in Figure 80, reveals significant differences between the two methods. The HF-DCA model maintains a spherical shape, as one would physically expect. In contrast, the iso-contour for the SVF-DCA model shows a ribbed surface, suggesting that the numerical errors inherent to this method contribute to the distortion.

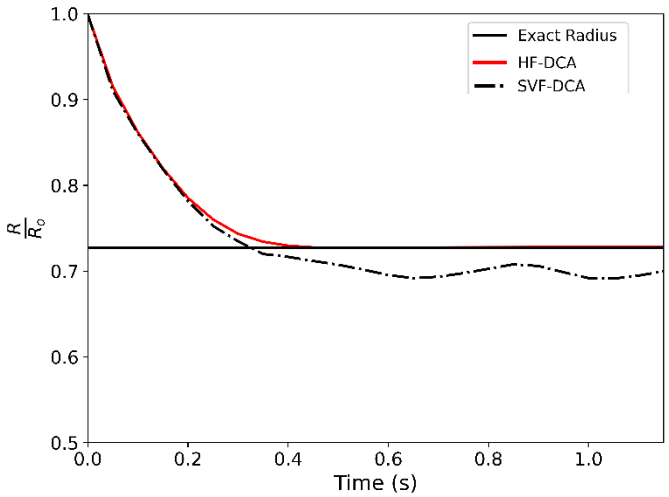

Figure 78 Time evolution of the wetted radius – comparison between the SVF-DCA model and HF-DCA model for equilibrium contact angles: $\theta_e = 120°$

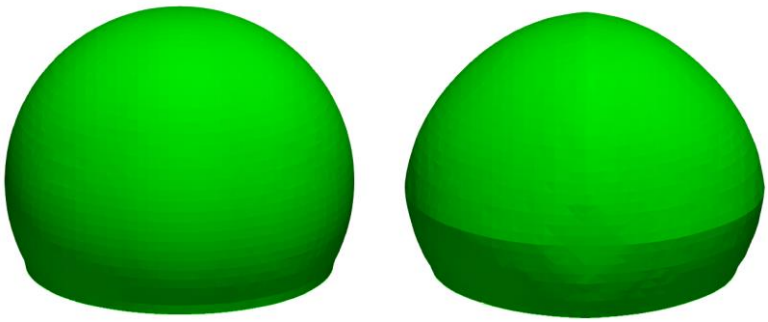

Figure 79 Numerical results of spreading droplet at final state; left SVF method, $\theta_e = 120°$; right HF method, $\theta_e = 120$

6.4 Spreading of a water droplet

Another test involving the spreading of a water droplet is carried out. In this case, we will take into account the effects of both gravity and surface tension force. The goal is to compare the new HF algorithm, when coupled with a dynamic contact angle model, with numerical and experimental results from the literature. The case considered is the Roisman experiment [93] corresponding to the spreading of a water droplet on a dry surface at a low Weber number at different impact velocity. The parameters of the experiment, along with the properties of the liquid used, are detailed in Tables 3 and 4. These tables lay the groundwork for our simulation and allow us to accurately mimic the conditions and parameters of Roisman's experiment.

Table 4. Roisman experiment parameters [93]

Roisman-exp	
Liquid	water
Solid surface	Stainless steel
Droplet diameter D_0 (mm)	2.5
Advancing contact angle (θ_a)	120°
Receding contact angle (θ_d)	65°
Impact velocity (m/s)	0.16
Weber number	0.88

Table 5. Water and air properties for droplet spreading case

Water properties	**Air properties**

Viscosity $(Pa.s)$	Surface tension $(N.m^{-1})$	Density $(kg.m^{-3})$	Viscosity $(Pa.s)$	Density $(kg.m^{-3}$
0.00874	0.07319	1025.76	0.000018	1.225

The experiment involved a water droplet splashing onto a stainless steel surface. The advancing and receding contact angles were measured to be 120 degrees and 65 degrees, respectively. The velocity of the droplet immediately before making contact with the solid wall was recorded at 0.16 m/s. The computational domain is a cube of 12.5 mm side length (Figure 80). All faces are set as a wall boundary condition. The mesh resolution is fixed at 32 cells per radius.

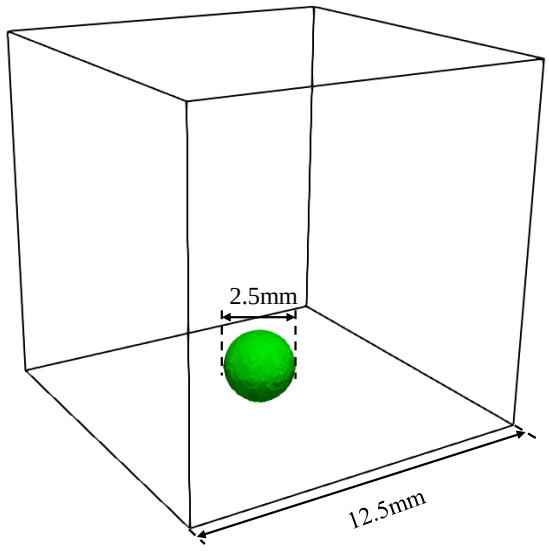

Figure 80. Computational domain for the spreading of droplet case [93]

6.4.1 Effect of curvature method

To illustrate the different between different curvature method, the curvature calculation HF and SVF each integrated with the Kistler dynamic contact angle model are explored. As illustrated in Figure 81a) ,it appears that both the SVF Kistler and HF Kistler models initially overestimate the droplet spreading factor compared to the experimental data. However, in Figure 81a), as time progresses, the spreading factor in the HF Kistler model starts to detach from the SVF Kistler model at time = 7.5 ms. Then, the spreading factor of the HF Kistler model is closer to the experimental data, while the SVF Kistler model continues to overestimate the experiment data throughout the entire time period.

On the other hand, Figure 79b illustrates that the HF Kistler model is more adept at capturing the experimentally observed changes in height ratio compared to the SVF Kistler model. Overall, the figure shows droplet oscillations from 0 to 25ms. From time=0 to time=7ms, the droplet's height decreases, albeit with a minor rebound at around 5ms. During this phase, the HF Kistler model closely aligns with experimental results, whereas the SVF Kistler model overestimates the height. From 7.5ms and 13m, after the droplet reaches its lowest height, the height starts to increase again, reaching a ratio of H/H_0=0.765. Here again, the HF Kistler model exhibits strong agreement with experimental data, while the SVF Kistler model underestimates the height.

Beyond this point, the droplet continues to oscillate. The HF Kistler model remains consistent with the experimental data up to around 23ms, after which it begins to diverge. In contrast, the SVF Kistler model starts showing significant discrepancies with the experimental data from that moment onward.

In conclusion, the HF method's ability to represent the experimental data with greater accuracy, while the SVF method initially overestimates and then underestimates the phenomenon.

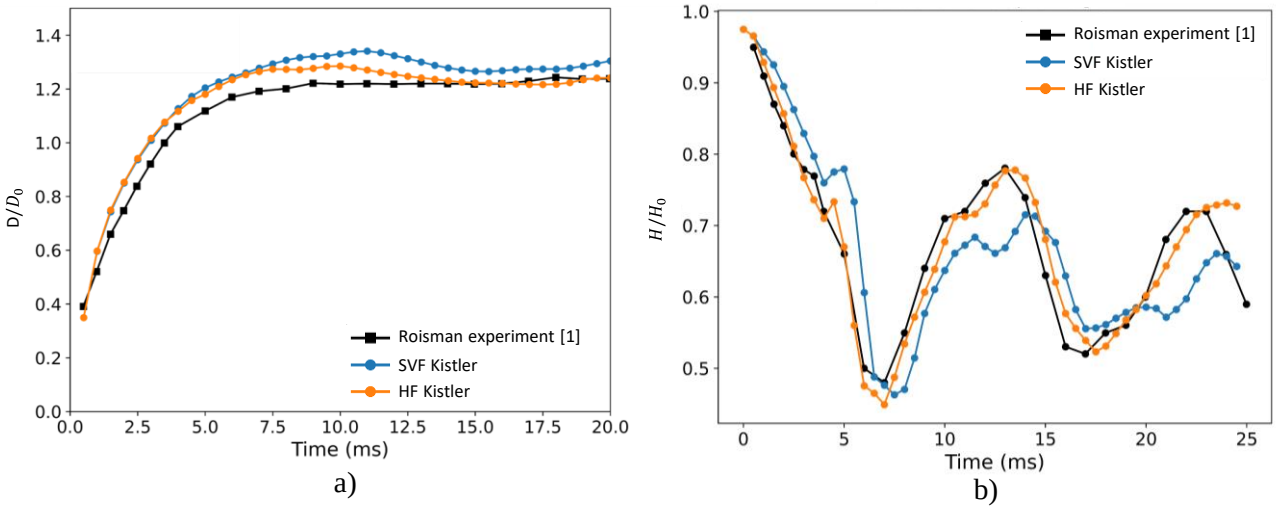

Figure 81. SVF Kistler and HF Kistler are compared with numerical and experimental results of Roisman [1]: a) The evolution of the spreading factor; b) The evolution of the droplet height.

Figure 82 show the comparison between our numerical results and the experimental images from Roisman et al. [93]. Overall, the numerical simulation agrees well with the experiment data. However, some minor differences in shape are observed. This can be explained by the fact that, in the experiments, the droplet shape is not a perfect sphere when it contacts the solid surface. Indeed, Roisman [93] reported that due to the initial oscillations during droplet generation, it is difficult to perfectly control the initial shape of the droplet.

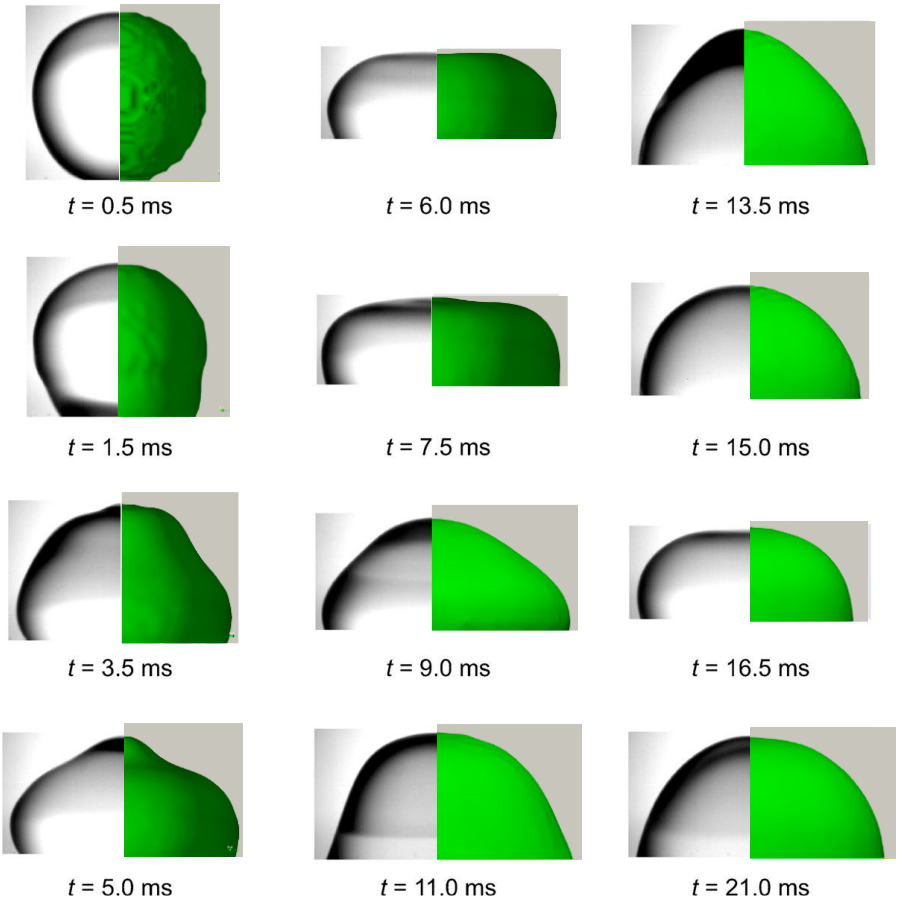

Figure 82. Numerical results of the spreading droplet obtained with HF and Cox's models (right half, green) and experimental results [93] (left half). The contour is the C = 0.5 iso-surface

6.4.2 Effect of different dynamic contact angle model

As discussed in Section 2.3, there are several dynamic contact angle models. During the development phase, two different models, Kistler and Cox, are implemented. Therefore, in this section, these two models are compared to observe their behavior. Figure 83a) illustrates the time evolution of the spreading factor defined as the ratio between the wetted diameter D and the initial wetted diameter D_0. Both dynamic contact angle models predict the evolution of the spreading droplet well, although the droplet diameter is slightly over predicted by the numerical simulations, including the Roisman CFD results. Both models behave similarly during the transient phase. However, a divergence becomes apparent at around the 7.5-second mark. From that point onward, the Cox model tends to continue overestimate the radius, while the Kistler model forecasts a lower final spreading factor that aligns more closely with the experimental data.

Figure 83b) shows the time evolution of the dimensionless droplet height defined as the ratio between the droplet height H and the initial droplet height H_0. Both the Kistler and Cox dynamic contact angle

models effectively replicate the experimental data and accurately predict the droplet's oscillation frequency. During the initial descent phase from 0 to 7ms, the CFD results of the current study align more closely with experimental observations than do Roisman's CFD findings. From 7 to 17ms, both the current study's CFD outcomes and those of Roisman track well with the experimental data, although the HF-Cox method slightly underestimates the height between 9 to 14ms. Beyond 1 ms, Roisman's CFD results fail to follow the experimental trend, while the Kistler model remains accurate up to 22ms and the Cox model up to 20ms. After the 22ms mark, none of the CFD models can faithfully reproduce the experimental data.

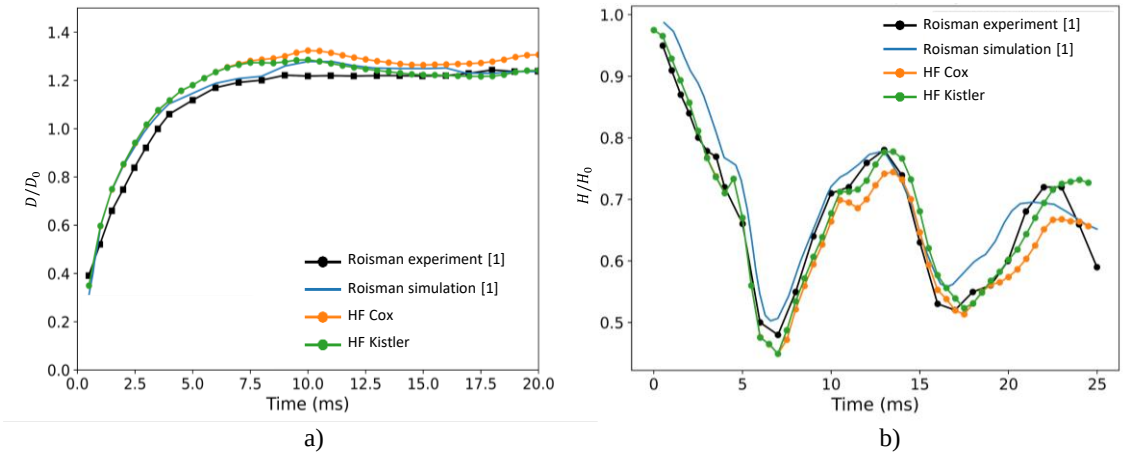

a) b)

Figure 83. Two different dynamic contact angle models are compared with numerical and experimental results of Roisman [93]: a) The evolution of the spreading factor; b) The evolution of the droplet height

6.5 Conclusion

In this chapter, several tests were carried out to valid the new development (well-balanced PISO algorithm, Height Function method, dynamic contact angle models and the combination of these new developments). Initially, a two-dimensional stationary droplet was chosen to test the effects of the HF and well-balanced method. The results indicated that with these new implementations, errors caused by imbalances in the code are dramatically reduced, and the accuracy of the interface location has significantly improved. The spreading of a droplet, driven by the contact line and water droplet spreading, was tested to observe the effects of the new implementation of the dynamic contact angle. This showed that the dynamic contact angle significantly enhances the output of two-phase flow CFD, which is then compared with theoretical models as well as with experiments.

Chapter 7

Transient film flow over complex surfaces

How can new developments be applied to simulate corrugated channels? In this section, film flow over flat and corrugated surfaces will be simulated to understand the hydrodynamics of film flow over complex corrugated dry surfaces.

7.1 Introduction

In Chapter 4, the research focused on film flow over a pre-wet surface, often observed in oil injection flows for electric motor end windings. However, this does not represent all scenarios encountered in practical applications. Specifically, when oil injection begins, the motor's end winding usually displays a dry and intricate surface. As a result, this chapter delves into the simulation of film flow on these complex dry surfaces. Simulating film flow on a dry surface demands special attention due to the effects of the contact line, which isn't a concern with pre-wetted surfaces. To address this, methodologies from Chapters 5 and 6 have been incorporated to accurately depict film flow over dry areas. The chosen model employs a two-dimensional computational domain as the basis to probe the effects of surface curvature calculation methods, equilibrium contact angles, and varying Reynolds numbers. The objective is to study the film's behavior on intricate surfaces under diverse setup parameters, which will enrich the understanding of film flow on the corrugated surfaces of motor end windings.

7.2 Numerical setup

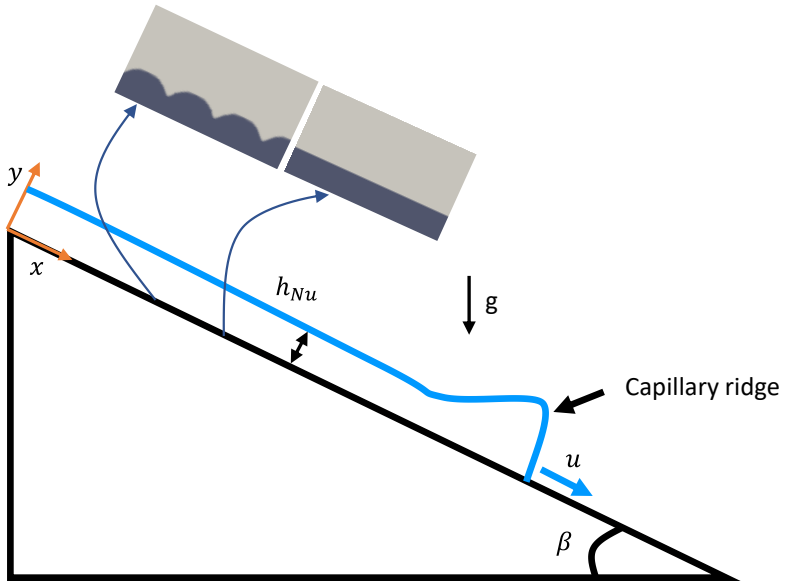

Figure 84. Representation of a film injected at a constant uniform rate onto a plane inclined at an angle β.

Two distinct wall configurations are studied: a flat wall and a wall with a corrugated pattern (Figure 84). The motion of the liquid film is affected by a combination of factors, including the inlet mass flow rate and gravitational forces. Key features of the film flow, such as the shape of the fluid interface and the characteristics of the capillary ridge, are influenced by forces like gravity, viscous forces, and surface tension. The thickness of the liquid film is theoretically calculated using Nusselt film theory and compared with the numerical results.

7.2.1 Numerical domain and setup

The reference flat wall domain configuration is based on the research of Lallement and experiences of Johnson [96,97] with the objective to do 3D simulation. However, in this scope of study, only 2D simulation tests was conducted as it requires much less simulation time. It corresponds to a film injected at a constant mass flow rate with Re=0.52 onto an inclined surface at an angle of 27.9°.

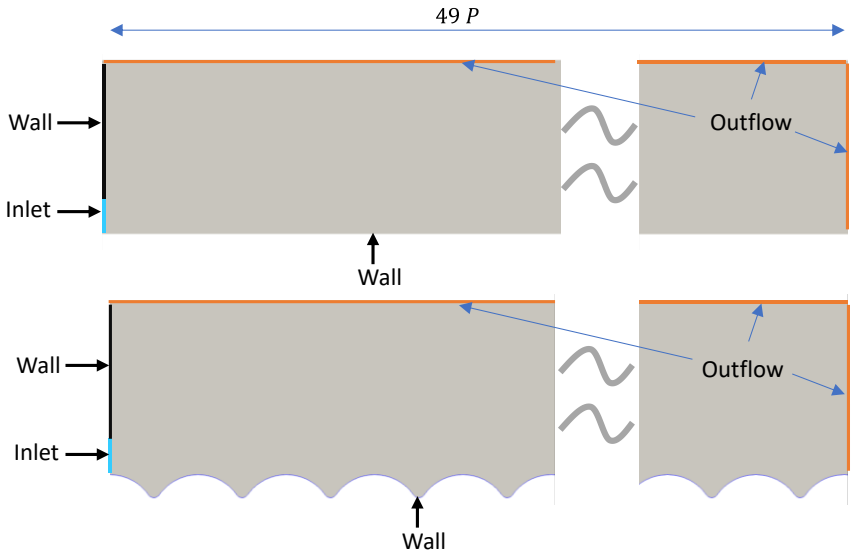

Figure 85. Computational domain and boundary conditions of dry channel

The corrugated pattern is similar to what is described in Chapter 3. The initial film height at the injection point is set to be equal to the thickness of the film calculated by Nusselt theory (Figure 85). The liquid properties are a mixture of water/glycerol at ambient temperature, as follows:

Table 6. Liquid properties at ambient temperature

Liquid	$\rho(kg.m^{-3})$	$v(m^2.s^{-1})$	$\mu(N.m)$	$\theta_s\ (contact\ angle)$
Water/glycerol	1210	6.9×10^{-5}	0.066	38°

The mass flow rate can be calculated based on Re; in the reference case with Re=0.52, the mass flow rate is:

$$\dot{m} = \rho \upsilon Re = 4.341 \times 10^{-2} kg.s^{-1}.m^{-1} \quad (107)$$

The thickness of the film, calculated by Nusselt theory, is:

$$\delta_{Nu} = \left(\frac{3\upsilon\dot{m}}{g\rho \sin(\beta)}\right)^{\frac{1}{3}} = 1.174 \times 10^{-3} \quad (108)$$

7.3 Mesh study

7.3.1 Mesh Strategy

In order to decrease the number of mesh to get results faster, the AMR was used. To confirm the reliableility of AMR, the position of interface after 1s simulation was compared (Figure 87). The mesh strategy consists in activating AMR in the liquid only and at the interface to compare with regular mesh (Figure 86). The mesh size varies from 100μm to 25 μm.

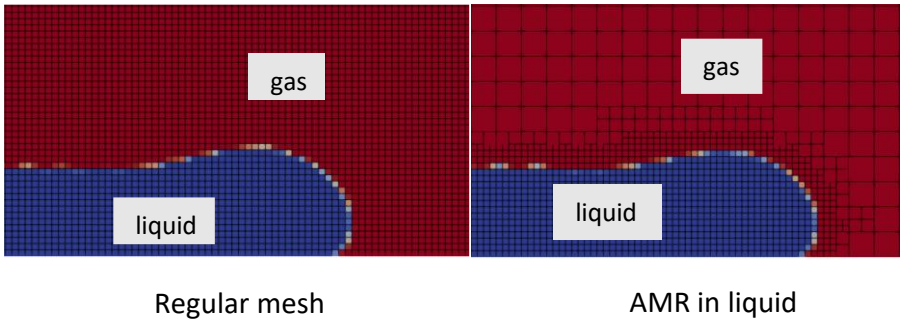

Figure 86. Comparing regular mesh vs AMR mesh

By comparing the interface at the same time, it can be observed that the interface in both meshes are almost identical. Hence, AMR does not affect the simulation results, while it reduces the mesh size by roughly 87% and decreases simulation time by 85%. This AMR configuration is used for subsequent simulations in this chapter.

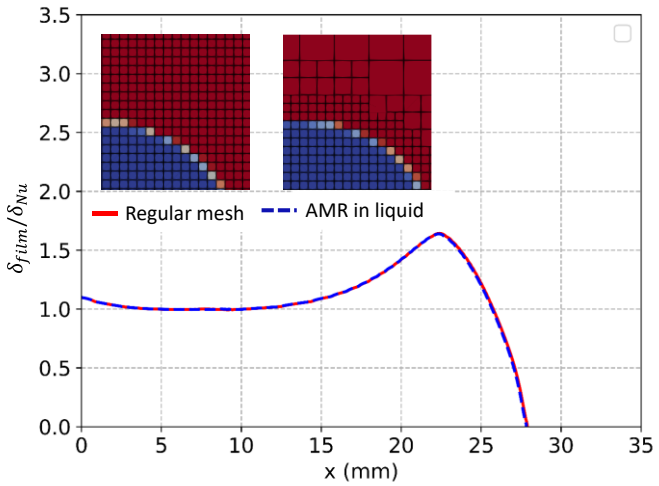

Figure 87. Comparing the interface position and shapre at the front of the film for the regular mesh and AMR in liquid, Δx=50μm, t=1s, $\theta_s = 38°$, Re=0.52

7.3.2 Mesh convergence study

In this section, a mesh study is launched to test and choose the best mesh configuration for the simulation, to investigate the sensitivity of transient film behavior to the grid. As previously mentioned (section 6.3.2), the simulation of the static contact angle model was first tested with mesh sizes ranging from $25\mu m$ to $100\mu m$ and then compared to Lallement's results (Figure 88 a.). The results clearly indicate that there is no mesh convergence, as explained in section 6.3.2. As the mesh size decreases, the implicit slip length also decreases, resulting in the contact line lagging behind compared to the case with a larger mesh. However, at a mesh size of $\Delta x = 50\mu m$, the results seem to align with Lallement's findings. In all mesh cases, after a brief transition at the inlet, the film thickness equals δ_{Nu}. Subsequently, the film thickness increases to form a capillary ridge due to the effects of the capillary number, contact angle, gravity, and liquid properties.

To observe the effect of dynamic contact angle on mesh refinement, the DCA Kistler model was applied (Figure 88 b). Overall, after the transition period at the inlet, the film thickness decreases back to the height of Nu theory when Δx is greater than $50\mu m$. However, at the mesh $\Delta x = 25\mu m$, the thickness, post-transition, does not revert back to δ_{Nu}. This is because at a denser mesh, the smaller implicit slip length causes the contact line to move more slowly than at a coarser mesh. Therefore, at 1s, it hasn't fully developed, preventing the film thickness from decreasing back to the theoretical film as observed in other cases.

In conclusion, among the three different meshes, it is evident that, as expected, there is no mesh convergence of the contact line for both SCA and DCA. However, it's clear that the film thickness equals the theoretical film in the fully developed section of the film.

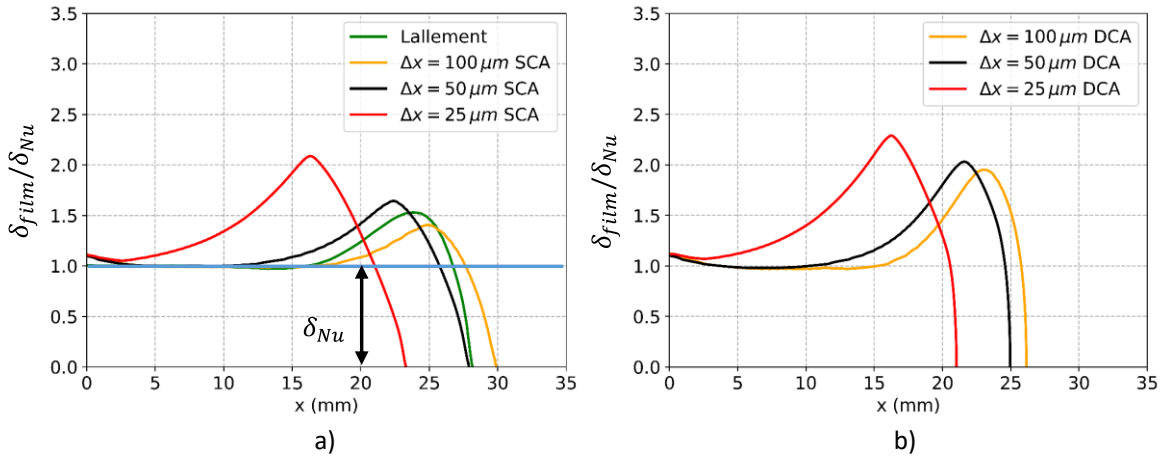

Figure 88. Mesh convergence test with a static and dynamic contact angle model at $t = 1s$, $\theta_s = 38°$, Re=0.52

The film initially wets the surface until it reaches the end of the computational domain. At this stage, the simulation surface is completely wet, and it will be checked for wall shear stress. As observation in Figure 89 a). It represents the shear stress of a fluid in relation to the wall boundary layer, extending from 0 to 35 mm. This is illustrated across four distinct mesh sizes, ranging from 12.5 micrometers to 100 micrometers. In this figure, there are four lines, with each line corresponding to a specific mesh size. All four lines follow a similar trend. Initially, the wall shear stress is at its highest, reaching 40 N/m^2. This then drastically decreases to approximately 5.5 N/m^2, experiences a slight increase, and eventually levels off. Due to the similarity in these trends, it becomes challenging to discern the nuances between the four different mesh sizes.

This is where Figure 89 b) comes into play. Figure 89 b) depicts the average value of the shear stress within a specific segment, specifically from 25 to 35 mm, for each of the four mesh sizes. By zooming into this range, the differences between the mesh sizes become more apparent. The average value for the 100 μm mesh is 7%, which gradually decreases to 6.6% for the smallest mesh size. The difference between them isn't vast; especially when comparing the 50 μm with the 12.5 μm, the difference is a mere 3%. This suggests that once the fluid has flowed past, a 50 μm is sufficient to capture the hydrodynamic phenomena of this type of flat wall.

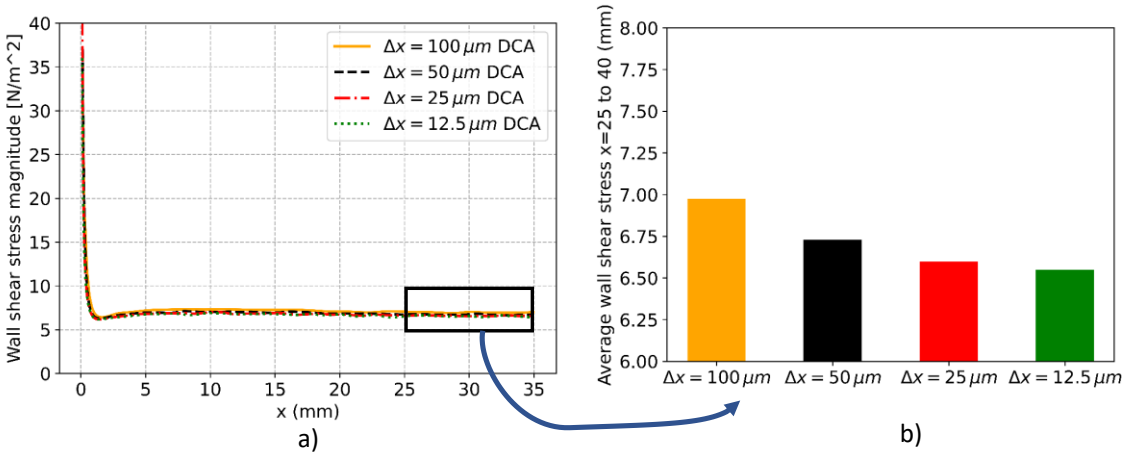

Figure 89. Wall shear stress magnitude at Re=0.52; a) along channel b) average from 25 to 35 (mm) when the channel already fully wetted

In practical scenarios, computational domains are rarely flat. Instead, they tend to be intricate, as exemplified by the corrugated surfaces discussed in this chapter. Meshing such domains with an aligned-wall mesh becomes infeasible due to their complexity. This challenge necessitates the adoption of alternative mesh structures, such as the cut-cell mesh, which is showed in Figure 90. This mesh type is versatile, capable of accommodating nearly any surface, regardless of its intricacy. However, its efficacy needs to be verified before extensive application.

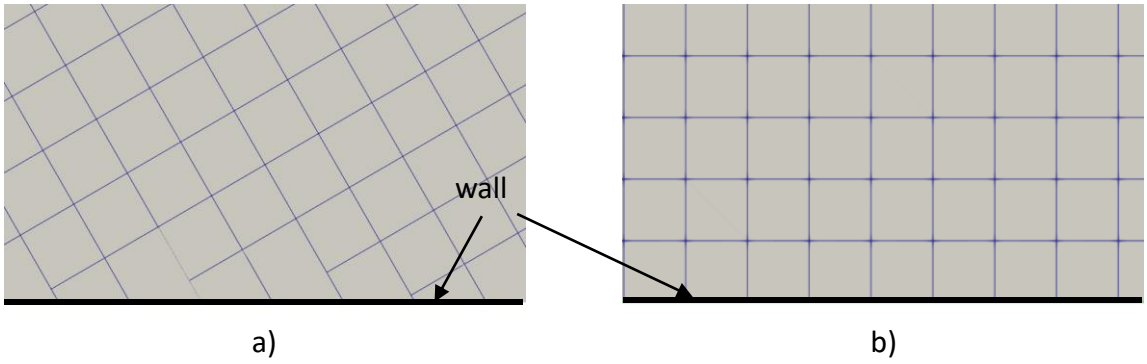

Figure 90. a) Cut-cell mesh; b) Aligned-wall mesh

Figure 91 offers a comparative analysis of the interface profiles of cut-cell mesh against the aligned-wall mesh at a specific instance (t=1s), considering both static (SCA) and dynamic contact angles (DCA) using the SVF method. Across all four simulations, a brief transmission section is evident where the film thickness deviates from the theoretical thickness, δ_{Nu}. This is followed by a phase where the film thickness aligns with δ_{Nu}. Notably, all four scenarios exhibit a Capillary ridge. However, a significant distinction emerges within the SCA model: the cut-cell mesh in the SCA

context appears to have a quicker sliding motion compared to its aligned-wall counterpart. In contrast, when examining dynamic contact angles, the discrepancies between the cut-cell and aligned-wall methods are minimal.

Drawing from these observations in Figure 91, it's clear that when used with the DCA, the influence of the cut-cell mesh structure on simulation results is relatively minor. However, its effects become significantly more discernible when the cut-cell mesh operates in conjunction with the SCA.

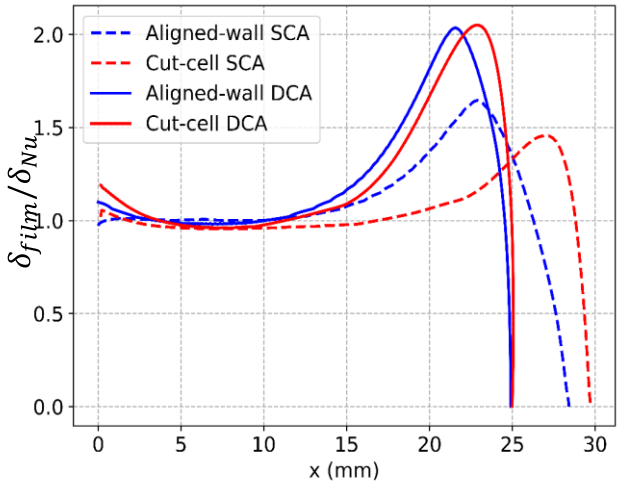

Figure 91. Interface profile at $1s$ with SVF method, $\Delta x = 50\mu m$, $\theta_s = 38°$, Re=0.52. Comparing SCA and DCA with different mesh structure

Based on these simulations, the cut-cell method is applied to simulated corrugated wall . A similar test was conducted as with the flat channel (Figure 89), where two graphs were plotted. One is a line chart of four mesh sizes ranging from 100 μm to 25 μm, and the other is a bar chart with four columns, each representing the average wall shear stress of the line segment from 25 to 30 mm.

In Figure 92 a), the line chart depicts the following: initially, much like a flat channel, the wall shear stress in the corrugated channel reaches a peak of 40 N/m^2. This value then experiences a sharp decline within the first 1 mm of the channel. However, due to the influence of the corrugated channel, the velocity in the boundary layer near the wall varies largely depending on the wall pattern. The wall shear stress has a consistent fluctuation following the pattern of the corrugated wall. On the other hand, Figure 92 b) depicts the average wall shear stress between 25 to 35 mm, where the wall shear stress exhibits stable fluctuations.

The results suggest that in this corrugated form, the mesh's impact is greater than in a flat channel. For instance, the difference in mesh between 100 μm and 12.5 μm in this case reaches up to 33%, while in a flat channel, it's only 6%. Interestingly, when the mesh is reduced to 50 μm, the difference

of wall shear stress in corrugated channel is only 8%, and it drops to 6% for a 25 μm.. In conclusion, for this type of surface, a mesh size of at least 50 μm is sufficient to capture most of the liquid's phenomena. Moreover, this coarseness ensures that the contact line can move smoothly.

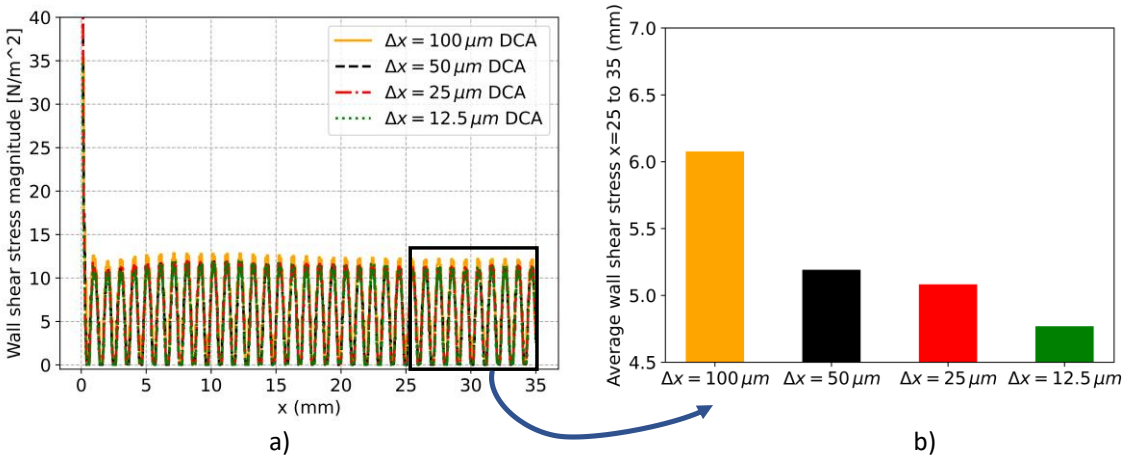

Figure 92. Wall shear stress magnitude at Re=0.52 a) along channel b) average from 25 to 35 (mm) when the channel already fully wetted

Upon examination of the mesh and evaluation of the implicit slip length, it becomes evident that selecting the mesh size $\Delta x = 50 \mu m$ for the simulations strikes a delicate balance. This choice is based on tests conducted with both SCA and DCA models, alongside comparisons with Lallement's findings. Specifically, a mesh size of $\Delta x = 50 \mu m$ is not only sufficiently fine to accurately capture the interface but also large enough to permit the movement of the contact line interface. This size ensures ample implicit slip-length for the liquid to glide smoothly, while simultaneously being fine-tuned to yield dependable results. From now on, the mesh with $\Delta x = 50 \mu m$ will be used for both flat and corrugated surfaces for simulating in this chapter.

7.4 Effect of curvature calculation

Once the appropriate mesh was finalized, the next step involved examining the influence of different curvature methods. In this segment, the SVF method was compared against the HF method, with both results benchmarked against those of Lallement. Figure 93a) and b) showcase the comparison of these curvature methods, using the SCA and DCA models, respectively, at a delta of 50 μm.

For Figure 93a), at the 1-second mark and in comparison with Lallement's results, both the HF and SVF methods align closely, especially in the contact line location. However, the HF method's

interface profile seems to adhere more accurately to the trend observed with Lallement's case, even at the capillary ridge. In contrast, the SVF method demonstrates slight discrepancies, particularly noticeable at the capillary ridge. Beyond the capillary ridge, both methods yield results in line with Nusselt's theoretical calculations, indicating a film thickness ratio equal to 1.

Figure 93b) paints a similar picture of the interfaces of both the SVF and HF methods. However, this time, instead of the SCA, the DCA is employed. Notably, there's no comparison with Lallement's data here, as Lallement's results pertain solely to SCA. This line chart, with separate lines representing HF and SVF, indicates that when the dynamic contact angle is employed, a greater distance, specifically around 5mm as opposed to 2.5mm for SVF, is needed for the liquid to transition to the Nusselt film state, where the film thickness matches Nusselt theory. This is due to the HF is more sensitive to the wall contact angle and potentially change setup can help. Due to the larger contact angle in DCA model, which results in greater adhesion force at contact line and consequently slows down the fluid motion. For instance, when using the HF method, the contact line position for SCA is 28mm (Figure 93a), while it's only 21mm (Figure 93b) for DCA. A similar trend is observed with the SVF method. Moreover, due to the increased resistance, the magnitude and height of the capillary ridge for DCA are greater; the peak of the DCA's capillary ridge is roughly twice that of the Nusselt film thickness theory, whereas the SCA's is around 1.6 times.

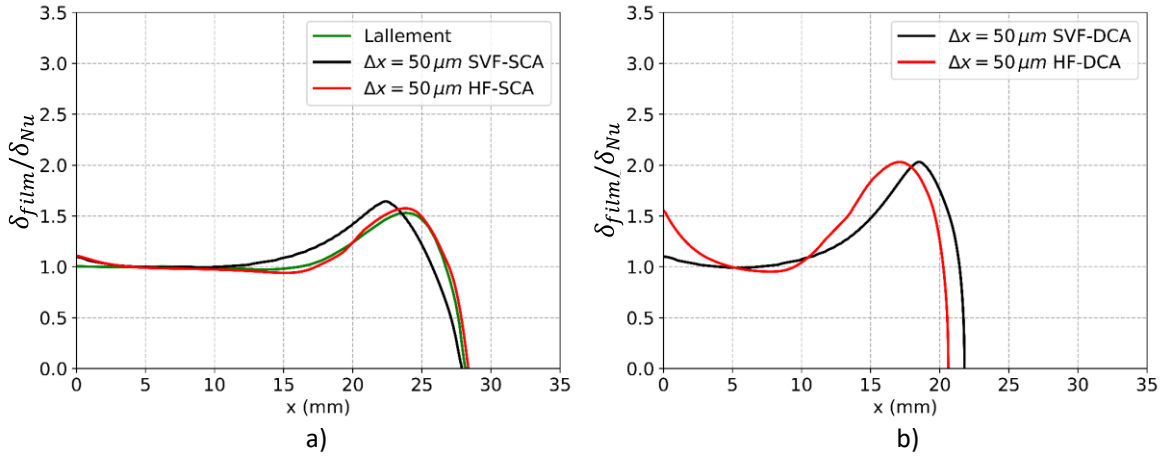

Figure 93. Interface profile comparison between HF and SVF at $t = 1s$, $\theta_s = 38°$, Re=0.52; a) SCA; b) DCA

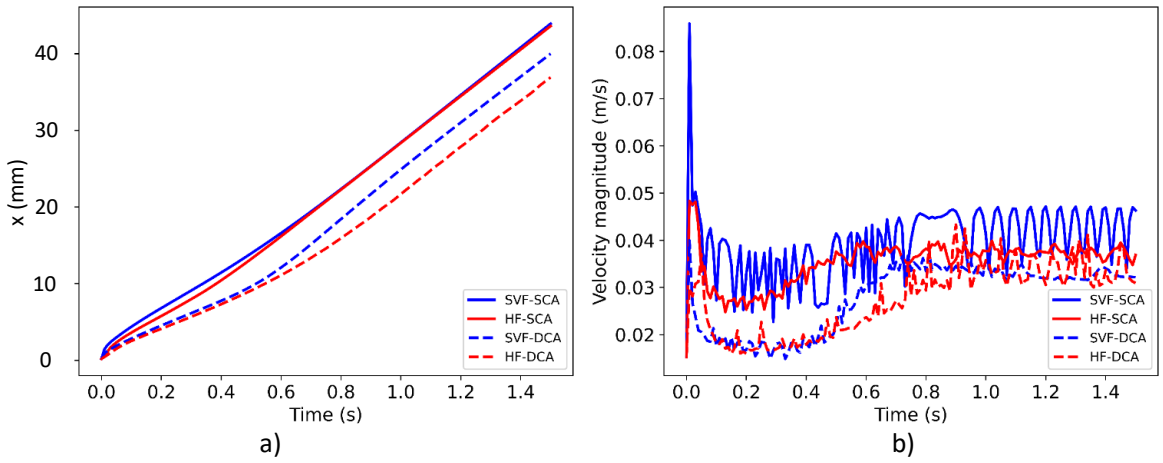

Figure 94. Numerical results with $\theta_s = 38°$, Re=0.52; a) Time-dependent contact line posision b) Time-dependent contact line velocity magnitude

While the interface profile allows us to observe the differences between DCA and SCA, a deeper analysis is necessary to understand the underlying reasons for their divergence. Figure 94a) assists in illustrating these differences.

Figure 94a) plots the position of the interface over time for four distinct scenarios, accounting for the variations in both curvature methods (SVF and HF) and contact angle models (SCA and DCA). Similarly, Figure 94b) illustrates the velocity of the contact line over time for these four cases.

From Figure 94a), it's evident that for cases employing the SCA model, both HF and SVF methods showcase a relatively consistent position of the contact line over time, increasing linearly. There's a minor deviation between 0 to 0.6 seconds, where the HF method's contact line lags slightly behind, but it eventually aligns closely with that of the SVF. In contrast, with the DCA model, both HF and SVF methods display similar contact line positions until around 0.6 seconds. After this point, the contact line's position in the HF method trails significantly, by about 0.05mm compared to SVF.

Figure 94b), as mentioned, describes the velocity of the contact line (measured as half the boundary cell velocity). On average, the velocities in the SCA model scenarios are greater than those in the DCA model scenarios. This observation is logical: the SCA model holds the contact line at a fixed angle of 38°, which is smaller than the DCA model's contact angle. A smaller angle implies less resistance, leading to faster velocities. However, the phenomenon of "spurious currents" (as detailed in Chapter 6) introduces velocity instability in the SVF-SCA scenario compared to the HF-SCA.

In general, at the onset, as the liquid is introduced into the channel, its velocity peaks sharply, and then immediately slows down. From this point, the average velocities of all four scenarios decline, reaching their minimum values at around 0.3 seconds. They then gradually increase until about 0.8

seconds, after which they stabilize. For the DCA scenarios, the velocity variations are less pronounced, and the average velocities are generally slower than in the SCA scenarios, as mentioned earlier.

In conclusion, the distinction between the SVF and HF methods significantly influences the behavior of the contact line, both regarding its position and velocity. The HF method hasdemonstrated a superior ability to capture the interface as . However, a limitation of the HF method is that it currently operates only on a single processor which is impossible to run a large scale simulation, but improvements are anticipated in future endeavors. As a result, the following chapter will employ the SVF method combined with DCA for simulations.

7.5 Comparison of transient film flow on flat and corrugated surfaces

The evolution of liquid film flow over two distinct surfaces, flat and corrugated, was studied (Figure 95). Observations of the liquid interface were recorded at three time intervals: 0.5s, 1s, and 1.5s.

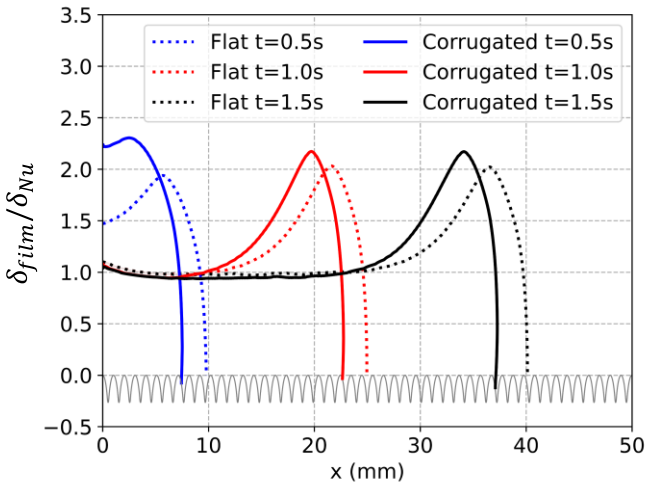

Figure 95. Interface profile comparison between flat and corrugated surface at 0.5s, 1.0s and 1.5s with $\theta_s = 38°$, Re=0.52

At the 0.5-second, the film interface on the corrugated surface was significantly thicker compared to that on the flat surface. This difference can be linked to the initial effects: the corrugations on the surface act as obstructions to the free movement of the liquid, resulting in a more substantial buildup. However, as the time extended to 1s and 1.5s, the influence of these initial effects diminished. Consequently, the film interface on both the flat and corrugated surfaces started to follow to the Nusselt film state more closely, with the theoretical film thicknesses aligning and the film thickness in the corrugated case was slightly thinner than in the flat case. Another observation is the film on the

flat surface traveled faster than that on the corrugated surface. This is illustrated in Figure 96 a), which depicts the changing contact line positions over time. For the flat surface, the contact line's position advances consistently. Initially, as the liquid is injected to the dry surface, the contact line advances slowly. This is because the liquid is still forming the capillary ridge. However, by 0.6s, it starts advancing fast, aligning with the contact line velocity depicted in Figure 96 b). On the other hand, the contact line position on the corrugated surface follows a distinct pattern due to its pattern. Particularly, from 0.3 to 0.5s, the position remains almost static. This stagnation occurs because the corrugated surface prevents the liquid's movement in the x direction, causing it to accumulate in the y direction. By 0.5s, when the capillary ridge is big enough and the wall's cohesive force of the wall acting on liquid longer hold the contact line back, it begins to move again. However, its progression remains slower compared to that on the flat surface.

As shown in Figure 96 b), there's a significant fluctuation in contact line velocity magnitude of corrugated case. This fluctuation in the contact line are largely influenced by the corrugated pattern. Specifically, the liquid tends to move slower when the flow direction and the wall's normal are misaligned, and quicker when both directions are aligned.

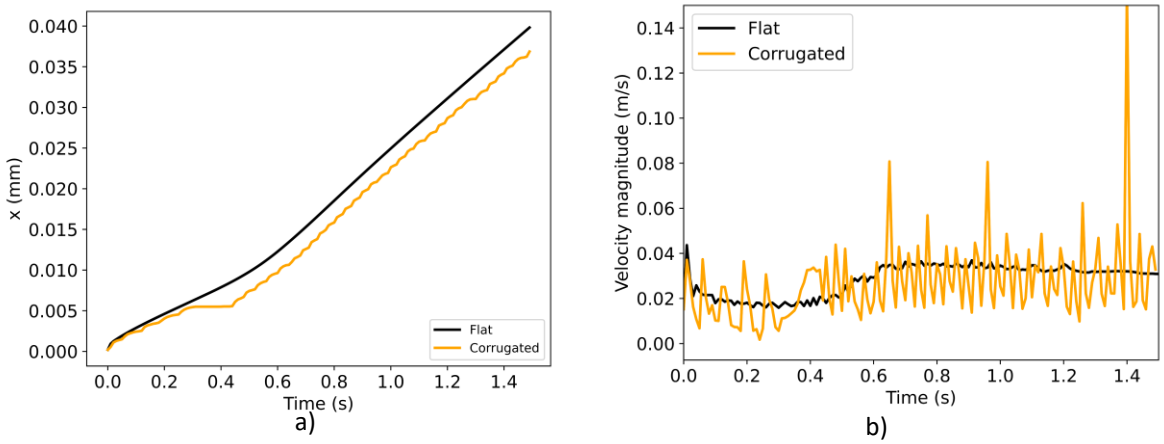

Figure 96. Comparison between flat and corrugated surface at 0.5s, 1.0s and 1.5s with $\theta_s = 38°$, Re=0.52; a) Time-dependent contact line posision b) Time-dependent contact line velocity magnitude

7.6 Effect of equilibrium contact angle

In electric motor applications where liquid coolants are deployed, a myriad of materials such as copper, steel, and wiring are encountered. As a consequence, the equilibrium contact angle is not always a constant figure. This value can fluctuate based on the surface characteristics of the material as well as the type of coolant used.

In this section, four distinct equilibrium contact angles: 38°, 60°, 90°, and 120° are investigated. These values are emblematic of two common surface categories: hydrophilic and hydrophobic.

Figures 95a and 95b depict the interface profile at 1 second for both flat and corrugated surfaces, respectively, when the SVF-DCA method is employed.

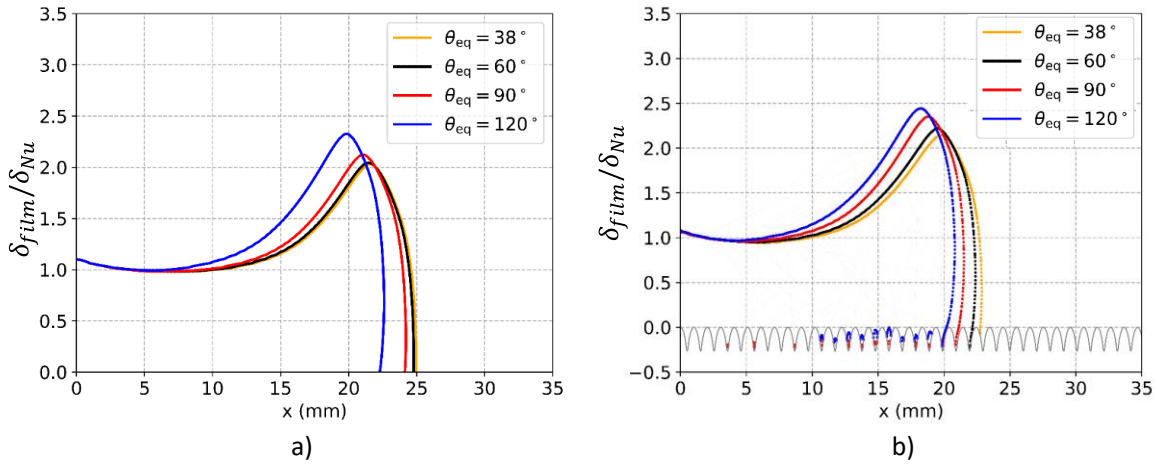

Figure 97. Interface profile comparison of four distinct equilibrium contact angles: 38°, 60°, 90°, and 120° at $t = 1s$, Re=0.52; a) SVF-DCA Flat channel; b) SVF-DCA Corrugated channel

In Figure 97a), all four cases display a comparable trend. Yet, as the equilibrium contact angle grows, the dynamic contact angle increase, as explained to in section 5.4. This change affects the capillary ridge. A rise in the "actual" contact angle exerts a stronger adhesion force which is resistance against the forward movement of the contact line. Consequently, the peak of the capillary ridge moves from being twice the theoretical film thickness to 2.2 times its value.

Figure 97b), also illustrates the interface profile at 1 second for the corrugated channel. Analogous Figure 97a), an increasing equilibrium contact angle slows down the contact line's motion, and the capillary ridge's peak also rises. A noteworthy distinction is the increased adhesion force experienced by the liquid flowing through the corrugated channel compared to the flat one. For instance, with an equilibrium contact angle of 60°, the liquid advances 25 mm in the flat channel at 1 second but only manages 22 mm in the corrugated channel. Furthermore, the highest point of the capillary ridge in the corrugated channel generally exceeds that in the flat channel. However, a peculiar observation in the corrugated channel is the emergence of air bubbles when the contact angle is at 90° and 120°. This suggests that with larger contact angles, the liquid fails to wet the entire corrugated surface, leading to this phenomenon.

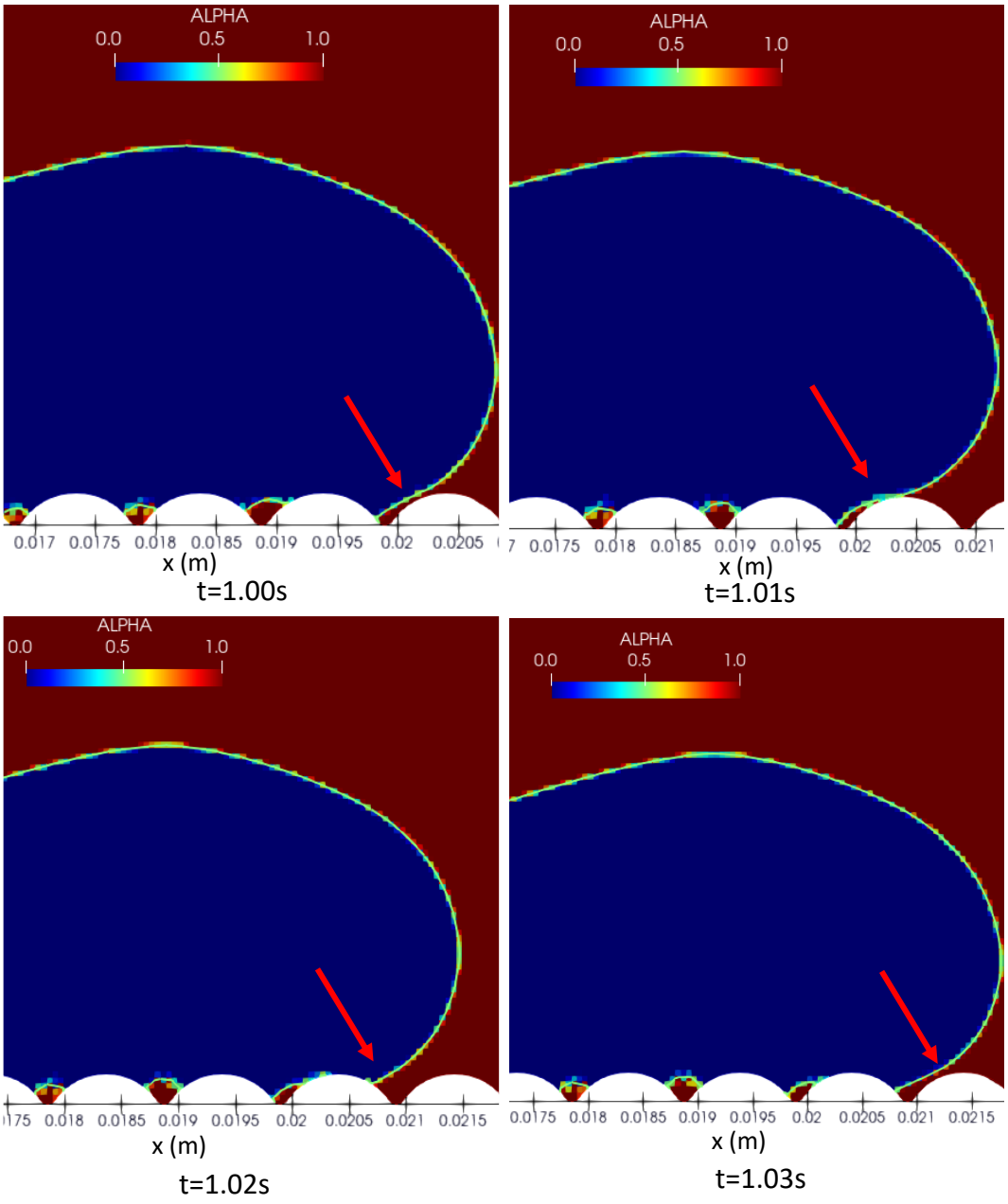

Figure 98. Close-up observation of the interface passing through a corrugated cycle near the wall. Re=0.52, $\theta_s = 120°$ at $t = 1.00, 1.01, 1.02, 1.03$, SVF-DCA

Further details can be observed in Figure 98, which presents the evolution of the contact line passing over a corrugated cycle at Re=0.52 when an equilibrium contact angle of 120 is applied. Due to the high contact angle and the pattern of the corrugation, the contact line touches the front side of the corrugated wall before it can wet the entire corrugated surface. This phenomenon results in bubbles being trapped within the corrugated valley.

7.7 Effect of Reynold number

In electric machines employing the direct cooling method, liquid films are anticipated to have higher Reynolds numbers. Thus, the study extended beyond the effects of different contact angles, as the Reynolds number also exhibited considerable variations. While a previous section studied the effects of different contact angles, this section focuses on the variations and consequences of changing Reynolds numbers.

The range of Reynolds numbers examined extended from a very low value of approximately 0.52 to a relatively high value of 30 (for film flow). To elucidate the effects of different Reynolds numbers, the capture time was normalized with respect to the Reynolds number, and the film thickness was compared to the theoretical film thickness as calculated by the Nusselt theory.

For time normalization, division by Re was undertaken. Regarding normalized film thickness, as detailed in Table 7, varying Reynolds numbers produce different theoretical film thicknesses. As a result, film thickness was normalized by dividing it by the theoretical film thickness associated with each distinct Reynolds number, notably for the values of 0.52, 5, and 30.

Table 7. Dependency of δ_{Nu} on Re number base on (107) and (108)

Re	0.52	5	30	76	100
δ_{Nu}	0.001174	0.002496	0.004536	0.006184	0.006776

Figure 99a) depicts the normalized interface profile at (Time/Re=0.52). It's evident that the shape of the capillary ridge deviates markedly with changing Reynolds numbers. The maximum height of the capillary ridge diminishes as the Reynolds number ascends. For instance, at Re = 0.52, the ratio of film thickness to theoretical film thickness is 2, while at Re = 30, this value reduces to approximately 1.3. Furthermore, at the same normalized time (Time/Re=0.52) for different corresponding Reynolds numbers, the liquid travels further with the highest Reynolds number. Moreover, at the highest Reynolds number, the actual velocity of the contact line is also proportionally faster and based, as velocity increases, the actual contact angle also surges, leading to the emergence of air bubbles in the flow. This phenomenon was not observed at Reynolds numbers of 0.52 or 5. This is because at higher Re numbers, there's a tendency for a greater contact line velocity which led to higher contact angle as described in section 2.3, causing the surface to become hydrophobic.

As a result, the interface beads up, and with high velocity, pockets of air become trapped between the wall and the liquid.

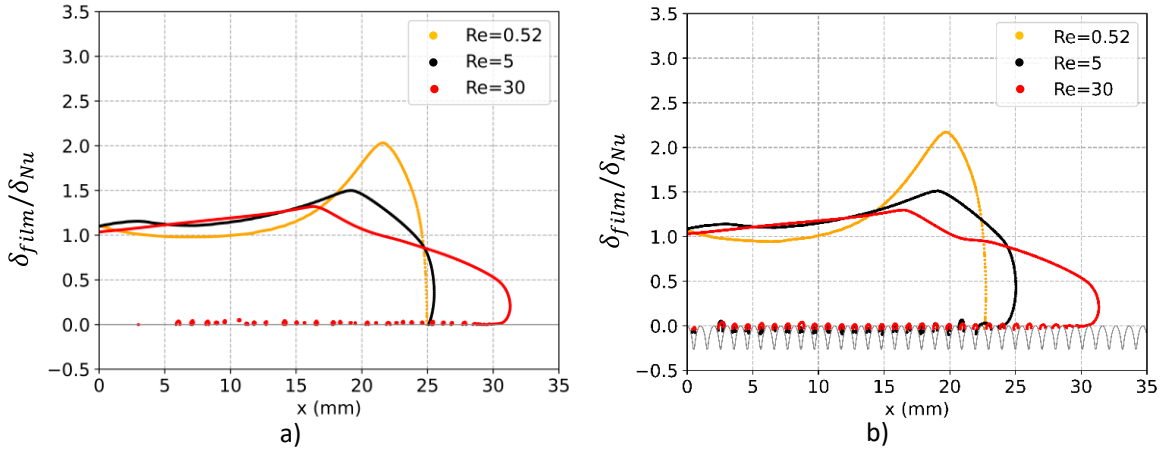

Figure 99. Interface profile for three different Reynolds numbers: 0.52, 5, and 30 at normalized time Time/Re = 0.52, $\theta_s = 38°$; a) flat channel b) corrugated channel

Similarly, Figure 99b) highlights the effects of Reynolds number on the corrugated channel. Broadly, the interface shape is akin to the flat channel, where a higher Reynolds number results in a lower max capillary ridge and a position further from the injection point at normalized time Time/Re = 0.52. However, a distinct difference is noted: even at Re = 5, numerous air bubbles emerge as the liquid flows. This occurrence is attributed not only to the larger contact angle but also to the velocity of the contact line. As illustrated in Figure 98, a higher contact angle causes the interface to touch the front side of the corrugation before it can wet the entire corrugated wall. However, when combined with high velocity, this phenomenon becomes more pronounced.

The Reynolds number profoundly impacts the flow characteristics in both flat and corrugated surfaces. While general trends such as reduced capillary ridge height with increased Reynolds numbers are consistent across both channels, certain phenomena, like the appearance of air bubbles at lower Reynolds numbers in corrugated surfaces, indicate the complex of fluid dynamics. When combined with heat transfer, these bubbles act as insulating materials, preventing direct contact between the liquid and solid parts. This leads to a more complex heat transfer analysis. Additionally, the bubbles can alter the hydrodynamics of the liquid flow. When trapped inside the valleys of the corrugated surface, they reduce the area of direct contact between the liquid and the wall, further complicating the hydrodynamic analysis. These problems need to be taken into account carefully to obtain reliable results.

7.8 Conclusion

In this chapter, we first try to simulate 2D film flow over a dry surface between flat and corrugated surfaces using different parameters with the new solver we develop in Chapter 5. It is essential for

3D simulations in future works. The simulation utilized the geometry described in Chapter 4, and the new developments from Chapters 5 and 6, to effectively simulate film flow over a dry surface. As AMR is crucial for two-phase flow simulations, we first tested its effect on the overall results. AMR reduced the simulation time by 85% while maintaining the output quality, equivalent to using a regular mesh with 85% fewer grid cells.

The mesh convergence study showed that, as expected and as described in Chapter 6, there was no mesh convergence with the no-slip boundary condition. However, we found that with a mesh size of $50\mu m$, the results agreed with the Lallement case.

The distinction between the SVF and HF methods greatly affects the behavior of the contact line, both in terms of its position and velocity. The HF method has demonstrated a superior ability to capture the interface with greater accuracy. However, it should be further improved for parallelization.

The equilibrium contact angle plays an important role in determining how liquids move and interact with surfaces, particularly within corrugated surfaces. Bubbles can easy form and get trapped within the wall corrugations. It should be considered that due to the bubble size is influenced by the wall pattern. Future research should explore various types of corrugated surfaces to understand how different wall patterns affect bubble formation.

Reynolds number emerges as a key factor, dictating the fluid's behavior in terms of film thickness and flow progression. Higher Reynolds numbers, while promoting flow progression, can also introduce challenges, such as air bubble formations, especially in corrugated surfaces.

As the number and size of bubbles trapped inside the corrugated wall vary with the Reynolds number and equilibrium contact angle, this can introduce challenges in accurately estimating heat transfer. These issues should be taken into account in future studies.

The simulations in this chapter are dedicated to future work on 3D simulations. The results and procedures found in this chapter can be used to further develop and properly launch simulations. The ultimate goal is to accurately simulate real 3D direct film flow over complex surfaces.

Chapter 8

Conclusion and perspective

8.1 Conclusion

Electric motors gained global interest due to their environmental benefits. As the push for compact, high-power motors grows, so do thermal management challenges. Heat in these motors, resulting from factors like magnetic, Joule, and mechanical losses, increases strain on various engine parts. Specifically, higher currents can lead to significant heat increases from the Joule effect. Compact designs also reduce cooling space. Thus, effective cooling methods are essential for stable and safe operation.

IFP Energies nouvelles, recognizing these demands, has initiated several projects encompassing simulation, design, and experimentation, all with the aim of producing high-efficiency electric motors. This thesis is embedded within the simulation phase, aiming to provide designers with trustworthy data regarding the heat flux of a cooling system that employs direct oil cooling to the end-winding of an electric motor. The goal of this work, as a component of the broader project mentioned above, is to devise a numerical methodology capable of effectively simulating a liquid film flow generated by a jet impinging on the end-windings of an electric motor. Crucially, this solver should integrate a dynamic contact angle model to accurately capture the intricate wettability phenomena present in the winding geometry, where the liquid film progresses.

First, the introduced of electric motors, underlining the critical thermal management challenges posed by compact designs. It emphasizes the importance of efficient heat dissipation, with a focus on oil-based cooling strategies. Then, a detail of physical phenomena of oil flow, or in general two phase flow has been detail, the surface tension and wettability which is the important aspect to able to simulate film flow over complex surface has been indicate. The dynamic contact angle, the angle between contact line and solid wall is explain in physical way as well as the mathematical model that able to represent that physics as present.

The introduction of the numerical method used for two-phase flow is detailed. The Navier-Stokes equation and how it is discretized are presented. The VOF method that we use in this study, along with the details of the PLIC method that allows for accurate tracking of the interface, is also discussed.

After the general study, the main results of this work can be summarized as follows:

- The study of film flow over pre-wet corrugated surface, which is helping to understand the hydrodynamics, the corrugated surface is based on the actually size of electric wise that use in common electric motor. The liquid properties are the automatic transmission fluid. The comprehensive investigation, the hydrodynamics and heat transfer of film flow within corrugated surfaces for Reynolds numbers less than 101.8 and Prandtl numbers

less than 133 were thoroughly examined using VOF method. The primary objective was to gain a deeper understanding of the intricate interactions occurring among flow behavior, surface geometry, and fluid properties in such configurations. The study explored the influence of channel geometry on flow behavior and heat transfer characteristics, taking a systematic approach. A flat channel was used as the reference model, providing detailed insights into heat transfer mechanisms, flow behavior patterns, and enabling the application of Nusselt correlations for comparative purposes. The corrugated channel's geometry was found to induce recirculation zones and create variable flow conditions, leading to a non-uniform thermal boundary layer. While these features may initially seem advantageous, the average heat flux and wall stress values within the studied range of corrugations were found to be lower 10 to 30% than those observed in flat channels. This result suggests that the heat transfer performance of corrugated surfaces is less effective than that of their flat counterparts.

- The development of a new numerical model allows for the reproduction of physical phenomena and reduces the errors in the current CFD software (Convergecfd.com). The well-balanced algorithm for the PISO procedure is applied to two-phase flow using a collocated grid. The well-balanced technique aims to discretize surface tension and pressure gradient simultaneously and at the same location, ensuring they are 'balanced'. This balance is vital for the solver to reduce spurious currents when solving for 2-phase flow. The height function is a method implemented to replace the existing SVF method in CFD code. Its purpose is to better estimate curvature, which significantly contributes to the overall accuracy of calculating surface tension force, thereby reducing unexpected spurious velocities. Subsequently, the dynamic contact angle is implemented to bridge the gap concerning surface tension force at the wall. The ultimate goal is to represent (as described in Chapter 2) the physical forces between the liquid-gas and solid surfaces at the contact line. To validate the new developments in the ConvergeCFD software, several tests were carried out on the well-balanced PISO algorithm, Height Function method, dynamic contact angle models, and the combination of these new developments. Initially, a two-dimensional stationary droplet was chosen to test the effects of the HF and well-balanced method. The results indicated that with these new implementations, errors caused by imbalances in the code are dramatically reduced, and the accuracy of the interface location has significantly improved. The spreading of a droplet, driven by the contact line and water droplet spreading, was tested to observe the effects of the new implementation of the dynamic contact angle. This showed that the dynamic contact

angle significantly enhances the output of two-phase flow CFD, which is then compared with theoretical models as well as with experiments.

- The final work of this thesis focuses on apply what developed in thesis to the film flow over flat and corrugated surface. The successful of using the SVF and HF with DCA on corrugated surface is another step closer to simulated multiphasic film flow when cooling end-winding using Automatic transmission liquid. In the detail, the distinction between the SVF and HF methods greatly affects the behavior of the contact line, both in terms of its position and velocity. The HF method has demonstrated a superior ability to capture the interface with greater accuracy. However, it should be further improved for parallelization. Then, several physical phenomena have been studied. The equilibrium contact angle significantly influences the movement and interaction of the liquid with surfaces, especially within corrugated surfaces. Here, bubbles can become trapped inside the corrugations of the wall, a factor which should be considered in the future works. Reynolds number emerges as a key factor, dictating the fluid's behavior in terms of film thickness and flow progression. Higher Reynolds numbers, while promoting flow progression, can also introduce challenges, such as air bubble formations, especially in corrugated surfaces. These setup and results in this work is continue apply to reproduce the 3D corrugated surface in the future works.

8.2 Perspective

The new model developed in this study are capable of simulating film flow over flat and corrugated surfaces. However, the model needs improvement in certain areas, which will be addressed in future works:

- The Navier-slip boundary condition should be implemented in this model to achieve mesh convergence when increasing mesh resolution.
- Since the HF method currently works with a single processor, future work should focus on adapting the HF method for parallel processing, which is essential for large-scale simulations.
- The number and size of bubbles trapped within the corrugated wall were influenced by the Reynolds number and equilibrium contact angle. This can produce complicate problem for accurate heat transfer estimations. This problem should be considered in the future works.

- 3D simulation should be considered in future work. It would explore the current developments to study bubbles and heat transfer with various corrugated surfaces.

FUNDING ACKNOWLEDGMENT

We would like to extend our gratitude to IFP Energies Nouvelles for their generous financial support for this project. The contributions from IFPEN enabled us to acquire all necessary materials, access advanced computational facilities, and fund our trips for PhD training and international conferences. Their commitment to fostering research and innovation has been instrumental in the success and progression of our work.

REFERENCES

[1] Copper wires and magnetic fields - how an electric drive is made, 2021, https://modo.volkswagengroup.it/en/mobotics/copper-wires-and-magnetic-fields-how-an-electric-drive-is-made, accessed 30 September 2021.

[2] Y. Huai, R.V. Melnik, P.B. Thogersen, Computational analysis of temperature rise phenomena in electric induction motors, Applied Thermal Engineering 23 (2003) 779–795.

[3] H. Kofler, Stray Load Losses in Induction Machines A Review of Experimental Measuring Methods and a Critical Performance Evaluation, REPQJ 1 (2003) 318–323.

[4] Amal Zeaiter, Thermal Modeling and Cooling of Electric Motors Application to the Propulsion of Hybrid Aircraft, ISAE-ENSMA Ecole Nationale Supérieure de Mécanique et d'Aérotechique, Poitiers, France, 2021.

[5] K. Bennion, G. Moreno (Eds.), Convective Heat Transfer Coefficients of Automatic Transmission Fluid Jets with Implications for Electric Machine Thermal Management, 2015.

[6] M. Fénot, Y. Bertin, E. Dorignac, G. Lalizel, A review of heat transfer between concentric rotating cylinders with or without axial flow, International Journal of Thermal Sciences 50 (2011) 1138–1155.

[7] K. Bennion, Electric Motor Thermal Management, 2018 Annual Merit Review, Washington D. C., 2018.

[8] T. Davin, J. Pellé, S. Harmand, R. Yu, Experimental study of oil cooling systems for electric motors, Applied Thermal Engineering 75 (2015) 1–13.

[9] 流体解析ソフトウェア Particleworks, Particle-based simulation software for CAE "Particleworks&quot, 2023, https://www.particleworks.com/home_en.html, accessed 4 September 2023.

[10] T. Ha, D.K. Kim, Study of Injection Method for Maximizing Oil-Cooling Performance of Electric Vehicle Motor with Hairpin Winding, Energies 14 (2021) 747.

[11] S.H. Swales, P.F. Turnbull, B. Schulze, F.R. Poskie, W.J. Omell, W.C. Deneszczuk, US2011084561 (A1), 2009.

[12] M.H. Park, S.C. Kim, Thermal characteristics and effects of oil spray cooling on in-wheel motors in electric vehicles, Applied Thermal Engineering 152 (2019) 582–593.

[13] D.H. Lim, S.C. Kim, Thermal performance of oil spray cooling system for in-wheel motor in electric vehicles, Applied Thermal Engineering 63 (2014) 577–587.

[14] H. Dong, L. Ruan, Y. Wang, J. Yang, F. Liu, S. Guo, Performance of air/spray cooling system for large-capacity and high-power-density motors, Applied Thermal Engineering 192 (2021) 116925.

[15] C. Liu, Z. Xu, D. Gerada, J. Li, C. Gerada, Y.C. Chong, M. Popescu, J. Goss, D. Staton, H. Zhang, Experimental Investigation on Oil Spray Cooling With Hairpin Windings, IEEE Trans. Ind. Electron. 67 (2020) 7343–7353.

[16] Pierre de Gennes, Capillarity and Wetting Phenomena: Drops, Bubbles, Pearls, Waves.

[17] Surface tension values of some common test liquids for surface energy analysis, 2018, http://www.surface-tension.de/, accessed 11 January 2022.

[18] B. Pethica, Contact-angle equilibrium, Journal of Colloid and Interface Science Volume 62, Issue 3, December 1977, Pages 567-569.

[19] R. Tadmor, Line energy and the relation between advancing, receding, and young contact angles, Langmuir 20 (2004) 7659–7664.

[20] M.E. Schrader, Young-Dupre Revisited, Langmuir 11 (1995) 3585–3589.

[21] R.N. Wenzel, RESISTANCE OF SOLID SURFACES TO WETTING BY WATER, Ind. Eng. Chem. 28 (1936) 988–994.

[22] A.B.D. Cassie, S. Baxter, Wettability of porous surfaces, Trans. Faraday Soc. 40 (1944) 546.

[23] M. Kanungo, S. Mettu, K.-Y. Law, S. Daniel, Effect of roughness geometry on wetting and dewetting of rough PDMS surfaces, Langmuir the ACS journal of surfaces and colloids 30 (2014) 7358–7368.

[24] J.H. Yizhi Zhuo, Icephobic Materials (2018).

[25] C.W. Extrand, Contact Angles and Hysteresis on Surfaces with Chemically Heterogeneous Islands, Langmuir 19 (2003) 3793–3796.

[26] C.W. Extrand, Contact Angles and Hysteresis on Surfaces with Chemically Heterogeneous Islands, Langmuir 21 (2005) 11546.

[27] Q. Liu, J. Yu, H. Wang, The role of the substrate roughness in contact angle hysteresis and dynamic deviation, International Journal of Heat and Mass Transfer 148 (2020) 118985.

[28] J. Zhang, M.K. Borg, J.M. Reese, Multiscale simulation of dynamic wetting, International Journal of Heat and Mass Transfer 115 (2017) 886–896.

[29] S.F. Kistler, "Hydrodynamics of wetting." Wettability 6, 1993.

[30] T.D. Blake, Y.D. Shikhmurzaev, Dynamic wetting by liquids of different viscosity, Journal of Colloid and Interface Science 253 (2002) 196–202.

[31] R.G. Cox, The dynamics of the spreading of liquids on a solid surface. Part 1. Viscous flow, J. Fluid Mech. 168 (1986) 169.

[32] R.G. Cox, Inertial and viscous effects on dynamic contact angles, J. Fluid Mech. 357 (1998) 249–278.

[33] Š. Šikalo, H.-D. Wilhelm, I.V. Roisman, S. Jakirlić, C. Tropea, Dynamic contact angle of spreading droplets: Experiments and simulations, Physics of Fluids 17 (2005) 62103.

[34] E. Olsson, G. Kreiss, A conservative level set method for two phase flow, Journal of Computational Physics 210 (2005) 225–246.

[35] M. Pasandideh-Fard, S.D. Aziz, S. Chandra, J. Mostaghimi, Cooling effectiveness of a water drop impinging on a hot surface, International Journal of Heat and Fluid Flow 22 (2001) 201–210.

[36] Y.D. Shikhmurzaev, Moving contact lines and dynamic contact angles: a ‘litmus test’ for mathematical models, accomplishments and new challenges, Eur. Phys. J. Spec. Top. 229 (2020) 1945–1977.

[37] S. Afkhami, S. Zaleski, M. Bussmann, A mesh-dependent model for applying dynamic contact angles to VOF simulations, Journal of Computational Physics 228 (2009) 5370–5389.

[38] Y. Sui, P.D. Spelt, An efficient computational model for macroscale simulations of moving contact lines, Journal of Computational Physics 242 (2013) 37–52.

[39] D. Legendre, M. Maglio, Comparison between numerical models for the simulation of moving contact lines, Computers & Fluids 113 (2015) 2–13.

[40] J. Göhl, A. Mark, S. Sasic, F. Edelvik, An immersed boundary based dynamic contact angle framework for handling complex surfaces of mixed wettabilities, International Journal of Multiphase Flow 109 (2018) 164–177.

[41] M. Meier, G. Yadigaroglu, B.L. Smith, A novel technique for including surface tension in PLIC-VOF methods, European Journal of Mechanics - B/Fluids 21 (2002) 61–73.

[42] Youngs, Time-dependent multi-material flow with large fluid distortion (1982) 273.

[43] W.J. Rider, D.B. Kothe, Reconstructing Volume Tracking, Journal of Computational Physics 141 (1998) 112–152.

[44] R. Scardovelli, S. Zaleski, DIRECT NUMERICAL SIMULATION OF FREE-SURFACE AND INTERFACIAL FLOW, Annual Review of Fluid Mechanics 31 (1999) 567–603.

[45] H. Jasak, Error estimation in the finite volume method with application to fluid flows, PhD Thesis, Imperial College London, 1996.

[46] CONVERGE 3.0 Manual.

[47] Search Our Company Website: Ansys.com, 2021, https://www.ansys.com/search#q=volume%20of%20fluid&t=AllAnsysTab&sort=relevancy, accessed 9 November 2021.

[48] Basilisk - /src, 2021, http://basilisk.fr/src/, accessed 9 November 2021.

[49] Siemens Digital Industries Software, Multiphysics computational fluid dynamics (CFD) simulation software | Siemens Software, 2021, https://www.plm.automation.siemens.com/global/en/products/simcenter/STAR-CCM.html, accessed 9 November 2021.

[50] V. Boniou, T. Schmitt, A. Vié, Comparison of interface capturing methods for the simulation of two-phase flow in a unified low-Mach framework, 31 May 2021.

[51] F. Evrard, F. Denner, B. van Wachem, Estimation of curvature from volume fractions using parabolic reconstruction on two-dimensional unstructured meshes, Journal of Computational Physics 351 (2017) 271–294.

[52] D.L. Youngs, An interface tracking method for a 3D Eulerian hydrodynamics code, Technical report, AWRE (1984).

[53] E. Aulisa, S. Manservisi, R. Scardovelli, S. Zaleski, Interface reconstruction with least-squares fit and split advection in three-dimensional Cartesian geometry, Journal of Computational Physics 225 (2007) 2301–2319.

[54] G. Tryggvason, R. Scardovelli, S. Zaleski, Direct Numerical Simulations of Gas–Liquid Multiphase Flows, Cambridge University Press, 2011.

[55] J. Brackbill, D. Kothe, C. Zemach, A continuum method for modeling surface tension, Journal of Computational Physics 100 (1992) 335–354.

[56] A. Miyara, Numerical simulation of wavy liquid film flowing down on a vertical wall and an inclined wall, International Journal of Thermal Sciences 39 (2000) 1015–1027.

[57] K. Bennion, Electric Motor Thermal Management Research. Annual Progress Report, NREL, 2017.

[58] K. Bennion, Electric Motor Thermal Management R&D: Annual Report, NREL, 2016.

[59] K. Bennion, E. Cousineau, X. Feng, C. King, G. Moreno, Electric Motor Thermal Management R&D, IEEE Power & Energy Society General Meeting, Denver, CO, 2015.

[60] M. VLACHOGIANNIS, V. BONTOZOGLOU, Experiments on laminar film flow along a periodic wall, J. Fluid Mech. 457 (2002) 133–156.

[61] C.-K.C. C.-C. Wang, Forced convection in a wavy-wall channel, International Journal of Heat and Mass Transfer (2001).

[62] S.K. Mehta, S. Pati, L. Baranyi, Effect of amplitude of walls on thermal and hydrodynamic characteristics of laminar flow through an asymmetric wavy channel, Case Studies in Thermal Engineering 31 (2022) 101796.

[63] L. ZaAO and R. L. CERRO, EXPERIMENTAL CHARACTERIZATION OF VISCOUS FILM FLOWS OVER COMPLEX SURFACES, International Journal of Multiphase Flow (1992).

[64] Malamataris, N. A., et al., Computer Aided Analysis of Viscous Film Flow along an Inclined Wavy Wall, Journal of Computational Physics (1999).

[65] Yu. Ya. Trifonov, Viscous liquid flim flow over a periodic surface (1998).

[66] S. Chen, J. Ma, X. Zhang, W. Chen, Numerical simulation of the behavior of high-viscosity fluids falling film flow down the vertical wavy wall, Asia-Pac. J. Chem. Eng. 12 (2017) 97–109.

[67] N. Aksel, M. Schörner, Films over topography: from creeping flow to linear stability, theory, and experiments, a review, Acta Mech 229 (2018) 1453–1482.

[68] A. Wierschem, N. Aksel, Influence of inertia on eddies created in films creeping over strongly undulated substrates, Physics of Fluids 16 (2004) 4566–4574.

[69] M. Scholle, A. Wierschem, N. Aksel, Creeping films with vortices over strongly undulated bottoms, Acta Mechanica 168 (2004) 167–193.

[70] Q. Wang, M. Li, W. Xu, L. Yao, X. Liu, D. Su, P. Wang, Review on liquid film flow and heat transfer characteristics outside horizontal tube falling film evaporator: Cfd numerical simulation, International Journal of Heat and Mass Transfer 163 (2020) 120440.

[71] X. Zhang, J. Zhang, Y. Zhou, Z. Yue, L. Li, Colossal permittivity and defect-dipoles contribution for Ho0.02Sr0.97TiO3 ceramics, Journal of Alloys and Compounds 767 (2018) 424–431.

[72] H. Ding, P. Xie, D. Ingham, L. Ma, M. Pourkashanian, Flow behaviour of drop and jet modes of a laminar falling film on horizontal tubes, International Journal of Heat and Mass Transfer 124 (2018) 929–942.

[73] J. Chen, R. Zhang, R. Niu, Numerical simulation of horizontal tube bundle falling film flow pattern transformation, Renewable Energy 73 (2015) 62–68.

[74] F. Tahir, A. Mabrouk, M. Koç, CFD Analysis of Falling Film Hydrodynamics for a Lithium Bromide (LiBr) Solution over a Horizontal Tube, Energies 13 (2020) 307.

[75] C. Cao, L. Xie, Y. Du, X. Zhu, W. Zhang, Three-Dimensional Flow Behavior of a Falling Film on Horizontal Tubes: A Comparative Study on Smooth and Finned Tubes, Ind. Eng. Chem. Res. 61 (2022) 2346–2358.

[76] John Richard Thome, Laminar and turbulent boundary layers.

[77] F.P. Incropera, Fundamentals of heat and mass transfer, 6th ed. ed., John Wiley, Hoboken NJ, 2007.

[78] CONVERGE 3.0 Manual.

[79] D. Lörstad, M. Francois, W. Shyy, L. Fuchs, Assessment of volume of fluid and immersed boundary methods for droplet computations, Int. J. Numer. Meth. Fluids 46 (2004) 109–125.

[80] M. Sussman, A second order coupled level set and volume-of-fluid method for computing growth and collapse of vapor bubbles, Journal of Computational Physics 187 (2003) 110–136.

[81] G. Tryggvason, B. Bunner, A. Esmaeeli, D. Juric, N. Al-Rawahi, W. Tauber, J. Han, S. Nas, Y.-J. Jan, A Front-Tracking Method for the Computations of Multiphase Flow, Journal of Computational Physics 169 (2001) 708–759.

[82] S. Popinet, Numerical Models of Surface Tension, Annu. Rev. Fluid Mech. 50 (2018) 49–75.

[83] S. Popinet, An accurate adaptive solver for surface-tension-driven interfacial flows, Journal of Computational Physics 228 (2009) 5838–5866.

[84] E. Shirani, N. Ashgriz, J. Mostaghimi, Interface pressure calculation based on conservation of momentum for front capturing methods, Journal of Computational Physics 203 (2005) 154–175.

[85] M.M. Francois, S.J. Cummins, E.D. Dendy, D.B. Kothe, J.M. Sicilian, M.W. Williams, A balanced-force algorithm for continuous and sharp interfacial surface tension models within a volume tracking framework, Journal of Computational Physics 213 (2006) 141–173.

[86] J. López, C. Zanzi, P. Gómez, R. Zamora, F. Faura, J. Hernández, An improved height function technique for computing interface curvature from volume fractions, Computer Methods in Applied Mechanics and Engineering 198 (2009) 2555–2564.

[87] H.V. Patel, J. Kuipers, E. Peters, Computing interface curvature from volume fractions: A hybrid approach, Computers & Fluids 161 (2018) 74–88.

[88] P. Liovic, M. Francois, M. Rudman, R. Manasseh, Efficient simulation of surface tension-dominated flows through enhanced interface geometry interrogation, Journal of Computational Physics 229 (2010) 7520–7544.

[89] M. Owkes, O. Desjardins, A mesh-decoupled height function method for computing interface curvature, Journal of Computational Physics 281 (2015) 285–300.

[90] Victor BONIOU, On the numerical simulation of On the numerical simulation of evaporating two-phase flows using sharp interface capturing methods, 2021.

[91] I. Malgarinos, N. Nikolopoulos, M. Marengo, C. Antonini, M. Gavaises, VOF simulations of the contact angle dynamics during the drop spreading: standard models and a new wetting force model, Advances in colloid and interface science 212 (2014) 1–20.

[92] CONVERGE CFD Software, 2022, https://convergecfd.com/, accessed 12 July 2022.

[93] I.V. Roisman, L. Opfer, C. Tropea, M. Raessi, J. Mostaghimi, S. Chandra, Drop impact onto a dry surface: Role of the dynamic contact angle, Colloids and Surfaces A: Physicochemical and Engineering Aspects 322 (2008) 183–191.

[94] D. Legendre, M. Maglio, Comparison between numerical models for the simulation of moving contact lines, Computers & Fluids 113 (2015) 2–13.

[95] T. Abadie, J. Aubin, D. Legendre, On the combined effects of surface tension force calculation and interface advection on spurious currents within Volume of Fluid and Level Set frameworks, Journal of Computational Physics 297 (2015) 611–636.

[96] J. LALLEMENT, Modélisation et simulation numérique d'écoulements de films minces avec effet de mouillage partiel, 2019.

[97] M.F.G. JOHNSON, R.A. SCHLUTER, M.J. MIKSIS, S.G. BANKOFF, Experimental study of rivulet formation on an inclined plate by fluorescent imaging, J. Fluid Mech. 394 (1999) 339–354.